Quantum electrodynamics with 1D artificial atoms: from Purcell enhancement to single-photon nonlinearities

A dissertation
submitted to the Niels Bohr Inistitute
at the University of Copenhagen
in partial fulfillment of the requirements
for the degree of
philosophiae doctor

Alisa Javadi
February 2, 2015

Quantum electrodynamics with 1D artificial atoms: from Purcell enhancement to single-photon nonlinearities

Preface

The research in this thesis was done between Febraury 2012 and January 2015 at Niels Bohr Inistitute, University of Copenhagen. During the period I was enrolled as a PhD student in Quanntum Photonics group (QP) under Prof. Peter Lodahl's Suppervision. I enjoyed nice sientific enviroment in Quantum Photonics group and I would like to thank all memebers of QP for their help during my thesis. In particular I would like to thank following people for their help in various aspects of this thesis:

First of all, I would like to thank Peter for his attitude and support during my PhD. Peter has a deep passion for physics and I always enjoyed insightful discussions with him not only during the meetings but also over lunch breaks. I would also like to express my sincere regards to David García who introduced me to the optics lab and supervised me during several parts of my PhD. I was inspired by his hard working and patient character.

Next, I would like to thank Sahand Mahmoodian for his relaxed attitude and warm manner. His knowledge of numerical modeling and photonic nanostructures was a big support during the course of my PhD, particularly during the work done in chapter 3. Additionally, I benefited from discussion we had about the work in chapter 5. I would also like to thank his unlimited patience in proof reading articles and manuscripts during my thesis. Immo Söllner did a lot of the background work for the research done in chapter 4 and 5, and I benefited discussions with him during the measurements in chapter 5, as well as most of my PhD. My warm regards goes to him. Additionally, I would like to thank Marta Arcari and Sofie Lindskov Hansen for their help during the experiments in chapter 4 and 5.

Several students and postdocs have dedicated their time to fabricating the nanostructures used in the experiments in this thesis. I would like to thank Søren Stobbe for supervising the fabrication team and also for inspiring discussions. Gambia Kiršanskė, Haitham El-Ella, Leonardo Midolo, and Tommaso Pregnolato have been the core members of the fabrication team, and the experiments in chapters 4 and 5 would not be possible without the nice samples.

I shared the office with Sahand and Marta during my PhD, and we had a very friendly and nice environment. A lot was added to my scientific understanding during the enlightening discussions with my officemates and my cheers goes to them. The QP has a tradition of getting together for lunch . The nice discussions over these lunch meetings have made the life in NBI more joyful.

I definitely loved the friendly and social environment in QP, especially the traditional Friday evening get togethers. I would like to thank all who joined and shared the fun. My thanks go to Petru Tighineanu whom we shared a lot of fun during the last three years, both in NBI and in the life outside. I made good friends with Immo and Sahand as well as all other group members.

QP has always been a nice environment to work in. My would like to thank the other past and present members of QP: Qin Wang, Jin Liu, Kristian Høeg Madsen, Tau Lehmann and Raphael Daveau for contributing and maintaining this nice environment. Our group is a part of the bigger quantum optics subdivision in NBI. I would like to thank the rest of members of the quantum optics community for a nice academic environment and the many enlightening discussions over the coffee breaks.

Finally, I would like to thank my family and friends who supported me during my PhD and this thesis. Especial thanks and regards go to my parents Lida and Rahim, and my sister Shalale.

Abstract

A 1D atom, a single quantum emitter coupled to a single optical mode, exhibits rich quantum electrodynamic (QED) effects and is thought to be the key ingredient for many applications in quantum-information processing. Single quantum dots (QD) in photonic-crystal waveguides (PCW) constitute a robust platform for realizing a 1D atom, and are the subject of theoretical and experimental investigations in this thesis. We use finite element method in 3D to calculate the local density of states (LDOS) in photonic-crystal membranes. The detailed spatial maps show strong inhibition of LDOS in the bandgap of the PhC, as large as 160 times. The method is extended to PCWs using a set of active boundary conditions. The extended method allows separating the contribution to the LDOS from the propagating mode and the radiation continuum. The detailed spatial maps of the LDOS show that for a broad spectral range, the contribution from the radiation continuum is much less than the contribution from the guided mode. The coupling efficiency between an embedded emitter and the PCW is shown to be higher than 90% for a wide range of dipole positions, frequencies and orientaitions, which qualifies the system as a candidate for a 1D atom. One of the signatures and functions of a 1D atom is the nonlinear optical response at the single-photon level. A PCW chip is designed to experimentally study the transmission spectrum of an embedded QD. The transmission spectrum is shown to be modified by 30% around the resonance of the QD. The power dependence of the transmission shows a nonlinearity with a critical power of 1.9 nW, which corresponds to an average number of 0.8 photons per lifetime of the emitter at the position of the QD. The autocorrelation function of the transmitted field shows bunching of the transmitted photons as expected from the theory. The value of $g^{(2)}(0)$ is around 1.08. The results confirm the observation of an on-chip giant optical nonlinearity and the 1D atom behavior. Another direction in this thesis has been to investigate the effect of Anderson localization on the electrodynamics of QDs in PCWs. A large data set of the statistics of Purcell-enhancement of QDs in Anderson-localized cavities is presented. The average Purcell-enhancement of 4.5 times, with a peak value of 12 is observed for QDs randomly positioned in Anderson-localized modes of a PCW.

Resumé

Et 1D atom, en enkelt kvante emitter koblet til en enkelt optisk tilstand, udviser mange kvante elektrodynamiske (QED) effekter og betragtes som den væsentligste del af mange anvendelser indenfor kvanteinformations behandling. Enkelte kvante-punkter (quantum dots, QD) i fotonisk-krystal bølgeledere (photonic-crystal waveguides, PCW) udgører en robust platform for realiseringen af et 1D atom, og er emnet for en teoretisk og eksperimentel undersøgelse i denne afhandling. Vi bruger endelig elementers metode i 3D til at beregne den lokale tilstandstæthed (local density of states, LDOS) i fotonisk-krystal membraner. Det detaljerede rumlige kort viser kraftig undertrykkelse af LDOS i båndgabet af den fotoniske krystal, så meget som 160 gange. Denne metode udvides til PCWer ved at benytte et sæt af aktive grænsebetingelser. Denne udvidede metode tillader separering af bidragene til LDOS fra den propagerende tilstand og strålings kontinuumet. Det detaljerede rumlige kort over LDOS viser, at for et bredt spektralt område er bidragende fra strålings kontinuumet meget mindre end bidraget fra den guidede tilstand. Koblingseffektiviteten mellem en indlejret emitter og PCWen vises at være højere end 90% for et bredt område af dipol-positioner, -frekvenser og -orienteringer, hvilket gør systemet til en kandidat for et 1D atom. En af signaturene og funktionerne af et 1D atom er den ikke-lineære optiske respons på enkelt-foton niveauet. En PCW-chip er designet til eksperimentelt at undersøge transmissionsspektret af en indlejret QD. Transmissionsspektret vises at være ændret med 30% omkring QDens resonans. Effekt-afhængigheden af transmissionen viser en ikke-linearitet ved en kritisk effekt på 1.9nW, hvilket svarer til et gennemsnitligt antal på 0.8 fotoner per livstid af emitteren ved QDens position. Autokorrelationsfunktionen af det transmitterede felt viser en samling ("bunching") af de transmitterede fotoner, som forventet fra teorien. Værdien af $g^{(2)}(0)$ er omkring 1.08. Resultaterne bekræfter observationen af en stor on-chip optisk ikke-linearitet og den 1D-atomare opførsel. En anden retning i denne afhandling har været at undersøge effekten af Anderson-lokalisering på elektrodynamikken af QDerne i PCWer. Et stort datasæt med statistikken fra Purcell-forstærkning af QDer i Anderson-lokaliserede kaviteter præsenteres. Den gennemsnitlige Purcell-forstærkning på 4.5, med en peak-værdi på 12, er observeret for QDer vilkårligt positioneret i Anderson-lokaliserede tilstande af en PCW.

List of Publications

The work performed in the work of this Ph.D.-project has resulted in the publications listed below:

Journal Publications

1. **A. Javadi**, S. Maibom, L. Sapienza, H. Thyrrestrup, Pedro D. García, and Peter Lodahl, *Statistical measurements of quantum emitters coupled to Anderson-localized modes in disordered photonic-crystal waveguides*, Optics Express, **22**, 30992 (2014).

2. M. Arcari, I. Söllner, **A. Javadi**, S. L. Hansen, S. Mahmoodian, J. Liu, H. Thyrrestrup, E. H. Lee, J. D. Song, S. Stobbe, and P. Lodahl, *Near-unity coupling efficiency of a quantum emitter to a photonic-crystal waveguide*, Physical Review Letters **113**, 093603 (2014).

3. P. D. García, **A. Javadi**, H. Thyrrestrup, and P. Lodahl, *Quantifying the intrinsic amount of fabrication disorder in photonic-crystal waveguides from optical far-field intensity measurements*, Applied Physics Letters **102**, 031101 (2013).

4. K. H. Madsen, S. Ates, J. Liu, **A. Javadi**, S. M. Albrecht, I. Yeo, S. Stobbe, P. Lodahl, *Efficient out-coupling of high-purity single photons from a coherent quantum dot in a photonic-crystal cavity*, Physical Review B **90**, 155303 (2014).

5. I. Söllner, S. Mahmoodian, S. L. Hansen, L. Midolo, **A. Javadi**, G. Kiršanskė, T. Pregnolato, H. El-Ella, E. H. Lee, J. D. Song, S. Stobbe, and P. Lodahl, *Deterministic photon-emitter coupling in chiral photonic circuits*, *arXiv:1406.4295*.

Journal Publications in Preparation

1. **A. Javadi**, I. Söllner, M. Arcari, S. Lindskov Hansen, L. Midolo, S. Mahmoodian, G. Kiršanskė, T. Pregnolato, E. H. Lee, J. D. Song, S. Stobbe, and P. Lodahl, *Single photon nonlinear optics with a quantum dot in a waveguide*, In preparation.

2. **A. Javadi**, S. Mahmoodian, I. Söllner,and P. Lodahl, *In-depth investigation of quantum emitters in photonic crystal waveguides using finite-element modeling*, In preparation.

3. M. Nishan, **A. Javadi**, and P.D. Garcia, and P. Lodahl, and S. Hughes, *Theory and experiments of disorder-induced resonance shifts and mode edge broadening in deliberately disordered photonic crystal waveguides*, In preparation.

Conference Contributions as presenting author

1. **A. Javadi**, P. D. García, L. Sapienza, S. Maibom, H. Thyrrestrup, and P. Lodahl, *Statistics of decay dynamics of quantum emitters in disordered photonic-crystal waveguides*, CLEO/QELS, San Jose, California, USA, 2014.

2. **A. Javadi** and P. Lodahl, *Numerical Study of Local Density of States in Photonic Crystal Waveguides*, Comsol Conference, Oct. 2013, Rotterdam, Netherlands.

Contents

Preface ii

Abstract v

Resumé vi

List of publications viii

1 Introduction 1

1.1 Quantum dots as artificial atoms 1

1.2 A short introduction to photonic crystals 4

1.3 1D atom 6

1.4 Outline of the thesis 7

2 Classical and quantum electrodynamical effects in disordered photonic-crystal waveguides 9

2.1 Introduction and literature review 9

2.2 Quantum electrodynamical effects of Anderson-localized modes 14

2.2.1 Experimental methods 14

2.2.2 Far-field mapping of the Anderson-localized modes along the photonic-crystal waveguide 15

2.2.3 Time-resolved measurements on Anderson-localized cavities 16

2.2.4 Time-resolved measurements on single quantum dots 18

2.3 Effect of disorder on the spectral position of band-edge 19

2.3.1 Numerical modeling of disorder induce band-edge shift 21

2.3.2 Comparison to experimental results 22

2.4 Conclusions 23

3 Numerical modeling of quantum emitters in a modified local density of states 25

3.1 Introduction and literature review . . . 25

3.2 Spontaneous emission rate of a quantum emitter . . . 27

3.3 Preface to finite element modeling . . . 28

3.4 Decay rate of a dipole in a photonic crystal . . . 30

3.4.1 Details of implementation . . . 31

3.4.2 Results . . . 32

3.4.3 Connection to the experimental results . . . 34

3.5 Electrodynamics of a dipole in a photonic-crystal waveguide . . . 35

3.5.1 Simulation method . . . 37

3.5.2 Results . . . 39

3.5.3 Convergence test results . . . 43

3.5.4 Comparison to experiments . . . 44

3.6 Out-coupling of light from planar nanostructures . . . 46

3.7 Conclusions . . . 49

4 Resonant excitation of quantum dots in photonic-crystal waveguides 51

4.1 Introduction and literature review . . . 52

4.2 Experimental considerations . . . 54

4.2.1 Sample structure . . . 55

4.2.2 Experimental setup . . . 56

4.3 Preliminary experiments on the first generation of samples . . . 59

4.4 Measurements on the second generation of the samples . . . 63

4.4.1 Early stages of the measurement . . . 63

4.4.2 Later stage of the measurements . . . 66

4.4.3 The final measurements . . . 70

4.4.4 Effect of the repump wavelength and intensity on the transmission dip . . . 71

4.4.5 Measurement of the ground state lifetime and revival time constant . . . 73

4.4.6 Others efforts to increase the transmission dip contrast . . . 75

4.5 Conclusions and outlook . . . 77

5 Single-photon nonlinearity induced by a single quantum dot in a photonic-crystal waveguide: theory and experiment **79**

5.1 Introduction and literature review 80

5.2 Theoretical background 82

5.2.1 Full equations for the transmission coefficient 83

5.2.2 Autocorrelation function of the transmission 87

5.2.3 Effect of spectral diffusion and blinking of the emitter 89

5.3 Experimental demonstration 90

5.3.1 Nonlinear transmission of the photonic-crystal waveguide 92

5.3.2 The photon statistics of the transmitted field 93

5.4 Conclusions and outlook 95

A Convergence analysis of the height of the active boundary conditions **97**

B Mesh convergence tests **101**

C Procedure for modeling the experimental data in chapter 5 **105**

Chapter 1

Introduction

Indium-Arsenide (InAs) quantum dots (QDs) embedded in Gallium-Arsenide (GaAs) have interesting properties for quantum optics. The internal structure of a single InAs QD offers sharp optical transitions with large dipole moments and relatively decoherence-free spin states. Additionally, nanostructures may be formed in the host GaAs to efficiently interface the QD to an optical field. Ultimately, a QD can be made to interact with just a single optical mode, which constitutes an artificial 1D atom. A 1D atom is a key ingredient in realizing many building blocks for quantum information processing, e.g. optical nonlinearities at the single photon level, single-photon transistors and photon sorters.

Photonic crystals (PhC) are the most successful nanostructures for controlling light behavior and their potential for quantum electrodynamics has been highlighted in several earlier works. In this thesis, we study photonic-crystal waveguides (PCWs) in detail and utilize them for different quantum optics experiments with InAs QDs. This chapter gives a short introduction to the InAs QDs, their structural and optical properties, as well as an overview of the photonic-crystal nanostructures, with particular emphasis on PCWs. The last section of this chapter includes the outline of the thesis.

1.1 Quantum dots as artificial atoms

In this section, we review the definition and properties of a quantum dot (QD). A QD is an island of a semiconductor with a smaller bandgap inside another semiconductor with a larger bandgap [1, 2], see figure 1.1(a). A QD is typically several nanometers high in the growth direction and tens of nanometers long in the directions normal to the growth axis. These dimensions are smaller than the exciton Bohr radius of the island material, hence the island acts as a three dimensional confinement potential for charge carriers. Consequently, the energy levels inside the QD are discretized, in close analogy to the discreet energy levels of an atom. This has given the QDs the name "artificial atom". Figure 1.1(b) shows the energy-level structure of a InAs/GaAs QD. The host material, GaAs, has a bigger bandgap than the island material (InAs). Therefore, several localized energy levels form in the

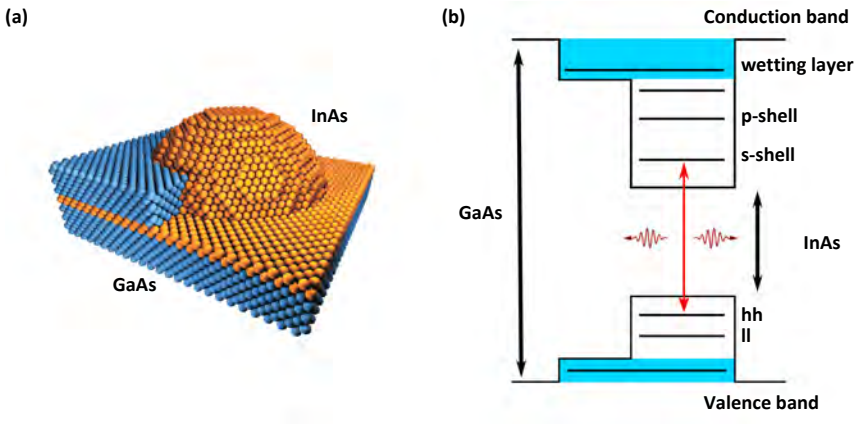

Figure 1.1: (a) Schematic image of a InAs/GaAs QD, courtesy of M. L. Andersen. (b) Energy structure of a InAs/GaAs QD, showing the electron state s-shell and p-shell and the heavy hole state. The s-shell is characterized by total angular momentum $\pm 1/2$ and the highest energy hole band (hh) is characterized by total angular momentum $|\pm 3/2\rangle$. The wetting layer is marked as the blue regions.

conduction band and valence band of the island material. The energy levels inside the conduction band are named s-shell, p-shell, and so on. The energy levels inside the valence band are named, heavy-hole band (hh), and light-hole band (lh) in the simplest picture. For a symmetric QD, the energy levels are identified by their total angular momentum and projected orbital angular momentum in the growth direction, $|J, j_z\rangle$. For the rest of this section, we focus on the s-shell states and the hh level states, since the optical transitions between these two levels have the largest oscillator strength [1, 3]. The s-shell is doubly degenerate and has two orbitals $|1/2, 1/2\rangle$ and $|1/2, -1/2\rangle$. We represent an electron in the $|1/2, 1/2\rangle$ orbital as $|\uparrow\rangle$, and an electron in the $|1/2, -1/2\rangle$ as $|\downarrow\rangle$, corresponding to spin state of the electron. The hh band, on the other hand, has two levels that are characterized as $|3/2, \pm 3/2\rangle$. The holes in these orbitals are denoted as $|\Uparrow\rangle$ and $|\Downarrow\rangle$ respectively.

Different charge configurations are possible inside a QD. The ground state of the QD ($|g\rangle$) can be neutral or charged. The first excited states of a neutral QD are the neutral excitons ($|X^0\rangle$). A neutral exciton is a combination of an electron and a hole. The four possible $|X^0\rangle$ states are $|\uparrow\Downarrow\rangle$, $|\downarrow\Uparrow\rangle$, $|\uparrow\Uparrow\rangle$, and $|\downarrow\Downarrow\rangle$. j_z for the first two excitons is ± 1 and hence the two excitons can recombine optically and emit a circularly polarized photon. The last two are dark excitons ($j_z = \pm 2$) and are optically inactive. However, an actual QD lacks the rotational symmetry and hence the excitons hybridize [1, 3–5]. Due to the symmetries of the underlying crystal orbitals, the two bright excitons hybridize together while the dark ones hybridize with each other. The resulting excitons are $\frac{1}{\sqrt{2}}(|\uparrow\Downarrow\rangle \pm |\downarrow\Uparrow\rangle)$ and $\frac{1}{\sqrt{2}}(|\uparrow\Uparrow\rangle \pm |\downarrow\Downarrow\rangle)$. The projected orbital angular momentum for the new excitons are $j_z = 0$ and $j_z = \pm 2$ respectively. Therefore, the bright excitons emit linear photons and the dark excitons remain dark. Other mechanisms can mix the dark and the bright states together, e.g. magnetic fields. Phonons can also mediate interaction between the dark excitons and the bright excitons through spin flip processes [6, 7]. Figure 1.2 shows the level diagram of a neutral exciton. The two bright excitons ($\frac{1}{\sqrt{2}}(|\uparrow\Downarrow\rangle \pm |\downarrow\Uparrow\rangle)$) decay radiatively to the ground state. There is also a nonradiative decay channel for the bright excitons (not shown in the figure). However, this nonradiative decay is around an order of magnitude slower than the radiative decay for InAs QDs.

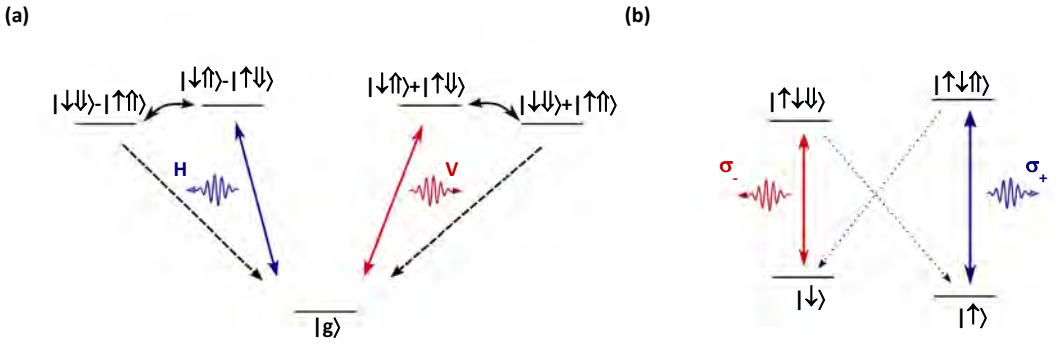

Figure 1.2: (a) Level structure of a neutral exciton. The two bright states ($\frac{1}{\sqrt{2}}(|\uparrow\Downarrow\rangle \pm |\downarrow\Uparrow\rangle)$) emit linearly (V/H) polarized photons. The normalization constant $\frac{1}{\sqrt{2}}$ has been dropped in the figure. Spin flip processes couple the two dark states to the two bright states. The dark states can also decay to the ground level through nonradiative processes. (b) The level diagram of a negatively charged QD. The two X^- states emit right and left circular photons. As long as the magnetic field in plane of the QD is zero, the diagonal transitions are forbidden due to spin selection rules.

A QD can also be charged, that is an electron or a hole can be in the QD for a long time. The four possible ground states for the charged QD are: $|\uparrow\rangle$, $|\downarrow\rangle$,$|\Uparrow\rangle$, and $|\Downarrow\rangle$ [5,8]. When an electron-hole pair is added to the extra charge in the QD, a charged exciton forms (X^+ or X^-). The four possibilities for a charged exciton are: $|\uparrow\downarrow\Downarrow\rangle$, $|\uparrow\downarrow\Uparrow\rangle$, $|\uparrow\Uparrow\Downarrow\rangle$, $|\downarrow\Uparrow\Downarrow\rangle$, where the first two are associated with an extra electron trapped int the QD and the later two are associated with an extra hole . For all these configurations $j_z = \pm 1$ and hence all of them are optically active and emit circularly polarized photons. Figure 1.1(b) shows the level structure of a QD, with an electron trapped in it (X^-). As long as the in-plane magnetic field is zero, the diagonal transitions (shown as doted black arrows) are very weak and in the ideal case spin forbidden [8,9].

A QD, regardless of its charge state, can be excited in several ways. The most common method is to excite the QD by creating charge carriers in the host material, which subsequently fall to the wetting layer and then to the QD (above-bandgap excitation). For a InAs/GaAs the above band gap excitation requires a pump wavelength of lower than 800 nm. Alternatively, one can directly excite the carriers inside the wetting layer (wetting layer excitation). The typical wavelengths for wetting layer excitation are around 850 nm. The third method would be to excite the carriers directly to a higher excited state of the QD (p-shell excitation). The mentioned methods pump carriers incoherently to the s-shell of the QD, and are used in limited cases, mostly for spectral analysis. Alternatively, one can directly excite the exciton by a laser that has the same energy as the exciton transition (resonant excitation). The resonant excitation allows to coherently interface the state of a photon directly to the internal state of the QD and is required in the quantum information applications [5]. In the next section, we discuss PhCs and their potential for controlling light in nanometer scales.

1.2 A short introduction to photonic crystals

Photonic crystals are the optical analog of semiconductor crystals [10, 11]. A PhC is a periodic modulation of the refractive index of a homogenous medium on the scale of the wavelength. The light propagation in a PhC is governed by Bloch modes which have the periodicity of the crystal. Similar to semiconductors, PhCs also have energy gaps in their dispersion diagram where light propagation is inhibited [12]. A 3D modulation of the refractive index allows to produce full bandgaps for light propagation; however, from the fabrication point of view it is more appealing to work with lower dimensional materials. PhC membranes are a class of PhCs where the light propagation in two planar

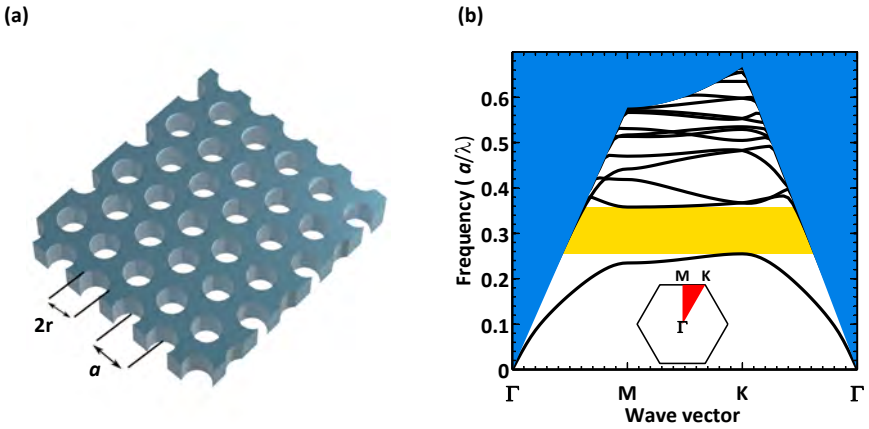

Figure 1.3: (a) A pictorial sketch of a PhC membrane. (b) Bandstructure of the PhC for propagation in different crystallographic directions (Only the TE modes are plotted). The hexagonal in the middle shows the Brillouin zone. The blue region is the light cone, where the modes are not bound to the membrane. The yellow area indicates the bandgap for the TE modes.

dimensions is controlled by the modulation of the refractive index of the material, and in the third direction the light is confined to the membrane by total internal reflection. Figure 1.3 shows triangular lattice of air holes in a membrane. The modes of the membrane can be classified as transverse magnetic modes (TM) and transverse electric (TE) modes, according to their symmetry with respect to the center of the membrane. The particular geometry of the crystal has a bandgap only for the TE modes. The lattice constant of the PhC is a and the hole radius is r. Figure 1.3(b) shows the energy of TE modes for different propagation directions. The solid black lines are the eigenmodes of the membrane. The blue area in this plot is the light cone, where the modes are not bounded to the membrane. The interesting section of this bandstructure is the area colored yellow, where no modes are supported inside the PhC. Depletion of optical modes has several consequences. For instance, the spontaneous emission from an emitter is inhibited at these frequencies which is an important feature for quantum electrodynamics of the emitter. This is the topic of chapter 3. Furthermore, a geometrical defect (for instance a displaced or removed hole) creates tightly localized modes in the bandgap of the PhC. This fact is the operational concept of most of the PhC based devices [12], such as PhC cavities and waveguides. PhC cavities and waveguide have attracted a tremendous interest in the recent decades and have been successfully used for a wide range of applications [12].

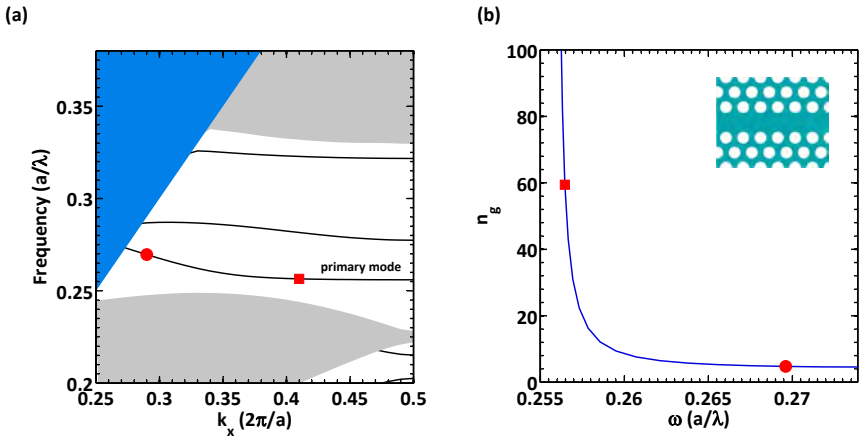

Figure 1.4: The structure of a PCW can be seen as an inset on the right side of the figure. (a) Bandstructure of the PCW. The three guided TE modes are shown as solid black lines. The red rectangle and the red circle mark $N_g = 5$ and $N_g = 58$ respectively. The light propagation is slowed down in the PCW and ultimately reaches zero when the frequency approaches the band-edge of the primary mode. The gray regions are membrane guided modes. These modes are bounded to the membrane but not to the waveguide. The blue area is the light cone. (b) The group index (N_g) as a function of the frequency.

One of the interesting nanostructures based on PhCs is the PCW. A photonic-crystal waveguide (PCW) is created by removing a row of holes from a perfect PhC, see the inset in the right side of figure 1.4. Figure 1.4(a) shows the bandstructure of a PCW. The solid black lines are the guided modes of the waveguide. At the frequency of these modes, the light is tightly bound to the defect-line and only propagates along the defect-line; other optical modes are still inhibited as for the PhC. Three different waveguide modes are visible in figure 1.4. The interesting feature of the guided modes is the low group velocity of these modes close to the bandedge($k_x = \pi/a$). At these frequencies, the light propagation slows down and ultimately at the band-edge the propagation speed reaches zero. Figure 1.4(b) shows the group refractive index, N_g, for the lowest-energy mode of the waveguide. The slow-down of the light is important for several applications, for instance small-footprint delay lines. Another consequence of slow propagation velocity is the stronger interaction of the light and matter inside the PCW.

The interaction between the primary mode and an embedded quantum emitter is very efficient for two reasons. First of all, the decay rate of a quantum emitter inside a PCW is proportional to N_g of the waveguide, and hence the decay rate of the emitter is highly enhanced close to the PCW edge. Secondly, all other optical modes are inhibited, which means that the coupling to these modes is decreased significantly. These two properties make a PCW an ideal candidate for a 1D atom. In the next section, we discuss the concept of 1D atom and its applications.

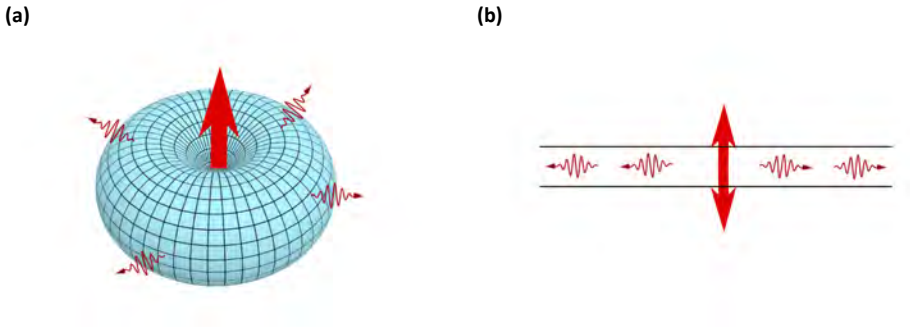

Figure 1.5: (a) The far-field pattern of an atom. The dipole moment of the atom is oriented along the red arrow. Photons are emitted on a toroid-like shape in free space. (b) An atom efficiently coupled to a waveguide mode. All the photons emitted from the atom couple to the waveguide. Hence, the waveguide acts as a deterministic interface to the atom.

1.3 1D atom

Two-level systems are considered as the building blocks of the quantum computers [13]. In the quantum optical approach to a quantum computer, atoms or artificial atoms are the candidate for the two-level system [14,15]. However, a deterministic interface between the atom and flying photons is a must for scalable quantum information processing [15,16]. Unfortunately, the emission pattern of an atom is distributed over a 4π solid angel and a deterministic interface to a bare atom is impossible. Figure 1.5(a) shows the far-field emission pattern of a dipole emitter, for instance. On the other hand, it is possible to couple the individual atoms to single localized or propagating modes. In such a case, the coupling efficiency of the atom to the target mode can be measured as the ratio of the decay-rate of the atom to the target mode over the total decay rate of the atom $\beta = \frac{\Gamma_{\text{target}}}{\Gamma_{\text{target}}+\gamma}$, where γ is the decay to all other modes. Ultimately in the case that $\gamma << \Gamma_{\text{target}}$, β approaches one, which means all the photons emitted from the atom are collected to a single mode. Such a system is called a 1D atom [17], since all the photons that are launched to the mode will interact with the atom and all the photons that are scattered from the atom will couple to the single mode. Figure 1.5(b) shows a schematic demonstration of a 1D atom.

A number of different platforms have been proposed to realize a 1D atom. Experimentally, microwave qubits coupled to superconducting waveguides [18], single atoms coupled to micro-cavities [19, 20] and waveguides [21], single QDs coupled to PCWs and dielectric nanowires [22–24], and nitrogen vacancy centers coupled to plasmonic nanowires [25] have been shown to exhibit properties similar to a 1D atom.

Theoretically 1D atom opens numerous opportunities for scalable quantum computing [15]. A true 1D atom will enable deterministic CNOT gates [15], photon sorters [26], Bell-state analyzers [26], and single-photon transistors. Along with these, a 1D atom enables obtaining optical nonlinearities on single photon levels, where the response of the system for one incident photon and two incident photons is different. Such a giant nonlinearity can have applications for quantum and classical information

processing. Single-photon nonlinearity from an artificial atom (QD) coupled to a PCW is the topic of the last chapter of the thesis.

1.4 Outline of the thesis

This thesis is organized as follows. Chapter 2 deals with the effect of disorder in PCWs and Anderson localization. We experimentally probe the statistics of the lifetime enhancement from QDs coupled to Anderson-localized cavities. Also, we observe and model the effect of disorder on the band-edge of the PCWs.

Chapter 3 includes an extensive modeling of quantum electrodynamics of a dipole emitter in a PCW. We present a method to extract the exact local density of states in a PCW, and to separate the contribution from the guided mode and the radiation modes of the waveguide. Finally we discuss the relevance of the modelings to very recent experiments. The results in this chapter reemphasize the potential of QDs embedded in PCWs as a platform to realize a 1D emitter.

In chapter 4, the experimental details of resonantly exciting QDs in PCWs are presented. The ground state of the QDs is a metastable state, and a weak aboveband laser helps stabilize this ground state. We examine the effect of the aboveband laser intensity and wavelength on the optical properties of a QD. The results in this chapter lay the grounds for the work in chapter 5. In chapter 5, we experimentally demonstrate optical nonlinearity in the transmission of a 1D artificial atom, composed of a QD embedded in a PCW. The power dependence of the transmission of the artificial atom shows a nonlinear behavior, where the critical photon number is below one photon. The single photon nature of the nonlinearity is further confirmed by the modified photon statistics of the transmitted field. The demonstrated nonlinear transmission of the 1D artificial atom has a broad range of applications from photon sorters and switches to single-photon transistors.

Chapter 2

Classical and quantum electrodynamical effects in disordered photonic-crystal waveguides

This chapter partly builds on reference [27]. In this chapter, we present a statistical study of the Purcell enhancement of the light emission from quantum dots coupled to Anderson-localized cavities formed in disordered photonic-crystal waveguides. We measure the time-resolved light emission from both single quantum emitters coupled to Anderson-localized cavities and directly from the cavities that are fed by multiple quantum dots. Strongly inhibited and enhanced decay rates are observed relative to the rate of spontaneous emission in a homogeneous medium. From a statistical analysis, we report an average Purcell factor of 4.5 ± 0.4 without applying any spectral tuning. Also, we study and model the effect of disorder on the band-edge of the photonic-crystal waveguides. The experimental data show a blueshift and broadening of the band-edge of the photonic-crystal waveguide with increasing amount of disorder in the sample, in qualitative agreement with the numerical models.

2.1 Introduction and literature review

Photonic crystals are arguably one of the best approaches to engineer light propagation and interaction [12, 28]. During the past decades, significant effort has been spent on designing and utilizing photonic crystal based devices for various applications both in classical and quantum optics [29, 30]. In the classical domain, cavities with Q-factors reaching 2 million [31], nonlinear optical interactions, frequency conversion [32], and very low-power optical switching have been demonstrated [33]. In the quantum regime, controlled spontaneous emission [34, 35] with modifications of the emission rate approaching two orders of magnitude [36] and strong coupling between a single quantum dot and a photon in a photonic-crystal cavity [37] have been achieved.

CHAPTER 2. CLASSICAL AND QUANTUM ELECTRODYNAMICAL EFFECTS IN DISORDERED PHOTONIC-CRYSTAL WAVEGUIDES

As discussed in chapter 1, PhCs are dielectric structures where a periodic variation of the refractive index leads to the formation of a frequency range, the photonic band gap, where the electromagnetic wave propagation is strongly suppressed [12]. One possible implementation of a two dimensional PhC can be obtained by etching a hexagonal lattice of holes in a membrane of a high refractive index material. In such a PhC, a photonic-crystal waveguide (PCW) is formed by leaving out a row of holes, see figure 2.1(a). In that case, light is tightly confined and effectively guided along the missing row of holes due to the presence of an in-plane band gap in the PhC and by total internal reflection within the membrane. Three different (longitudinal) waveguide modes are found in the band gap, cf. the dispersion diagram of figure 2.1(b) and the mode profiles in Figs. 2.1(c) and 2.1(d).

At the edges of a PhC band gap and close to the cut-off of the waveguide modes, the LDOS is strongly enhanced and even diverges in the case of a perfect crystal. This effect is called the Van-Hove singularity and implies an ideally vanishing waveguide mode group velocity thus forming a standing wave. In real structures, fabrication imperfections smooth this singularity, but a strongly enhanced LDOS still prevails near the cutoff of the waveguide mode [38]. This ability to enhance the LDOS makes PhCs and PCWs very useful for slowing down light [39], optomechanical experiments [40] and deterministic photon-emitter interfaces [22, 23] for quantum-information applications.

The presence of disorder in a PhC, ultimately due to the limited precision of the fabrication process, breaks the discrete translational symmetry of the structure, see figure 2.1(a). Disorder degrades the performance of the PhC-based structures in several ways. Disorder induces propagation loss in the PCWs [41–45], and decreases the quality factor of the PhC cavities. Disorder can also shift the spectral position of the PhC cavities and waveguides [46, 47]. It also forms localization by inducing random multiple scattering of light and creates one-dimensional Anderson-localized modes [11, 48].

The Anderson-localized modes approximately inherit the polarization properties of the propagating modes in the waveguide, as seen in figure 1(c) and 1(d). Due to their random nature, a statistical analysis is required to extract the spectral and spatial properties of these modes. They appear around and below the cut-off frequency of the waveguide mode or at the band-edge forming a so-called Lifshitz tail [49, 50], as marked in figure 2.1(b) by the shadowed regions for the waveguide modes. After ensemble averaging over all configurations of disorder, the electric field from an embedded emitter will decay exponentially in space with a characteristic length called the localization length (ξ) [51]. A finite-element calculation of the E_y components of two different Anderson-localized modes is shown in figures. 2.1(c) and 2.1(d) that is compared to the Bloch modes of the ideal periodic structure. Remarkably, such random cavities in a PCW have been found to have quality (Q) factors and mode volumes that are comparable to state-of-the-art engineered cavities [52–54], both in silicon-based structures [52] and in optically active materials such as GaAs [55], with the benefit of having less stringent requirements on sample fabrication precision. Disorder-induced cavities have attracted significant attention and have been proposed for light harvesting [56], used in cavity quantum electrodynamic (QED) experiments [55], and for random lasing [57, 58].

Several groups have studied the effect of disorder and the formation of Anderson localization in photonic-crystal waveguides [44, 46, 47, 50, 52, 55, 58–67]. Topolancik *et al.* studied light transmission

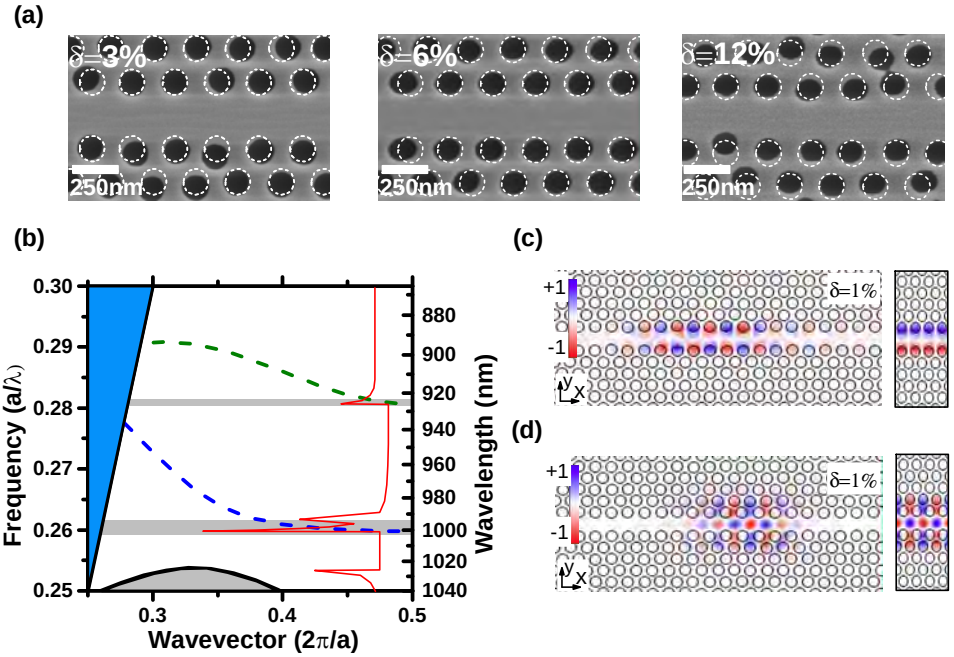

Figure 2.1: (a) Scanning-electron micrographs of photonic-crystal waveguides with different amounts of intentional disorder in the hole position. Dashed circles indicate the positions of the holes in a perfectly periodic structure. (b) Dispersion relation for an ideal photonic-crystal waveguide showing the fundamental (dashed blue line) and high-energy (green) guided modes from a full 3D simulation of a photonic-crystal membrane structure. The blue area corresponds to the light cone where the radiation is not bound to membrane. The band gap of the photonic crystal extends from $a/\lambda = 0.255$ to the top of the figure. The shadowed area near the cutoff of the guided modes indicate the spectral range where Anderson-localized modes appear. The red curve is a sketch of the local density of optical states of a disordered structure. (c) and (d) Illustration of Anderson-localized modes obtained from 2D finite-element calculation of the E_y component of the electric field in a disordered perturbed PCW with $\sigma = 1\%$ introduced disorder in the hole positions (left) and along an unperturbed PCW (right) corresponding to the high-energy ($\lambda = 850$ nm) (c) and fundamental ($\lambda = 930$ nm) (d) guided modes shown in (b).

in photonic-crystal waveguides and observed strong localization around the primary guided mode of the PCW due to Anderson localization [52]. They later reported on Q-factors in the range of 6×10^5 in the telecommunication wavelengths, due to Anderson localization. Baron *et al.* studied light transport in photonic-crystal waveguides and coupled cavity waveguides theoretically. They predicted that exponential decay of the light transmission in presence of disorder holds for photonic-crystal waveguides, although the strong dispersion. They also predicted that the exponential decay law would not hold for grating nanowire waveguides [63]. Other groups mapped out the near-field profiles in presence of disorder [50, 64]. They observed light localization around the band-edge of the waveguide and mapped the extinction length of the Anderson-localized cavities.

Several works from our group studied Anderson-localized modes with embedded emitters. The advantage of embedded emitters is the ability to excite the AL modes that are deeply embedded in

the waveguide. Smolka at. el. used the statistical distribution of the Q-factors of Anderson-localized cavities to discriminate the loss length and localization length in disordered PCW [62]. They studied samples with different amounts of extrinsic disorder. According to their results, the localization length and loss length on the samples with fabrication limited disorder are 7 µm and 600 µm respectively. It was also reported that the loss length decreases and localization length increases with increasing amount of disorder. García *et al.* studied the broadening of the Lifshitz tail versus different amounts of disorder [67]. They compared the results to the numerical simulations, successfully mapping the fabrication limited disorder to the uncertainty in the position of air holes in PCW. According to the results, the fabrication limited disorder is equivalent to 1.2nm uncertainty in the air hole position.

The other advantage of using samples with embedded emitters is to study the local density of states in the nanostructure. Sapienza *et al.* studied decay rate of single emitters embedded in disordered PCWs and observed strong enhancement of the decay rate of QDs due to coupling to the Anderson-localized modes [55]. The Anderson localization nature of the cavities was verified through the statistical distribution of intensity of the localized modes. The probability of entanglement between a single quantum dot and a photon in an Anderson-localized mode was investigated in reference [66], where a probability of 1% was found for parameters corresponding to recent samples and experiments. In addition, from the statistical distribution of Purcell factors the probability to observe largely enhanced decay rates was assessed.

The complex nature of multiple scattering of light requires a statistical approach that accounts for the statistical distribution of the relevant physical parameters describing the system. The main goal of this chapter is to give the first experimental study of the statistics of the decay rate of emitters embedded in disordered PCWs. We present statistical measurements of the decay dynamics of QDs in disordered PCWs both for the case where the cavities are probed directly and for the case that single quantum dots are tuned into resonance with Anderson-localized modes. The data sets provide two alternative ways of experimentally extracting Purcell factor statistics. In the first presented data set we measure the decay dynamics of the Anderson-localized modes and extract the fastest rate of the multi-exponential decay curves. This procedure records the rate of the quantum dot that is best coupled to this particular Anderson-localized mode while the detuning between the emitter and the cavity is not optimized. For the second data set, we tune a single quantum dot through resonance of an Anderson-localized mode. This uncovers the full potential of the Anderson-localized modes but at the expense that the measurements are time consuming thereby limiting the amount of statistical data that can be collected. From our measurements, we evaluate the light-matter interaction strength and compare the experimental data to the theoretically predicted distributions illustrating that the best observed cavities are at the onset of the strong-coupling regime.

In the second part of this chapter, we experimentally study the broadening of the Lifshitz tail and its position versus disorder. We create spectrally resolved, spatial maps of Anderson-localized cavities by scanning along the PCW. We observe a blue shift of the PCW mode with increasing amount of disorder. We also observed broadening of the Lifshitz tail by increasing disorder as expected. We compare our experimental results to theoretical predictions based on an eigenvalue expansion method. The experimental data helps identifying the more suitable model for the eigenvalue expansions. The

experimental data and theoretical predictions are in qualitative agreement.

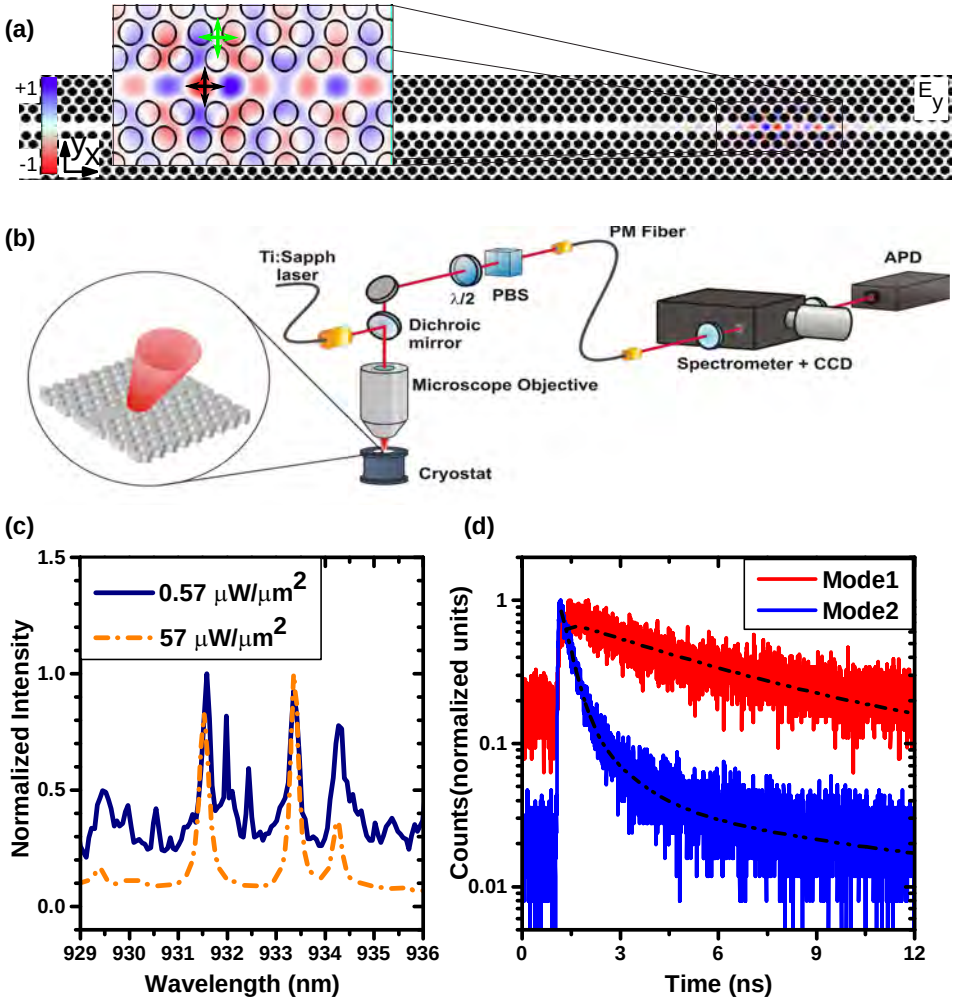

Figure 2.2: (a) Two-dimensional finite-element calculation of the E_y component of an Anderson-localized mode along a PCW with $\sigma = 1\%$ introduced disorder. The inset shows two dipoles placed at a node (green) and an anti-node (blueblack) of the cavity, thus experiencing a very different local density of optical states. (b) Sketch of the experimental setup. See main text for detailed explanations. (c) Emission spectra of the sample under high excitation power (dashed curve) showing the Anderson-localized modes, and under low excitation power (solid curve) showing Anderson-localized modes and quantum dot lines. (d) Examples of time-resolved photoluminescence decay curves of different Anderson-localized cavities fitted with multi exponentials (dashed lines). The pronounced differences in the decay times are attributed to the different spatial and spectral positioning of the dominant emitter feeding the cavities.

2.2 Quantum electrodynamical effects of Anderson-localized modes

In this section, we describe the experimental procedure and results showing the effect of Anderson-localized cavities on the local density of states in a PCW waveguide.

2.2.1 Experimental methods

The samples studied are 150 nm thick GaAs membranes with an embedded layer of self-assembled InAs quantum dots in the center with a density of 80 μm^{-2} that emit light in the 890 nm - 1000 nm wavelength range. A set of 100 μm long PCWs with a hexagonal lattice of holes and varying lattice constant (a) and hole radius (r) are etched in the membrane. All waveguides are at least 10 times longer than the measured localization length [62], assuring that Anderson-localized modes are formed near the cut-off of the waveguide mode. Various types of disorder likely contribute to the intrinsic disorder, including uncertainties in the positions and radii of the holes as well as surface roughness. Apart from the intrinsic fabrication imperfections in shape, size, and position of the holes, additional engineered disorder is introduced in the sample by randomly varying the position of the three rows of holes on each side of the waveguide according to a normal distribution with a mean value of zero and a variance of $\sigma \times a$, where σ is varied from 0% to 12% (cf. figure 2.1(a)). Figure 2.2(a) schematically represents two quantum dots at two different positions showing the two potential dipole orientations with respect to the E_y field component of an Anderson-localized mode in a PCW. To carry out the optical measurements, the sample is placed in a liquid Helium flow cryostat and cooled down to 10 K, see figure 2.2(b). A pulsed Ti:Sapphire laser with 5 pico-second pulse width emitting at 800 nm is focused on the sample through a microscope objective with NA = 0.55 from the top to a spot size of about 1.4 μm^2, and the emission from the quantum dots is collected through the same microscope objective. The cryostat is mounted on translational stages to control the excitation and collection spot with an accuracy of 100nm. The emission is polarization filtered with a half-wave plate and a polarizing beam-splitter, coupled to a polarization maintaining single mode fiber for spatial filtering, and sent to a monochromator with spectral resolution of 50 pm. The filtered light is finally detected with a CCD for spectral measurements or with an avalanche photo diode (APD) for time-resolved measurements.

In order to create wavelength resolved spatial maps of the Anderson-localized modes, we excite the sample with high-power aboveband which results in saturation of the single dots. The resulting inhomogeneous emission from the ensemble of quantum dots excites the localized modes efficiently. We move the collection spot along the waveguide and record the intensity of emission on the CCD of the spectrometer, see figure 2.2(b) for sketch of the experimental setup. We extract an approximate DOS by summing up all the observed intensities along the waveguide and normalizing it.

Time-resolved measurements are performed using two different approaches. In the first one, a set of waveguides with lattice constant a = 240nm, hole radius r = 74nm, and different disorder degrees (0-5% and 9%) are investigated, where the cut-off of the fundamental guided mode is at 930 nm. For high

pump powers (57 μW/μm^2), the spectral properties of the Anderson-localized modes are determined. The excitation power is then reduced to 0.57 μW/μm^2, cf. figure 2.2(c), which is close to the saturation power of a single quantum dot and time-resolved measurements are performed on the cavity emission spectrum. In such time-resolved measurements on the cavity peak, emission is recorded from all the quantum dots that are coupled to the cavity mode implying that the decay curves are generally multi-exponential. We concentrate here on the fastest component of the decay curves corresponding to emission from the quantum dot that couples best to the cavity. The measured decay curves (see figure 2.2(d) for representative examples) are fitted satisfactorily well with either single exponential, bi-exponential, or triple-exponential models after convolution with the 66 ps wide instrument response function of the setup acquired by sending the excitation laser reflected off the sample substrate through the setup. The same procedure is repeated for all of the observed Anderson-localized modes in the samples and very large variations are observed between different cavities. This procedure enables us to acquire a large data set for the statistical analysis, which provides a lower bound on the actual Purcell enhancement that can be obtained in the system, since the detuning between the quantum dots and cavity modes is not controlled. In the second approach, the Purcell factor is probed directly by time-resolved photoluminescence experiments on a single quantum dot emission line after tuning it into resonance with an Anderson-localized cavity by varying the temperature from 10 K to 30 K [68]. The fast decay rate originates from the recombination of the bright exciton of the resonant quantum dot. The Purcell factor is extracted by relating the measured decay rates to the average decay rate of 1.1 ns^{-1} obtained from quantum dots in a homogeneous environment. The optimum Purcell factor for a quantum dot perfectly matched spatially and spectrally to a cavity is given by $F_P = 3Q(\lambda/n)^3/4\pi^2V$, where n = 3.44 is the refractive index of the membrane and Q and V are the quality factor and mode volume of the cavity. From this relation, a conservative upper bound on the mode volume of the Anderson-localized cavity can be extracted. It is worth mentioning that intrinsic non-radiative processes give rise to a small residual recombination rate in the quantum dots, which in the case of radiatively suppressed quantum dots leads to an underestimation of the inhibition factor [36]. For the enhanced quantum dots, on the contrary, the non-radiative decay rate is usually negligible.

2.2.2 Far-field mapping of the Anderson-localized modes along the photonic-crystal waveguide

We reconstruct the spatial distribution of the Anderson-localized modes along PCWs for different amount of disorder. Figure 2.3 shows a sample scan along the waveguide with $\sigma = 2\%$ at the spectrum around the primary mode of the waveguide. The bright peaks in this figure correspond to Anderson-localized cavities. Several localized modes are observed while scanning the collection spot along the waveguide. The band-edge of this mode is around λ =933 nm. The Anderson-localized modes are spread around this value. These localized modes have Q-factors in the order of 3000. It is difficult to extract the spatial extent of the localized cavities from this data, since the crowded spectrum in figure 2.3. Previous work [62] estimated the localization length for $\sigma = 2\%$ to be around 4 μm (assuming a distribution of losses). The localized modes in figure 2.3 appear to extends in the range of few μms

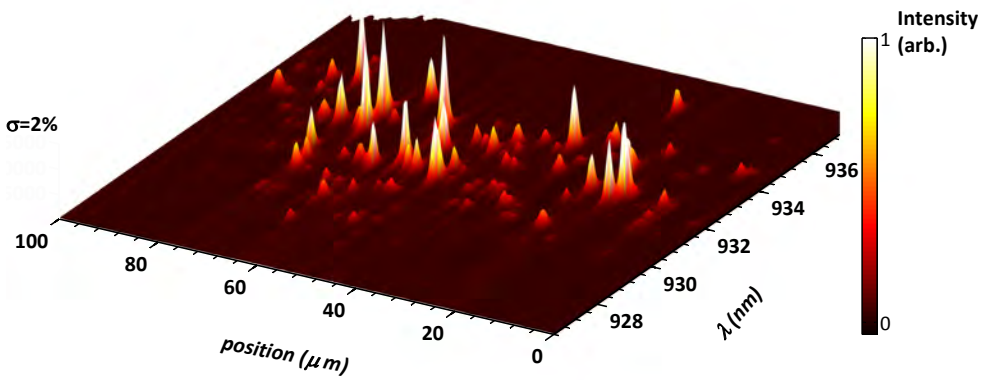

Figure 2.3: . Wavelength resolved spatial scan along the waveguide. We record the light intensity on a spectrometer while scanning the excitation and collection spot. The strong peaks along the waveguide are attributed to the Anderson-localized modes. The waveguide has 2% extrinsic disorder.

which qualitatively agree with the more accurate quantification in [62]. Next section presents the time-resolved analysis of emission from these localized modes.

2.2.3 Time-resolved measurements on Anderson-localized cavities

In this section, we present the experimental data of the spontaneous emission dynamics recorded when collecting light from the Anderson-localized cavities. We study the two different waveguide branches and for different degrees of disorder. We observe a distribution of Purcell factors reflecting the statistical distribution of coupling coefficients due to the random nature of the Anderson-localized cavities and the spatial and spectral matching of the quantum dot emitters to the cavities. Figure 2.4 shows the statistics of the measured Purcell factor. The histogram in figure 2.4(a) shows the case of the secondary waveguide mode which can be probed with the quantum dots by choosing a sample with $a = 260$ nm and $r = 78$ nm, and in this case we focus on $\sigma = 0\%$ (i.e., only intrinsic disorder). We observe an average Purcell factor of 1.7 together with a variance of 0.5. We stress that the Purcell factor obtained from these types of measurements constitute lower bounds of the actual Purcell factor of a quantum dot tuned into resonance.

We also study the fundamental waveguide mode while varying σ from 0% to 9%. For this purpose, a waveguide with parameters $a = 240$ nm and $r = 74$ nm is chosen, which has a band-edge at 932nm. The histograms in Figs. 2.4(b) to 2.4(d) include the experimentally extracted Purcell factor distributions for the waveguides with $\sigma = 0\%$, 3%, and 9%, respectively. The localized modes are found to span a spectral range between 3 nm and 7 nm. Compared to the measurements made at the high frequency waveguide mode, cf. figure 2.4(a), the Purcell factors are generally found to be considerably higher and have a broader distribution for the fundamental mode where also higher cavity Q-factors are observed, see insets of Figs. 2.4(a) to 2.4(d). The observed Purcell factors in this case range from 0.2 to 12, i.e., very pronounced suppression and enhancement is observed reflecting the broad range of coupling efficiencies found due to the statistical properties of the cavities. Figure 2.4(e)

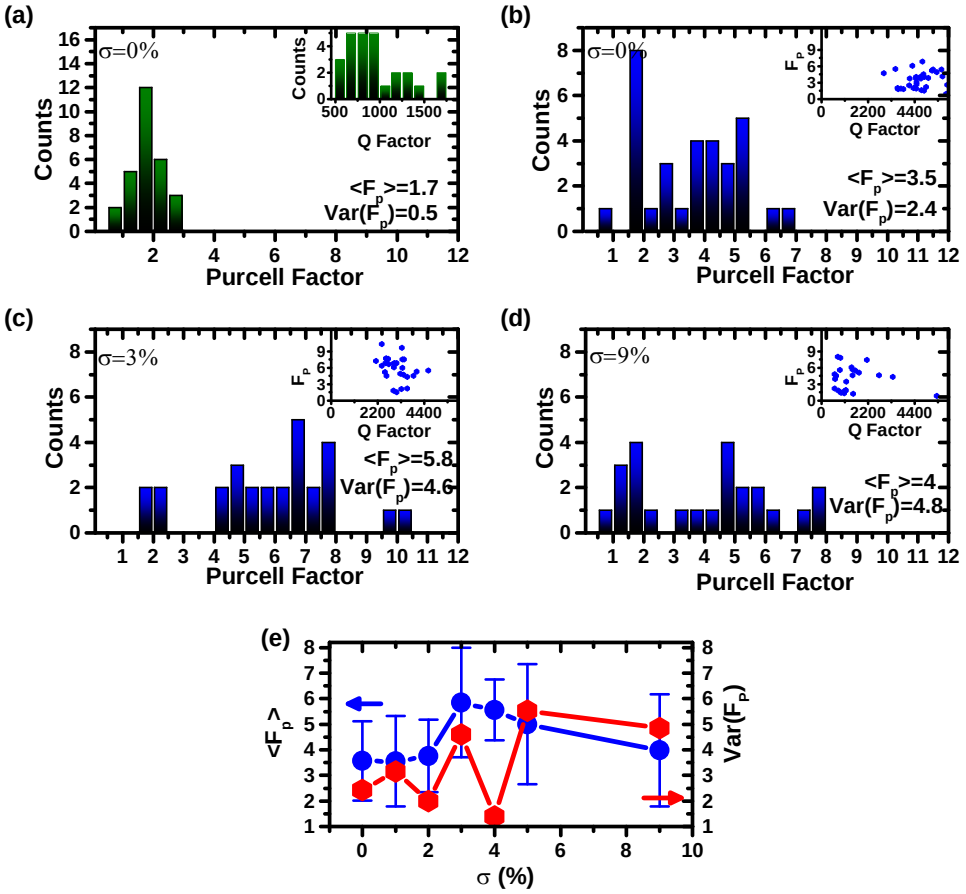

Figure 2.4: (a) Histogram of the measured decay rates from the Anderson-localized modes appearing along an unperturbed PCW ($\sigma = 0\%$) with a = 260 nm and r = 78 nm for the high-energy guided mode. The inset shows the histogram of the cavity Q-factors. (b),(c) and (d) Histograms displaying the Purcell factor measured on Anderson-localized modes for the fundamental guided mode of a PCW with a = 240 nm and r = 74 nm and for $\sigma = 0\%$, $\sigma = 3\%$ $\sigma = 9\%$, respectively. The insets show the measured Purcell factor vs. the corresponding cavity Q-factor. The lack of clear correlation between Q factor and decay rates is attributed to the uncontrolled spatial and spectral matching of the dominant emitter to the cavity. (e) Mean and variance of the measured Purcell factors vs. disorder degree for the data of (b)-(d). The variance is defined as $\mathrm{Var}(F_p) = \langle F_p^2 \rangle - \langle F_p \rangle^2$ and the error bars in $\langle F_p \rangle$ are the square root of the variance.

shows the mean and variance of the Purcell factor for waveguides with different amounts of disorder. The mean value of Purcell factor for individual distribution varies between 3.5 to 5.8 depending on the degree of disorder. There is also a clear trend in the mean value of Purcell factors versus extrinsic disorder. Increasing intentional disorder up to 3% tends to increase the mean value of the Purcell factor from 3.5 to 5.5 while further increase in the disorder amount decreases the mean value of the Purcell factor. The collected statistics reveal that there is a significant enhancement of light-matter interaction in the disordered medium.

We note that the uncertainty on each individual Purcell factor, due to the uncertainty in the fitting

routine of the decay rate, is in the range of $\Delta F_p \approx 0.4$. This value is smaller than the square root of the variance of the Purcell factor reported in figure 2.4(e). The variance of the Purcell factor distributions shown in figure 2.4(e) is due to the inherent statistical distribution of the Anderson-localized cavities including the random positioning of the individual QDs with respect to the cavities. While the former is determined by the amount of disorder in the structure [62], the latter is independent of disorder. The interplay between these two mechanisms gives rise to the non-trivial dependence of the variance of the Purcell factor with disorder in figure 2.4(e).

2.2.4 Time-resolved measurements on single quantum dots

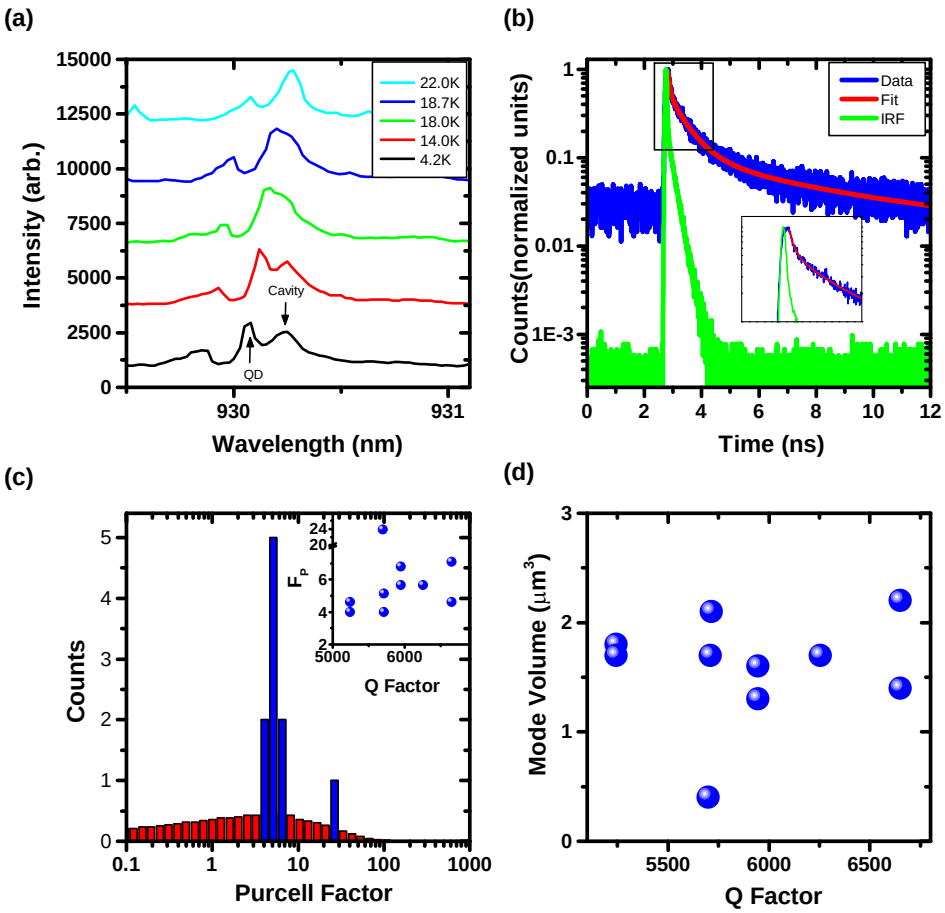

Figure 2.5: (a) Emission spectrum of the fastest quantum dot (Purcell factor of 23.8±1.5) while temperature tuning it through resonance of an Anderson-localized mode. (b) Decay curve recorded from the quantum dot in (a) at resonance with the cavity. The fit is shown as the solid red line. The green curve is the instrument response function(IRF) of the detector). (c) Purcell factor statistics obtained after tuning single quantum dots into resonance for a PCW with r = 69 nm, a = 230 nm, and $\sigma = 1\%$ (Blue histogram). The red histogram shows the theoretically calculated distribution using the theory in [66]. (d) Extracted upper bound on the mode volume vs. the corresponding cavity Q-factor.

In the previous section, we found a maximum in the average Purcell factor for quantum dots

coupled to Anderson-localized cavities appearing near the cutoff of the fundamental guided mode[1]. In order to measure the Purcell factor more precisely, the detuning between quantum dot and cavity is controlled through temperature and the decay rate is extracted on resonance. Figure 2.5(a) shows the spectrum of a single quantum dot while temperature tuning it across the resonance of an Anderson-localized cavity. We have repeated this procedure for a total of 10 different quantum dots along the PCW. The statistics are plotted in figure 2.5(c), where we observe Purcell factors in the range of 4 - 7 together with a quantum dot with a Purcell factor as high as 23.8. For comparison, the theoretically predicted distributions are also plotted in figure 2.5(c). The theory predicts a wide range of Purcell factors but the experiment has focused on extracting the large-value tail of the distribution due to the limited statistics available in the experiment. The inset in figure 2.5(c) plots the measured Purcell factors vs. the cavity Q, where no clear correlation is observed, which is attributed to the fact that the quantum dots are positioned randomly relative to the electric field of the localized cavities. Using the theoretical expression for the Purcell factor, we can estimate upper bounds on the mode volume of the individual Anderson-localized modes that are plotted in figure 2.5(d). The extracted values range between 0.5 to 2.2 μm^3, where we stress that spatial mismatch mentioned above will imply that these values are significantly overestimated, and likely to be consistent with the mode volumes in the range of 0.07 - 0.1 μm^3 recently obtained from random lasing experiments [58].

Finally, we analyze in detail the case of a Purcell factor of 23.8±1.5, shown in figure 4(b). In this case, the upper bound for the mode volume is 0.40±0.03 μm^3 and the spatial positioning and dipole orientation is likely to be close to optimal. The criterion for strong coupling between a quantum dot and a cavity is $g/\kappa > 1/4$, where $\kappa = 2\pi c/\lambda Q$ is the loss rate of the cavity, g is the coupling strength between the emitter and the cavity, c is speed of light in vacuum, and λ is the wavelength of the emitted photon. For this particularly fast quantum dot, this ratio is $g/\kappa = 0.130 \pm 0.004$, which indicates that the cavity is in the weak-coupling regime, but close to the onset of strong coupling. Another important figure-of-merit is the β-factor that specifies the fraction of recombination events of the quantum dot that leads to a photon in the cavity. An estimate of β is obtained by comparing the decay rate of the quantum dot when tuned away from resonance to the rate on resonance [38]. We obtained $\beta = 86\%$ for the highly enhanced quantum dot. This number is limited by the applied tuning range of the quantum dot in this experiment. From the measurements on other quantum dots that are suppressed and therefore not well coupled to cavity modes we estimate that a typical rate for coupling to other channels than the cavity would be 0.15 ns^{-1}. From such an estimate we conclude that the quantum dots are coupled to the Anderson-localized cavities with β-factors reaching as high as 99%.

2.3 Effect of disorder on the spectral position of band-edge

In addition to backscattering and Anderson localization, disorder is also responsible for the spectral shift of the PhC cavities and PCW bands [46, 47, 59]. It has been observed that the transmission of a PCW decreases and peak transmission blue shifts with increasing amount of disorder [59]. However,

[1]Data taken by Luca Sapienza and Henri Thyrrestrup

a band-edge shift is hard to observe in transmission-type measurements, since three different mechanisms, *i.e* Anderson localization, out of plane scattering, and photonic gap, reduce the transmission of the waveguide indistinguishably. However, spectral shifts in the position of the Anderson-localized modes clearly indicate a shift in the band-edge of the PCW.

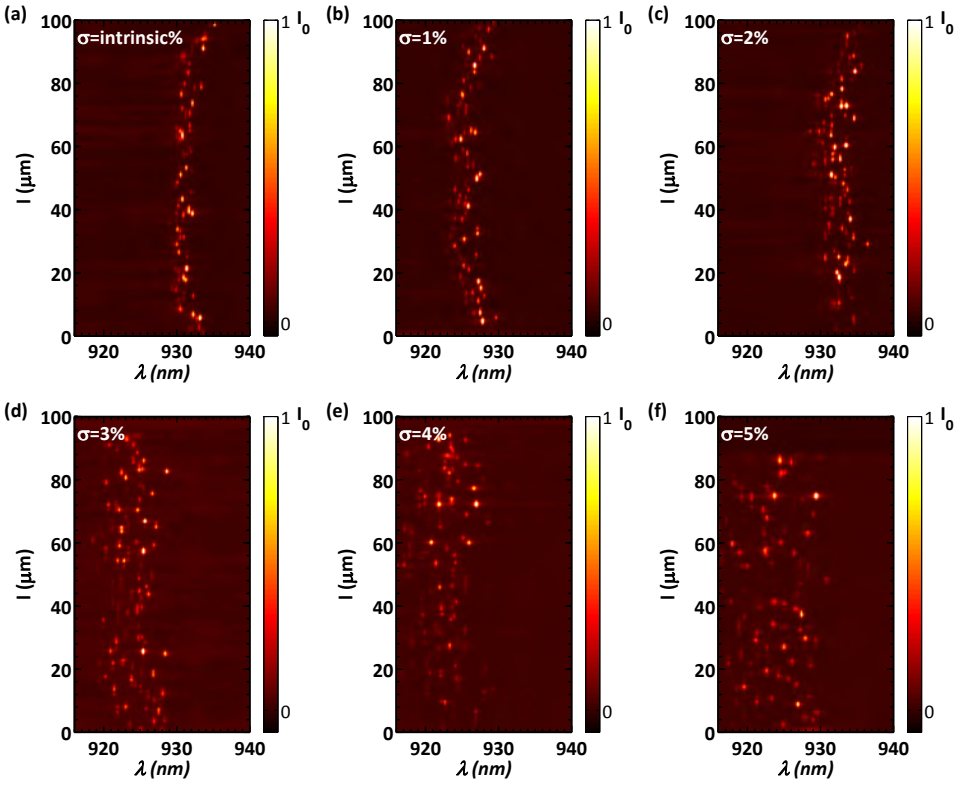

Figure 2.6: . Wavelength resolved spatial scan along the waveguide for six different amounts of extrinsic disorder. $\sigma = 0\%$ (intrinsic disorder) to 5% corresponding to (a) to (f). The y axis is the position along the waveguide and the x axis is the wavelength in free space. The spectral position of Anderson-localized modes, and hence the band-edge, appears to blue shift with increasing amount of σ. Broadening of the Lifshitz tail with increasing amount of disorder is also clear. Length of the localized modes increase with increasing Disorder in correlation with the increase in localization length observed before.

In this section, we map out the light scattered from the Anderson-localized modes along the PCW for waveguides with different amounts of disorder ranging from $\sigma = 0\%$ to $\sigma = 5\%$. The experimental method is described in section 2.2.1. Figure 2.6 shows the wavelength resolved spatial map along these waveguide. All these waveguides have the parameters a =240 nm and r =74 nm. However it is evident from figure 2.6 that the position of the Anderson-localized modes blue shifts with increasing amount of disorder. It is also worth mentioning that the waveguide with $\sigma = 2\%$ is an outlier to this trend. As expected from the theory in [67] the Lifshitz tail, increases with increasing amount of disorder and the localized modes appear over a broadened range.

Note that the area between $l = 0$ to 5 μm and also $l = 95$ to 100 μm appear to have slightly different band-edges compared to the rest of the waveguide. This is more clear for the three waveguides

$\sigma = 0\%$ to 2%. The reason for this shift is the edge effects present in this area. For all the conclusions drawn hereafter, these regions are neglected.

Fabrication related issues, such as scanning electron microscope proximity effects, and other mask production and etching steps can easily change the parameter of a PCW and cause shifts in the band edges. However, these effects are less likely to be the source of the shifts observed, since these effects are sensitive to larger area variations on the sample and the variations in the hole positions cancel out when averaged over scale of a waveguide.

2.3.1 Numerical modeling of disorder induce band-edge shift

In order to gain further understanding of the observed band shifts and to compare the shifts to the theory, we carried out numerical modeling. In reference [47], a mean blue shift and broadening of waveguide band-edge with disorder was predicted. The theory in reference [47] is an eigenvalue expansion method that takes into account the rapidly varying refractive index profile at the air and material interface. The mean shift of the band-edge is attributed to local field effects. This shift is absent when the slowly varying material/air interface assumption [69] is made. Full details about the modeling method can be found in [47, 70] [2].

The mean value of the waveguide band shift is given by [47, 70]:

$$\mathbb{E}\left[\Delta\omega^{(1)}\right] = -\frac{\omega_0}{2}\int_{cell}\mathbb{E}\left[E^*(r).P(r)\right], \tag{2.1}$$

where $E^*(r)$ is the electric field in the unperturbed eigenmode, $P(r)$ is the polarization function that characterizes disorder, and $\mathbb{E}$ is the ensemble averaging symbol. The variance of the band-edge shift can be calculated as:

$$\mathbb{E}\left[\Delta\omega^{(2)}\right] = \frac{\omega_0^2}{4}\int_{cell}\mathbb{E}\left[E^*(r).P(r)E^*(r').P(r')\right]drdr', \tag{2.2}$$

The choice of the right polarization model is very important to calculate these shifts correctly. Two models that have been widely used for modeling dielectric perturbations: weak-index contrast, and smooth-perturbation. We model $P(r)$ with the bump-perturbation polarization model with cylindrical bump shapes [69, 70]. This model is valid for abrupt interfaces of arbitrary shape which is the relevant type of perturbation in this work. As was noted in reference [47], resonance shifts in the band structure are due to local field effects and are not predicted by either the weak-index contract or the smooth-perturbation models. In contrast to [47], in this work the disorder is applied to the position of the holes, which is the relevant case for our experiments.

Since disorder shifts and broadens the mode edge, a useful quantity for experimental comparison is the density of states, DOS. To compute the DOS, we remind the reader that the definition of DOS bears close resemblance to the mathematical definition of a probability density function (PDF). We calculate DOS for a disordered PCW by creating a disordered band structure where $\omega(k) = \omega_0(k) + \Delta\omega(k)$.

[2] The numerical work has been done in Professor Stephen Hughes group in Queen's University and I am thankful to Nishan Mann for providing the data in figure 2.7(a).

$\omega_0(k)$ is the frequency corresponding to eigenvalue k of the perfect structure and $\Delta\omega(k)$ is a random variable with mean $\mathbb{E}\left[\Delta\omega^{(1)}\right]$ and variance $\mathbb{E}\left[\Delta\omega^{(2)}\right]$. The data set of $\omega(k)$ allows us to calculate the ensemble averaged DOS.

2.3.2 Comparison to experimental results

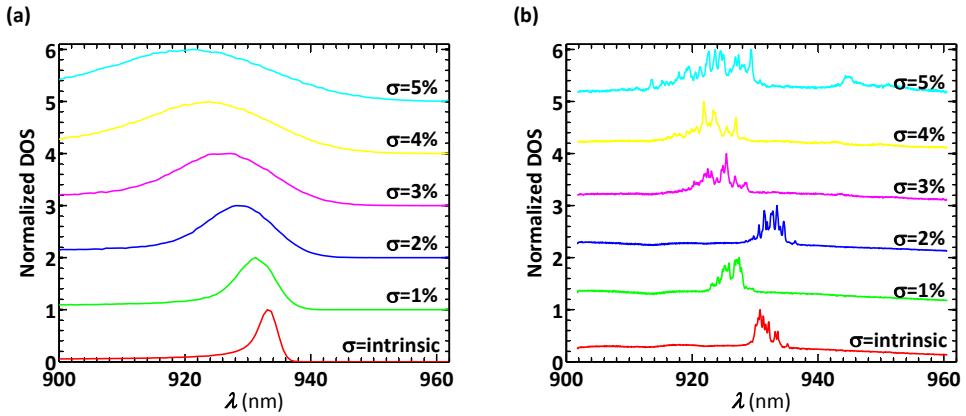

Figure 2.7: . (a) Theoretical curves showing LDOS in disordered PCW. (b) Experimental results showing DOS versus different amounts of disorder. The theoretical predictions qualitatively match the experimental results. Theoretical and experimental results show a blue shift for the band-edge with increasing amount of disorder.

We used the model described in the previous section to calculate the ensemble averaged DOS. Figure 2.7 shows the theoretical ensemble averaged DOS for waveguides with $\sigma = 0\%$ to 5%. We use the intrinsic amount of disorder for the case of $\sigma = 0\%$. For each waveguide, we ensemble average over 500 disorder instances. For all σ, the observed band-edge shift is towards higher frequencies. The band-edge broadens with increasing amount of disorder as expected. We note that the prediction of a mean blue shift is non-trivial and is solely due to the asymmetric polarizabilities present in bump perturbation polarization model.

Experimentally, the DOS can be extracted as an average LDOS over the spatial degrees of freedom. To do so, we integrate the data in 2.6 along the y axis and normalize the resulting spectrum to its maximum. Figure 2.7(b) shows the experimentally extracted DOS for $\sigma = 0\%$ to $\sigma = 5\%$. The experimentally extracted normalized DOS peak appears to blue shift and broaden with increasing disorder, in qualitative agreement with numerical predictions in part (a).

The lack of solid quantitative agreement between results in 2.7(a) and (b) can be attributed to several facts. First of all, the theory predicts the DOS for an infinitely periodic disordered unit cell and then does the ensemble averaging [47, 70]. This is an approximation for the experiments, since the actual waveguides are made up of unit cells with different instantiations of disorder. Secondly, the localized modes that form in aperiodic disordered waveguides do not appear in the periodically disordered waveguide case. And finally, multiple scattering becomes important for waveguides with $\sigma > 2\%$ and $N_g > 20$. Therefore, the periodic disordered model, provides and upper bound on the

mode edge broadening and a non-perturbative multiple scattering model would be needed to properly deal with the localized modes.

2.4 Conclusions

In this chapter, we have presented a statistical analysis of the emission dynamics from single quantum dots embedded in disordered PCWs. The measurement of the decay dynamics from the Anderson-localized modes enables efficient collection of a large amount of data. These measurements provide detailed insight about the statistical properties of QED in disordered PCWs. We observe a dependence of the distribution of the Purcell factor with the amount of disorder. We attribute this dependence to the interplay between the statistical distribution of the Anderson-localized modes and the random positioning of the individual QDs with respect to them. Measuring the decay rate of single quantum dots that are spectrally tuned across the cavities allows to reliably extract the Purcell factor. Hence, we observed Purcell factors in the range of 4-7 together with an extraordinarily large Purcell factor of 23.8 ± 1.5. The experimental data are compared to theory where a very broad distribution of Purcell factors is expected that cannot be fully resolved in the present experiment. This work demonstrates the promising potential of disordered nanophotonic structures for QED experiments and shows that the transition to the strong-coupling regime should be within experimental reach [71].

In the second section of this chapter, we spectrally mapped the Anderson-localized cavities in PCWs with various amounts of disorder. The spectral position of these mode appeared to systematically blue shift with increasing amount of disorder. Also the Lifshitz tail broadened with increasing disorder. From the spatial maps of Anderson-localized modes, we extracted the normalized DOS. We compared these results to numerical results based on bump-perturbation polarization model. A good qualitative agreement between the theoretical predictions of the band-edge shifts and the experimental results was observed. The inclusion of the local field effects for the correct prediction of band-edge shifts is crucial.

Chapter 3

Numerical modeling of quantum emitters in a modified local density of states

This chapter partly builds on reference [72]. As discussed in the introduction chapter, the density of states in a photonic crystal (PhC) is significantly modified compared to a homogenous medium. In this chapter, we study the local density of states (LDOS) in membranized photonic crystal nanostructures. We develop a 3D numerical model based on finite element method to simulate LDOS in PhCs and photonic-crystal waveguides (PCW). The method is used to extract detailed spatial maps of the LDOS in PhCs. For a PCW, the method is extended to separate the LDOS contribution from radiation continuum and the contribution from the PCW mode. We plot detailed spatial maps of coupling to the radiation continuum, and the β-factor. The results are compared to recent experiments. In the last part, the out-coupling from PCWs is considered. We model the far-field pattern of two different out-couplers that are normally used in the experiments. Our results show that the coupling efficiency between a PCW and embedded dipoles is close to unity (>90%) for a wide range of frequencies and spatial positions of the dipole. The results in this chapter highlight potential of two level emitters embedded in PCWs as robust 1D atoms.

3.1 Introduction and literature review

The environment of an emitter can drastically modify its emission dynamics. It was first predicted by Purcell that placing an emitter in a cavity would increase its decay rate [73]. A change in the decay of the emitter close to planar interfaces was first observed by Drexhage [74]. Two decades later, the enhancement of microwave transitions of Rydberg atoms in high-Q cavities was reported [75]. Around the same time it was realized that the spontaneous emission rate of a quantum emitter can

also be suppressed by placing it in a photonic band gap [10, 76]. These led to a significant effort in understanding and controlling the effect of the environment around a quantum emitter. The strong coupling of an atom to a single mode of a cavity, where interaction between a single mode is much stronger than rest of the modes, was subsequently observed [77, 78]. Theoretically it was predicted that the spontaneous emission rate of a quantum emitter can also be suppressed by placing it in a photonic band gap [10, 11, 76]. Further theoretical work has concentrated on detailed understanding of the effect of the environment on decay dynamics of a quantum emitter [79–85].

Quantum dots have a particular advantage when it comes to engineering the photonic environment around them. The first experiment demonstrated a Purcell enhancement of 5 with quantum dots in micropillars cavities [86]. In the last decade enhancement and inhibition of emission from single quantum dots in inverse-opal photonic crystals [34], membrane photonic-crystal cavities [35, 87], and micropillars cavities [88,89] was experimentally demonstrated [90]. Several groups also achieved strong coupling between single quantum dots and different nanostructures [37, 91–93]; see [94] for a review of this topic.

Further theoretical studies demonstrated the possibility of strong modification of spontaneous emission from quantum emitters in photonic crystals with partial band-gap (photonic-crystal membranes). Koenderink, *et al.* numerically showed that, it is possible to strongly inhibit emission from quantum emitters in the band gap of a triangular photonic-crystal membrane [81]. Later, Wang *et al.* measured inhibition factors of up to 70 in the bandgap of photonic-crystal membranes [36, 95].

It was proposed that photonic-crystal waveguides can enhance the emission rate of a dipole to the single mode of the waveguide [96] over a very broad bandwidth. Also, it was understood that the combination of inhibition of the radiation to the membrane modes and the enhancement of the radiation to the waveguide mode, results in most of the emission from the emitter to funnel into the single mode of the waveguide [97, 98].

The ratio of the power coupled to the waveguide mode over the total power emitted from the emitter is defined as "β-factor". A high β-factor is desirable for most of applications and particularly to realize a 1D atom. Several experiments have shown very high β-factors for single quantum dots in photonic-crystal waveguides. Lund-Hansen et el. reported β-factors of up to 89%. Since, several groups have measured β-factors as high as 98% for quantum emitters coupled to single guided modes [22,23,99–102].

This chapter is organized as follows: We first review the equations governing the dynamics of spontaneous emission of an emitter in an arbitrary medium. The second section gives an overview of the finite element method (FEM) and its application to solution of partial differential equations. Next, we apply frequency domain FEM in 3D to calculate the local density of optical states in a PhC and derive detailed spatial maps for LDOS in the bad gap of PhC. The section 3.5 aims at calculating the LDOS in a PCW and separating the contributions from primary guided mode and the radiation continuum. We develop special Dirichlet boundary conditions to deal with the boundaries of the waveguide and to reduce the reflections from simulation domain boundaries. We create spatial maps showing the position dependence of the coupling to the leaky modes and the spatial map of coupling efficiency to the waveguide mode. We briefly discuss the relevance of these simulations for

recent experiments. In the last part of this chapter we consider out-coupling from PCW and calculate far-field patterns of second order Bragg gratings and inverse taper out-coupler.

3.2 Spontaneous emission rate of a quantum emitter

The interaction of a two level emitter with a reservoir of electromagnetic modes is described by the Jaynes-Cummings Hamiltonian [103].

$$\hat{H} = \sum_k \hbar\omega_k \hat{a}_k^\dagger \hat{a}_k + \frac{1}{2}\hbar\omega_0 \hat{\sigma}_z + \sum_k \left[\hbar g_k \hat{\sigma}_+ \hat{a}_k e^{i(\omega_0-\omega_k)t} + \text{h.c.}\right], \tag{3.1}$$

where $\hat{a}_k$, $\hat{a}_k^\dagger$ are annihilation and creation operators, for mode k, $\hat{\sigma}_z = |e\rangle\langle e| - |g\rangle\langle g|$, $\hat{\sigma}_+ = |e\rangle\langle g|$ are the emitter-population operators. The coupling strength between the emitter and the mode k of the reservoir is $g_k(r_0) = i\vec{d}\cdot\hat{E}_k^\dagger(r_0)/\hbar$, where $\hat{d}$ is the dipole moment of the emitter, $\hat{E}_k = \sqrt{\frac{\hbar\omega_k}{2\epsilon_0}}\hat{u}_k(r)$, and $\hat{u}_k(r)$s are eigenvectors of the nanostructure and satisfy the normalization condition $\int dr^3\epsilon(r)\hat{u}_k(r)\cdot\hat{u}_k(r)^* = \delta_{kk'}$.

The equation of motion for the population of the excited state of the emitter can be simplified as [30]:

$$\frac{\partial c_{\text{e}}(t)}{\partial t} = -\frac{d^2}{2\epsilon_0\hbar}\int_0^\infty d\omega\,\omega\rho(r_0,\omega,\hat{e}_d)\int_0^t dt' c_e(t')e^{i\Delta(t-t')}, \tag{3.2}$$

where $c_{\text{e}}(t)$ is the probability amplitude of the emitter being in the excited state, $\Delta = \omega_0 - \omega$, d is the amplitude of $\hat{d}$, and ρ is the local density of states (LDOS) which is defined as [30, 104, 105]:

$$\begin{aligned}\text{Im}\left[\hat{e}_d^*\cdot\overleftrightarrow{G}(r,r,\omega)\cdot\hat{e}_d\right] &= \frac{\pi\omega}{2}\sum_k |\hat{e}_d\cdot\hat{u}_k(r)|^2\,\delta(\omega-\omega_k)\\ &= \frac{\pi\omega}{2}\rho(r,\omega,\hat{e}_d).\end{aligned} \tag{3.3}$$

$\hat{e}_d$ is a unit vector oriented along the dipole moment, $\overleftrightarrow{G}(r,r,\omega)$ is the Green's tensor and is defined as the solution to the Helmholtz equation with a delta current source located at r' [30].

Under Wigner-Weisskopf approximation equation 3.2 simplifies to :

$$\begin{aligned}\frac{\partial c_{\text{e}}(t)}{\partial t} &= -\Gamma c_{\text{e}}(t),\\ \Gamma &= \frac{\pi d^2}{\epsilon_0\hbar}\omega_0\rho(r,\omega,\hat{e}_d).\end{aligned} \tag{3.4}$$

where Γ is the radiative decay rate of the emitter in the medium.

It is often appealing to compare the decay rate of an emitter in a nanostructure to its decay rate in a reference medium. The Purcell factor is defined as $F_p = \Gamma/\gamma_0$, where γ_0 is the decay rate of emitter in a reference medium. This allows to cancel out the trivial dependencies on oscillator strength and frequency. The decay rate of an emitter in a homogenous medium is $\gamma_0 = \frac{n\omega^3|d|^2}{3\pi\epsilon_0\hbar c^3}$, where n is the refractive index of the homogenous medium. Hereafter, the term Purcell-factor and normalized LDOS are used interchangeably, since this is implied by definition of Purcell factor.

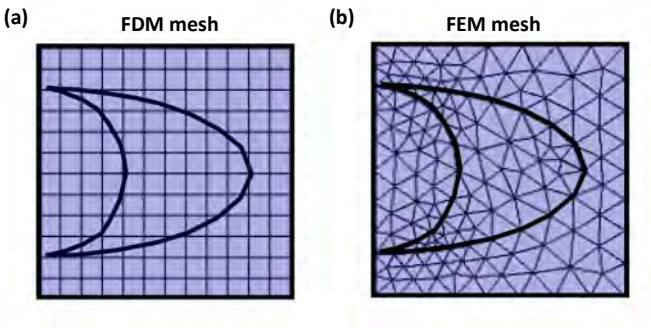

Figure 3.1: A typical mesh (a) for FDM modeling, and (b) for FEM modeling of a 2D problem. Finite element mesh is much more accurate in resolving the sharp edges.

It is challenging to get analytical solutions for Green's tensor for most $\epsilon(r)$ configurations, and one has to revert to numerical methods for a solution. In this thesis, we use finite element method to numerically calculate the projected local density of states for various 3D photonic crystal nanostructures.

3.3 Preface to finite element modeling

In this section, we briefly introduce the finite element modeling and concepts and related concepts. Different approaches for obtaining numerical solution of the differential equation:

$$\mathcal{L}\{u\} = f(u, r), \tag{3.5}$$

have emerged since the 1950s. In this equation $\mathcal{L}$ is the differential operator of order m, vector $r \in \mathcal{R}^n$ is the vector of n independent variables, and u is the dependent variable. Most approaches are based on discretizing the generally continuous domain of the $r \in \mathcal{R}^n$ to $r_i \in \mathcal{N}^n$, where $\mathcal{N}$ is a finite numerable subset of $\mathcal{R}$. The subdomain $\mathcal{N}^n$ is called a mesh.

The next task is to find u_i so that $u_i \approx u(r_i)$. The initial approach was to choose $\mathcal{N}^n = \mathcal{N}_1 \otimes \mathcal{N}_2 \otimes ... \mathcal{N}_n$. This approach is called finite difference method (FDM). Following this approach the operator $\mathcal{L}$ can be converted to an algebraic sum of the u_is. Hence, the equation 3.5 can be converted to linear system of equations and solved respectively. This approach provides very powerful tool to solve differential equations, however the discretization of the domain $\mathcal{R}^n$ is limited to rectangular meshes which is a draw back when dealing with complex geometries [106, 107], see 3.1 for a typical FDM mesh.

The alternate approach is to discretize the $\mathcal{R}^n$ to a set of subdomains. The geometry of the subdomains are not restricted to rectangles and can be any polyhedrons. The common shapes for the mesh elements are tetrahedrons and hexahedrons in 3D case. There are several formulations for solving equation 3.5 using an inhomogeneous mesh. The core of these formulations is to convert

equation 3.5, called the "strong form", to a an integral form.

$$\int_{\Omega} \mathcal{L}\{u\}v - \int_{\Omega} f(u,r)v = 0, \tag{3.6}$$

where Ω is the modeling domain and v is an arbitrary function.

Equation 3.6 is called the weak form. It is possible to prove that if u satisfies the weak form equation for any v, it is a solution to the strong form also. Often, depending on the nature of $\mathcal{L}$, Gauss or Green's formula is applied to equation 3.6 to soften the requirement on the continuity of u and also to lower the rank of $\mathcal{L}$. For example consider the equation

$$\nabla.(-c\nabla u) = f. \tag{3.7}$$

The weak form of this equation simplifies to:

$$\int_{\Omega} c\nabla u.\nabla v - \int_{\Omega} fv - \int_{\partial\Omega} c\nabla u.nv = 0. \tag{3.8}$$

The third term in this equation is the boundary condition requirement. A solution u to the above equation needs to be differentiable just once, while the solution to the original equation needs to be twice differentiable with respect to independent variables. In principle, the solution u to equation 3.8 should be tested for all v defined over $\mathcal{R}^n$ [108]. However, this is practically impossible and normally u is tested against an orthonormal set of functions e_{ji}, where subscript i refers to the mesh element and j runs over the orthonormal set [107]. Often one chooses the set e_{ji} so that each e_{ji} is only nonzero over element i [107]. Also, following Galerkin's method, and without loss of generality, u_i is written as:

$$u_i = \sum_j C_{ij} e_{ji}. \tag{3.9}$$

Inserting equation 3.9 to 3.6, the integro-differential equation 3.6 can be turned to a system of linear equations. Note that the e_is are local to mesh elements and $\int_{\Omega} e_{i\Omega_a} e_{j\Omega_b} = \delta_{ij,ab}$ [107].

For the mesh element i, the size of $\{e_{ji}\}$ determines the order of element, or in other words, the number of degrees of freedom for the mesh element. Obviously, the accuracy of the solution depends on the size of $\{e_j\}$. It is very important to check the accuracy of the solution set $\{u_i\}$. A convergence is reached when the solution does not depend on the size of $\{e_j\}$ within certain deviations.

The main advantage of FEM over FDM is at dealing with complex structures. Due to the flexible shape of the elements, FEM is able to resolve the geometry of the structure with much better accuracy, hence the results of the solution converge at much bigger element sizes than that of the FDM [106,107]. Figure 3.1a and 3.1b show a complex object with FDM and FEM meshes in the background. As it is clear, FEM resolves the geometrical features of the object much better, thanks to its flexible mesh.

On the other hand, the linear system of equations resulting from FEM are generally harder to solve and require careful ordering of the elements in the solution matrix. Also meshing the simulation domain into smaller subdomains is challenging and requires smart meshing strategies.

Fortunately, a wide range of commercial and open-source FEM packages are available that deal with the numerical complexities, ANSYS, COMSOL, and Maxwell, to name a few. For the propose

of this thesis we will be using a commercially available package, COMSOL. The software package has a wide range of tools dedicated to electromagnetic problems. The package has features to handle the problem of meshing the simulation domain and also provides access to a wide range of direct, iterative and preconditioned iterative solvers among many other features.

3.4 Decay rate of a dipole in a photonic crystal

As discussed in 1.2, a PhC is a highly dispersive and the mode density is very different from homogenous media. Figure 3.2 shows the band diagram of a membrane photonic crystal along the Brillouin zone edge. The membrane guided modes, solid black lines in figure 3.2 , are bounded to the PhC membrane by total internal reflection. The blue area in figure 3.2 corresponds to the radiation modes. These modes are not bound to the membrane and leak to the surrounding environment. Also note that these modes are present at all frequencies. In general, the decay rate of an emitter is a sum of contributions from these to set of modes, $\Gamma = \Gamma_{\text{membrane}} + \gamma_{\text{rad}}$.

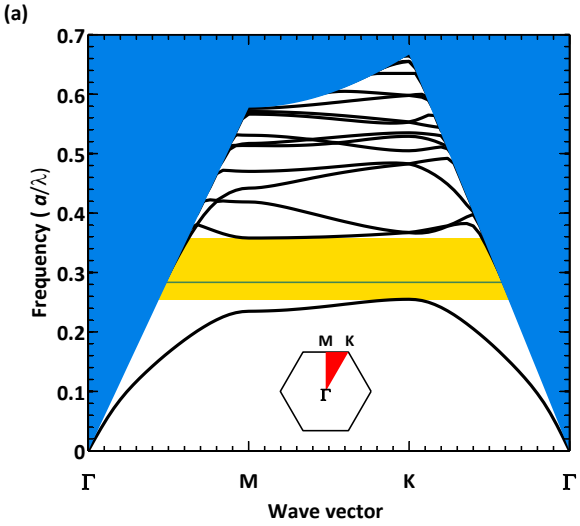

Figure 3.2: Dispersion diagram of a PhC membrane along the border of the irreducible Brillouin zone for transverse electric modes. The blue shaded areas represent the light cone. The yellow region is the partial band gap of the structure. The red triangle represents the irreducible Brillouin zone. The green line indicates the frequency studied in 3.4.

The yellow area in 3.2 is the band gap of the PhC. For this energy range the membrane guided modes are suppressed. That means the only channels for an emitter to decay are the radiation modes, $\Gamma = \gamma_{\text{rad}}$.

It is challenging to calculate all the eigenvectors of such a band diagram, since it involves discretizing the continuum of the radiation modes. As a result, we solve the full 3D Maxwell's equation for a small current element which represents a dipole emitter. We post process these solutions to calculate the power emitted by the current element and extract the normalized LDOS (F_p). The next section

describes details of the simulations.

3.4.1 Details of implementation

As mentioned in the previous section the approach in this thesis is to solve the inhomogeneous Maxwell's equations rather than eigenvalue expansion. We extract Γ for two orthogonal in-plane dipole orientations, x and y that are located in the center of waveguide. However, the approach presented in this section is general and can be used for any type of in-plane dipoles.

We calculate the LDOS in different photonic crystal nanostructures by solving the inhomogeneous Helmholtz equation for a classical dipole numerically using frequency domain FEM. We model the dipole with a very small current element J_0 running in direction $\vec{e}$, $\vec{e} \in \vec{x}, \vec{y}$. The total power emitted from this current source is proportional to the decay rate of a quantum emitter with dipole strength d at the position of the source

$$\Gamma = \frac{Pd^2}{\hbar\omega^3 J_0^2}. \tag{3.10}$$

This equation can also be written as $P/P_0 = \Gamma/\Gamma_0$, where Γ_0 and P_0 are the respective decay rate of quantum emitter and power radiated from a classical current source in a homogenous medium. The total power emitted from this dipole can be extracted as $P_{\text{total}} = 1/2Re[J_0 \int_L \vec{E}.dl]$, where the integration is a line integration over the length of the current element [85] or for a point dipole as $1/2Re[\vec{J_0} \cdot \vec{E}]$ [81]. J_0 is the amplitude of the vector $\vec{J_0}$. These equations are equivalent to integrating the Poynting's vector over a closed surface around the current source.

$$P_{total} = 1/2Re[\oint_s \vec{E} \times \vec{H}^\dagger \cdot \vec{ds}] \tag{3.11}$$

For all the simulations in this thesis we consider dipoles that are oriented in the plane of the membrane, x-y plane in figure 3.3 and are located in the center of membrane. Since the symmetry of the structure across the plane $z = 0$, the solutions of Maxwell's equations also have the mirror symmetry across the $z = 0$ plane and ($E_z(z = 0) = 0$ and $\frac{\partial}{\partial z}\{E_x, E_y\}|_{z=0} = 0$). In other words, the dipoles that are oriented in plane of the PCW and are positioned in the center of the membrane do not couple to the TM modes. As a result, the simulation domain can be cut to half along $z = 0$.

Figure 3.3 show the simulation domain for a PhC membrane, with lattice constant a and hole radius r. The simulation domain consists of a PhC membrane (colored gray in figure 3.3), an air box of height h, and perfectly matched layers (PML) [109]. The blue box in figure 3.3 is the PML, which absorbs the incoming waves. The red box in figure 3.3 inset, depicts the surface s in equation 3.11, used for extracting the total power emitted by the dipole. The refractive index of the PhC membrane is assumed to be 3.5 corresponding to refractive index of GaAs around 900 nm at 10 Kelvin. Table 3.1 contains the parameters characterizing the simulation domain.

The photonic crystal is terminated in the homogenous membrane which in turn is terminated by PMLs to absorb the light escaping from the PhC. One should note that the interface between

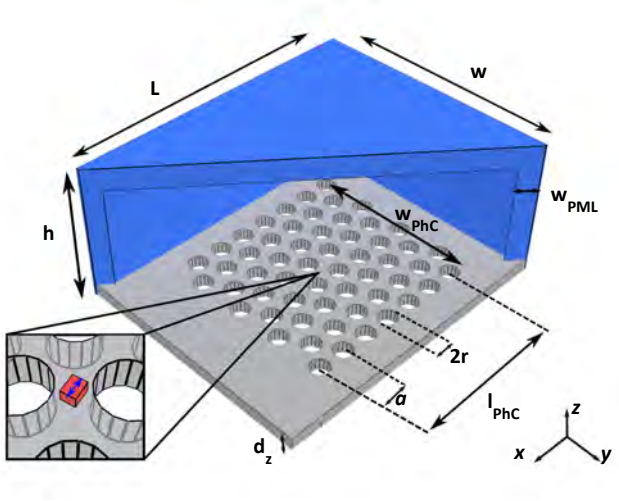

Figure 3.3: Cut through view of the simulation domain. The blue box around the membrane is the PML. The PMLs cover air boundaries and the material boundaries. The inset shows a zoom in on the location of the dipole. The double sided arrow shows the current element. Poyinting's vector integrated over the red box gives the amount of power radiated from the current source. Note that d_z is half of the actual membrane thickness due to symmetry conditions across $z = 0$. The dimension in the figure are not to the scale.

Table 3.1: Parameter list for the simulation domain of the dipole in PhC membrane.

Parameter	l	w	h	d_z	l_{PhC}	w_{PhC}	w_{PML}
Value	$4.2\mu m$	$5.1\mu m$	$1.6\mu m$	$80nm$	$15a$	$9\sqrt{3}a$	$0.5\mu m$

the homogenous membrane and the PhC can give rise to finite size effects. However, for the case of PhC membrane, we are mainly interested in the frequency range of bandedge, where the in-plane light propagation is negligible for sufficiently large PhCs. The PMLs are effective for the waves in homogenous medium, so the light radiated to the air domain gets absorbed by them.

3.4.2 Results

In order to map the spatial dependence of the Purcell factor in the PhC membrane, we run the simulations for different dipole positions inside the cubic unit cell and extracted the corresponding F_p. Figure 3.4(a) and (b) show the position dependence of projected LDOS for a dipole in the band gap of the PhC. As expected, the radiative decay of the emitter is inhibited due to reduced density of optical states. As evident from 3.4(a) and (b)the F_p in the band gap strongly depends on the position of the emitter and its orientation. For optimally located dipoles, the radiative decay is inhibited by factors of around 160.

These results compare nicely with the theoretical results reported by Koenderink *et al.* [81], where finite difference time domain was used. The main challenge in time domain simulations is to accurately

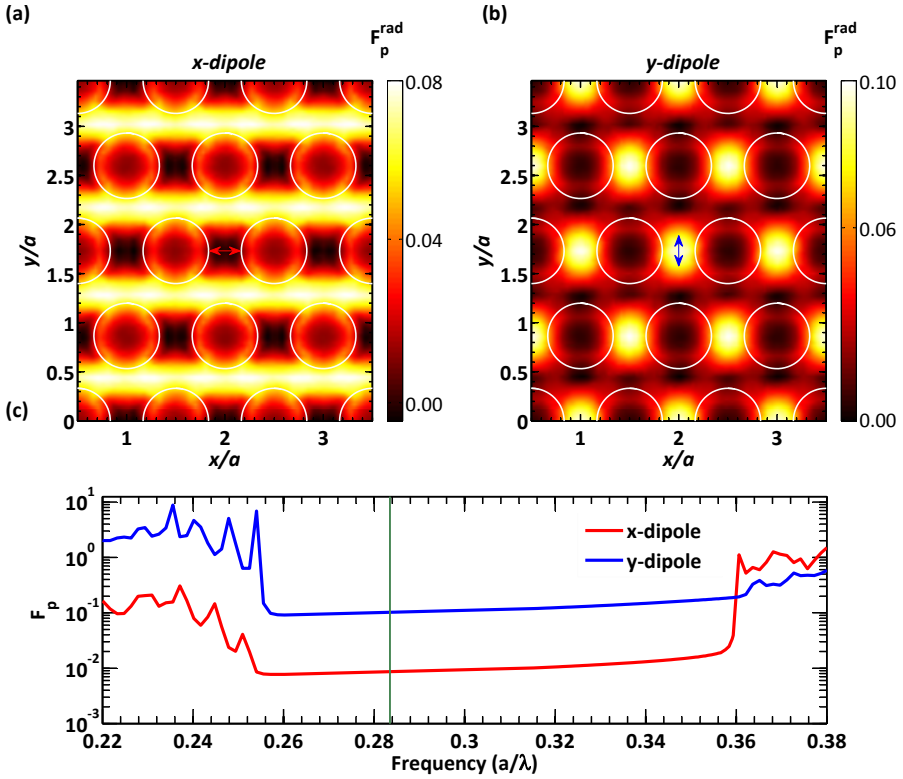

Figure 3.4: (a) and (b) Spatial maps for Purcell factor (normalized LDOS) of an emitter in the band gap of a PhC membrane, (a) for a x-oriented emitter, and (b) for a y-oriented emitter. The frequency of the emitter corresponds to the vertical green line in part (c) of this figure. The γ_0 is assumed to be the decay rate of an emitter in homogenous material with $n = 3.5$. The radiative emission for the emitter is suppressed by factors of up to 160 depending on the position of the dipole. (c) Frequency dependence of F_p for x- and y-oriented emitters, positioned at the points depicted by arrows in parts (a) and (b).

transform the power emitted by the dipole from time domain to frequency domain. When comparing the results with [81], one should note that the results in [81] are normalized to radiation from the emitter in air.

Figure 3.4(c) shows the frequency dependence of the F_p for a dipole positioned in the point of arrows in Figures 3.4(a) and (b) for the two orientations x (red line), and y (blue line). As expected the F_p varies very slowly in the band gap of the PhC for both dipole orientations and the high inhibition is maintained for all of the band gap. For the frequency ranges outside the bandgap there is a significant coupling to the TE modes present which results in a increased decay rate of the emitter. The residual LDOS at frequencies of ban gap is due to coupling to the radiation continuum.

It is also instructive to look at the field profile resulting from the dipoles located in the band gap. Figure 3.5 shows the norm of electric field for two different dipole orientations. The coupling between the dipole and evanescent modes results in these mode profiles. This observation can be interpreted as dipole induced localization of light in the band gap [110]. These localized modes might be interesting

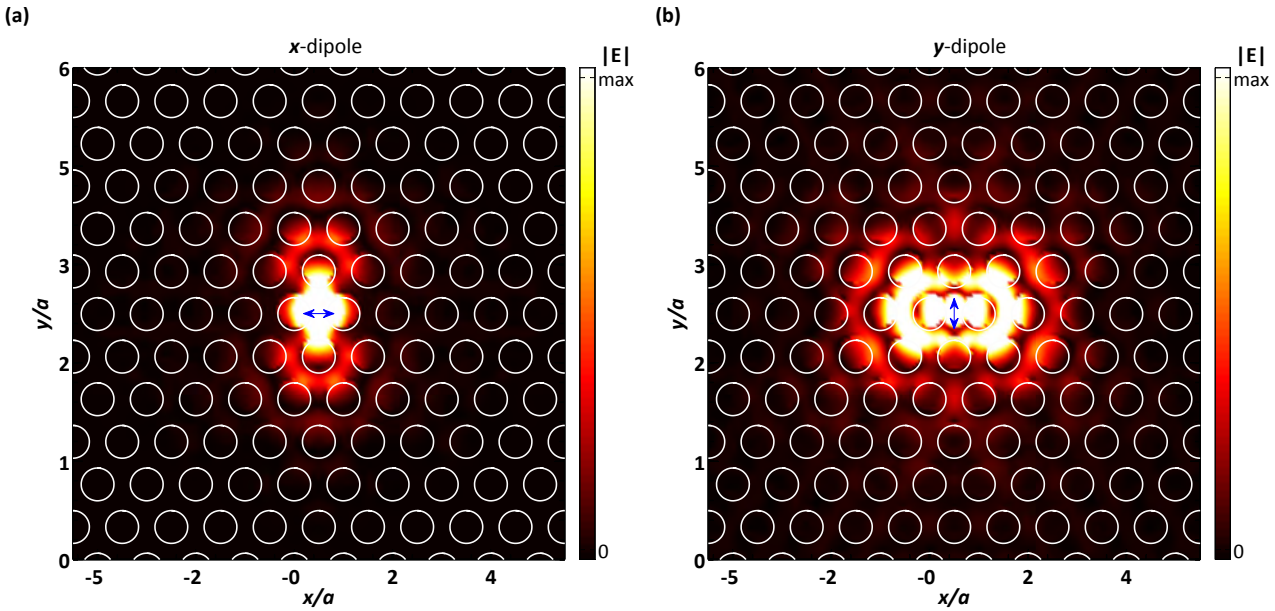

Figure 3.5: Field profile for x- and y-oriented dipoles at band gap frequencies. The dipole couples to a set of evanescent modes which form the field profiles above. These mode can also be interpreted as dipole induced localization of light.

for different QED proposes, e.g. coupling of two atoms or quantum dots. Also note that the loss rate from these cavities is $F_p\gamma_0$ of the quantum emitter responsible for the localization. The localized modes formed around an InAs QD, have Q-factors in the range of 10^7. This value is a conservative estimate based on experimental results.

These results further shed light on the potential of photonic crystals for QED applications where they open a possibility to efficiently interface a single emitter.

3.4.3 Connection to the experimental results

It is interesting to compare the results of simulations in this section to some of the reported in recent experiments [36, 111]. Julsgaard *et al.* measured decay rate of ensemble of quantum dots in a PhC for different frequencies. They observed an average inhibition of factor of 6 for the emission inside the band gap [111]. Wang *et al.* studied the decay rate of single quantum dots in the center of a PhC membrane. They observed that the radiative component of the decay rate of the single quantum dots was suppressed inside the band gap of a PhC compared to a uniform membrane. The average inhibition observed was around 20. They also reported suppressions as high as 70 for quantum dots inside the band gap [36]. These results lie within the theoretical calculations in the previous section.

3.5 Electrodynamics of a dipole in a photonic-crystal waveguide

In this, section we study LDOS in a PCW and discriminate contributions from different modes. Figure 3.6(a), shows the band diagram of the TE modes for a membrane PCW. The propagation of light in a PCW is governed by Bloch theorem [12]. The Bloch modes have the periodicity of the crystal lattice in the direction of the waveguide with a phase factor, $\vec{E}_{\text{Bloch}} = \vec{E}_{\text{wg}} e^{ikx}$, where $\vec{E}_{\text{wg}}$ is periodic over unit cell. Moreover, inside the band gap of the photonic crystal, light is mainly guided by three highly confined modes, and for a major part of the spectrum light transmission is single moded (figure 3.6(a), solid black lines). Light propagation in the individual waveguide modes is highly dispersive. The propagation velocity of the wave is reduced as its frequency approaches the band-edge and the group index of the propagation theoretically diverges. Since the partial band gap of the PCW, there exist a continuum of modes that are not confined to membrane and leak to the surrounding environment (blue area in figure3.6(a)). In the context of light propagation, disorder in the PCW couples the guided modes of the PCW and the continuum which leads to leaks and propagation losses in the PCW as discussed in 2. In what follows, we study the effect of different modes of the band structure on the decay dynamics of embedded quantum emitters.

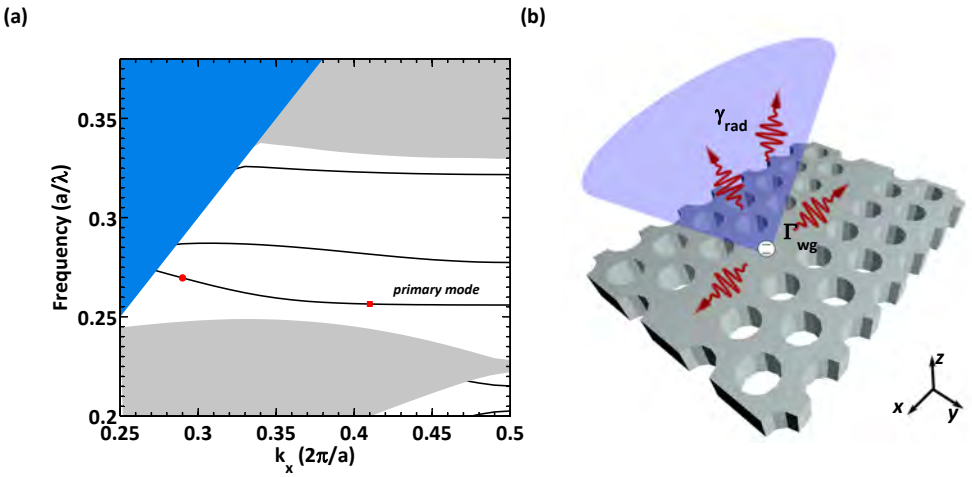

Figure 3.6: (a) Band diagram of a PCW membrane for TE modes. The solid black lines are the TE guided modes of the waveguide. The gray regions mark the membrane guided modes of the structure. The blue region is the continuum of the radiation modes that are not bounded to the membrane at all. The red circle and square mark the frequencies corresponding to $N_g = 5$ and $N_g = 58$ respectively. (b) The sketch of a quantum emitter in the middle of a PCW showing the coupling to radiation modes and to the bounded mode, blue region and solid black lines in part (b) of this figure.

The modes in figure 3.6 can be classified into three categories, the guided modes of PCW (the solid black lines in figure 3.6(a)), the membrane guided modes (the gray region in figure 3.6(a)) and the continuum of the radiation modes (colored as blue in figure 3.6(a)). At each frequency, the total decay rate of the emitter can be written as a sum of the contribution from these three set of modes

plus contributions from coupling to TM modes:

$$\begin{aligned}\Gamma_{\text{emitter}} =&\Gamma_{\text{wg}}(w)+\\ &\gamma_{\text{rad}}(w)+\gamma_{\text{membrane}}(w)+\gamma_{\text{TM}}(w).\end{aligned} \tag{3.12}$$

As discussed before, we are mainly concerned with dipoles that are located in the center of the membrane and oriented in plane of the membrane, and hence do not couple to antisymmetric modes of the membrane (TM modes). The frequency range of interest for a PCW is also mainly the region around the primary guided mode. In this spectral region, the membrane guided modes are suppressed and the light is strongly confined to the center of the waveguide. An emitter located close to center of the waveguide couples to two main sets of modes: the primary mode of the waveguide and the continuum of the radiation modes, see illustration in figure 3.6(b).

The solution to the Maxwell's equations under these conditions is:

$$\vec{E} = A_0^r \vec{E}_{\text{wg}} e^{ikx} + A_0^l \vec{E}_{\text{wg}}^{\dagger} e^{-ikx} + \sum_k c_k \vec{u}_{\text{rad}}, \tag{3.13}$$

where, $\vec{E}_{\text{wg}} e^{ikx}$ is the right propagating eigenvector of the primary waveguide mode. The Green's tensor for waveguide modes in this frequency range, neglecting the radiation modes, can be written as:

$$\begin{aligned}\overleftrightarrow{G}(r, r_0, \omega) = \frac{i\omega\epsilon_0}{2 \int\limits_{unitcell} Re[\vec{E}_{\text{wg}}^{\dagger} \times \vec{H}_{\text{wg}}] dr^3} \times \Big[&\Theta(x - x_0)\vec{E}_{\text{wg}}(r) \otimes \vec{E}_{\text{wg}}^{\dagger}(r_0) e^{ik(x-x_0)} \\ &+\Theta(x_0 - x)\vec{E}_{\text{wg}}^{\dagger}(r) \otimes \vec{E}_{\text{wg}}(r_0) e^{-ik(x-x_0)}\Big].\end{aligned} \tag{3.14}$$

The electric field generated from a point dipole based on the Green's tensor is:

$$\vec{E} = \frac{1}{\epsilon_0} \overleftrightarrow{G}(\omega, r, r_0) \cdot \vec{d}(\omega, r_0). \tag{3.15}$$

Using the three equations above the general form of the coefficients A_0^r and A_0^l for an arbitrarily oriented dipole moment can be derived as:

$$A_0^{l(r)} = \frac{i\omega \vec{E}_{\text{wg}}^{(\dagger)}(r_0) \cdot \vec{d}(r_0)}{2 \int\limits_{unitcell} 1/aRe[\vec{E}_{\text{wg}} \times \vec{H}_{\text{wg}}^{\dagger}].\vec{x} dr^3} \Theta((\pm)(x - x_0)). \tag{3.16}$$

Hereon, we use $A_0^{l(r)} = A_0^{l(r)}(x = x_0)$. It is straight forward to calculate the Γ_{wg} using the eigenvalue ω_k, the corresponding eigenvector $\vec{E}_k(\omega, r)$, equation 3.16, and [85, 97]:

$$\Gamma_{\text{wg}} = F_p^{\text{wg}} \gamma_0, \qquad , \qquad F_p^{\text{wg}} = \frac{6\pi^2 c^3 \epsilon_0 |\vec{E}_{\text{wg}} \cdot \vec{e}|^2}{\omega^2 \int\limits_{unitcell} nRe[1/a\vec{E}_{\text{wg}} \times \vec{H}_{\text{wg}}^{\dagger}] \cdot \vec{x} dr^3}, \tag{3.17}$$

where $\gamma_0 = \frac{n\omega^3 |\mu|^2}{3\pi\epsilon_0 \hbar c^3}$ is the decay rate of emitter in the membrane material, n is the refractive index of the membrane material and F_p^{wg} is the Purcell factor due to coupling to waveguide mode.

The parameter quantifying the fraction of radiation coupled to the primary waveguide mode is defined as:

$$\beta = \frac{\Gamma_{\text{wg}}}{\Gamma_{\text{total}}}. \tag{3.18}$$

For the case of an emitter at the spectral range of the primary PCW mode, $\beta = \frac{\Gamma_{\rm wg}}{\Gamma_{\rm wg}+\gamma_{\rm rad}}$.

Calculation of $\gamma_{\rm rad}$ in the same way is involved and requires discretization of the radiation continuum, which has its own complications [98], and is in general very time consuming. Our approach to this problem is to solve for the full Maxwell's equations for a dipole in the waveguide using frequency domain FEM as in previous section and then separate the contributions from the two set of the modes.

3.5.1 Simulation method

We extract $\gamma_{\rm rad}$ for two orthogonal in-plane dipole orientations, x and y that are located in the center of waveguide. The approach presented in this section is general and can be used for any type of in-plane dipoles. As in section 3.4.1 the particular orientation of the emitters and the symmetry of the structure in z direction allows to cut the simulation domain to half in the z-direction. Also as in the previous section we model a dipole by a small current element.

For a PCW, the main challenge in solving Maxwell's equations is to decouple the physical size of solution domain from the results. It is also highly desirable to limit the geometrical size of the simulation domain to the minimum possible. The general approach towards these goals has been to introduce an absorber in the boundaries of a finite simulation domain and adiabatically absorb the incoming wave [109, 112]. This approach is fully justified under two assumptions: the field impinging on the boundary should be a mode of the geometry that is invariant in the direction perpendicular to the boundary, and the solutions of the Maxwell's equations have to be propagating waves rather than evanescent fields in the direction normal to the boundary. In our case the simulation domain satisfies the requirements of PML in the three boundaries, $y = minimum$, $y = maximum$ and $z = maximum$, hence we can apply PML boundary conditions, see figure 3.7. Conversely, a PCW does not satisfy the first requirement above in the propagation direction (x), since its periodic nature in this direction. The generalization of the PML concept to photonic crystals has also proved to be inefficient in reducing the reflections from the boundaries of simulation domain [113].

In order to mimic an open system in the waveguide direction (x), we apply Dirichlet boundary conditions, $\vec{E}|_{x\pm} = C_{\pm}$ at the two ends of the waveguide ($x_{\pm}$). In general the value of $C_{\pm}$ is a sum of contributions from primary mode of the waveguide and the radiation continuum. We assume that the main contribution to $C_{\pm}$ is from the primary mode of the waveguide, neglecting the contributions from the radiation modes on these boundaries. We check the validity of this assumption by running a convergence test over the length of the simulation domain. Using equation 3.13, the value of the electric fields at the right and left boundaries ($x_{\pm}$) is:

$$E|_{x\pm} = -|A_0^{r(l)}|e^{-i\phi}\vec{E}_{\rm wg}^{(\dagger)}e^{\pm ikx_{\pm}}, \tag{3.19}$$

where ϕ is the phase of the projected electric field on the dipole at the position r_0, and r_0 is the position of the dipole in the unit cell. We call these boundary conditions "active boundary conditions". The amplitudes $A_0^{r(l)}$ can be calculated by plugging eigenvalues to the equation 3.16. In the case of linear dipoles, these amplitudes simplify to:

$$|A_0^r| = |A_0^l| = \sqrt{\frac{\hbar\omega\Gamma_{wg}}{2\int\limits_{unitcell} 1/aRe[\vec{E}^{\dagger}_{\mathrm{wg}} \times \vec{H}_{\mathrm{wg}}].\vec{x}dr^3}}$$
$$\phi = \mathrm{Arg}(-i\vec{E}_{\mathrm{wg}}(r_0).\vec{d}). \tag{3.20}$$

In general, the γ_{rad} may be extracted by subtracting Γ_{wg} from Γ_{total}, where Γ_{total} is the power integrated on the small box around the emitter and Γ_{wg} is extracted from equation 3.17. However, for the case of a PCW $\gamma_{\mathrm{rad}} \ll \Gamma_{\mathrm{wg}}$ and smallest reflections and numerical inaccuracies in Γ_{wg} spoil γ_{rad}. This can be avoided by calculating the γ_{rad} directly through integrating Poynting's vector over a box surrounding the current source and leaving out the integration over the boundaries normal to waveguide direction (x in figure 3.7), see green box in figure 3.7.

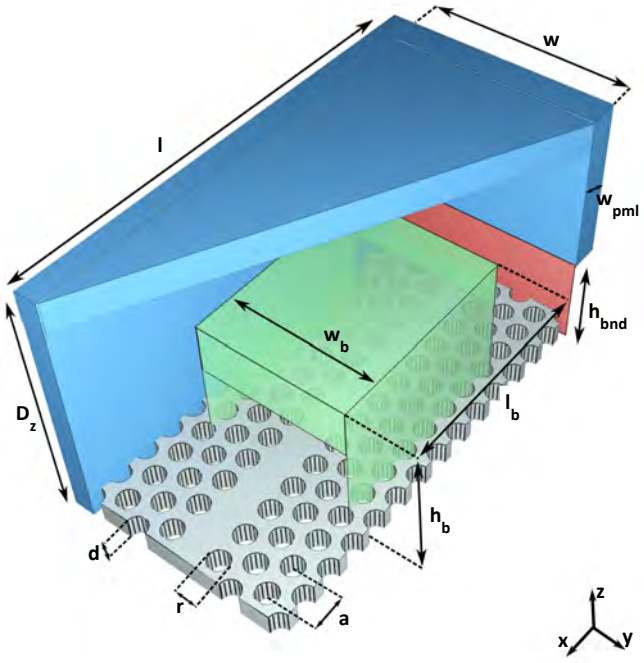

Figure 3.7: A cut through of the simulation domain. The blue box is the PML layer around the air domain. The green box is the integration surface that captures the radiation modes and the red plane is where the active boundary conditions are applied.

Figure 3.7 shows the geometry of the simulation domain. The PCW membrane has a length of $l = (2n+1)a$ and a width of $w = \sqrt{3}(2m+1)a$ and is surrounded by an air box of height D_z. The refractive index of the PCW membrane is chosen to be 3.5 corresponding to refractive index of the GaAs. The simulation domain is encapsulated by perfectly matched layers (PML) on all sides (blue box in 3.7). The width of the PML layer is w_{PML}. Active boundary conditions override the PMLs on the two ends of simulation domain normal to the waveguide direction (red plane in figure 3.7). The height of these planes are h_{bnd} and they cover the full waveguide in the y direction. The green box in figure 3.7 resembles the box that captures the radiation modes. l_b,w_b and h_b are the length, width and height of the radiation box. Note that the figure 3.7 is a sketch and the dimensions do not have the right ratio.

Table 3.2: Parameter list

Parameter	l	w	D_z	l_b	w_b	h_b	h_{bnd}	d_z
Value	$33a$	$9\sqrt{3}a$	$1.6\mu m$	$7.6\mu m$	$8\sqrt{3}a$	$0.6\mu m$	$0.5\mu m$	$80nm$

Table 3.2 gives parameter values used in the simulations in the rest of the article. To establish these numbers we have carried out numerous convergence tests. Some of the results of convergence tests will follow at the end of this section.

The simulation procedure is as follows: We first carry out an eigenvalue calculation to determine the frequency, N_g, eigenvector of the primary guided mode and the $F^p_{\rm wg}$ for the dipole position. Using equation 3.19 we determine the correct amplitudes for the respective boundaries of the waveguide. Next we run a finite element frequency simulation of the dipole in PCW with the active boundary conditions. The total power emitted from the waveguide is calculated by integrating Poynting's vector over a small box around the dipole. The $\gamma_{\rm rad}$ is extracted by integrating the Poynting's vector over the radiation box. In the next section the results of these simulations are presented.

3.5.2 Results

Application of the active boundary conditions suppresses the reflection from the boundaries of the simulation domain very effectively. Figure 3.8(a) and (b) illustrate the $|E|$ for a y-oriented dipole in the antinode of the Ey field for two different N_gs, 58 and 5 respectively, corresponding to slow and fast light propagation in PCW . The dipole position and orientation is marked by double sided arrow. The plots are zoom-ins around the position of the dipole. It is worth emphasizing that the value of $|E|$ is divergent at the point of the dipole, hence the color bars in figure 3.8 are saturated.

The field intensities on the right and left side of the simulation domain are uniform as expected from an infinite system. However the field profile is more intense around the dipole. These features are due to coupling of the dipole to evanescent modes of the PCW that are absent in the band diagram of figure 3.6. This can also be thought of dipole induce cavities in the waveguide. It is also important to mention that the shape of these localized modes totally depend on the position, orientation and frequency of the responsible dipole.

Due to the high suppression of the non-guided modes in a photonic crystal in addition to the enhancement of light emission to the primary waveguide mode, the β factor for the embedded emitters is known to be high [97, 98]. However an extensive study showing the position and frequency dependence of the $\gamma_{\rm rad}$ and hence the β-factor has been missing. Figure 3.9 provides a deeper insight to the issue. The three columns of this figure, from left to right, correspond to spatial maps of the Purcell factor due to coupling to primary waveguide mode $F_p^{\rm wg}$, Purcell factor due to coupling to radiation continuum ($F_p^{\rm rad} = \frac{\gamma^{\rm rad}}{\gamma_0}$), and the β-factor. Upper half of the figure shows the spatial maps of the listed parameters for x and y oriented dipoles with a frequency corresponding to $N_g = 5$ (fast light region). As clear from right hand column of figure 3.9(a) and (b), the waveguide mode in the fast

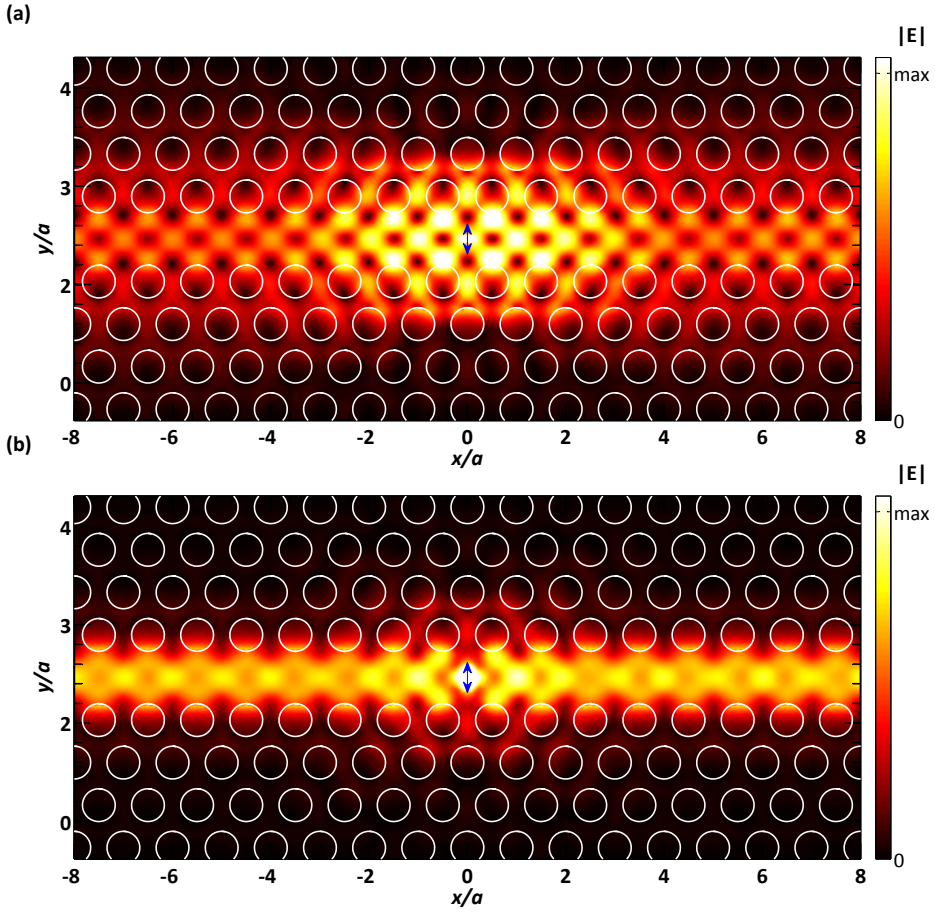

Figure 3.8: (a) Norm of the electric field from a y-dipole in the anti-node of the E_y for $N_g = 58$ and (b) $N_g = 5$. The blue arrow shows the dipole position and its orientation. The chevron like feature around the dipole is the dipole-induced cavity. The color scale is saturated due to divergence of electric field at the point of dipole.

light region is more confined to the center of the waveguide. The maximum value of the F_p^{wg} reaches 1.1 for y-oriented dipole and 0.5, hence the spatial distribution of the high β-factors are concentrated in the central part of the PCW.

The lower half presents the results for a dipole in the slow light regime ($N_g = 58$). The maximum of the F_p^{wg} for both x- and y oriented dipoles is around 9 due to slow light propagation. It is also interesting to compare the γ_{rad} for the two frequencies in figure 3.9 for parallel dipoles. The maximum value of F_p^{rad} for x-oriented dipole in slow light regime differs from the F_p^{rad} for x-oriented dipole in fast light regime by 0.013. This difference for the y-oriented dipoles is 0.007. In both cases it appears that going from the slow light to fast light regime the maximum of the coupling to the radiation modes increases by roughly 10%. However this not monotonically true for all positions of the dipole and actually there are significant differences depending on the position of the dipole. The values of F_p^{rad}, and their spatial dependence is similar to the case of a dipole in a perfect photonic crystal, as in section 3.4.2.

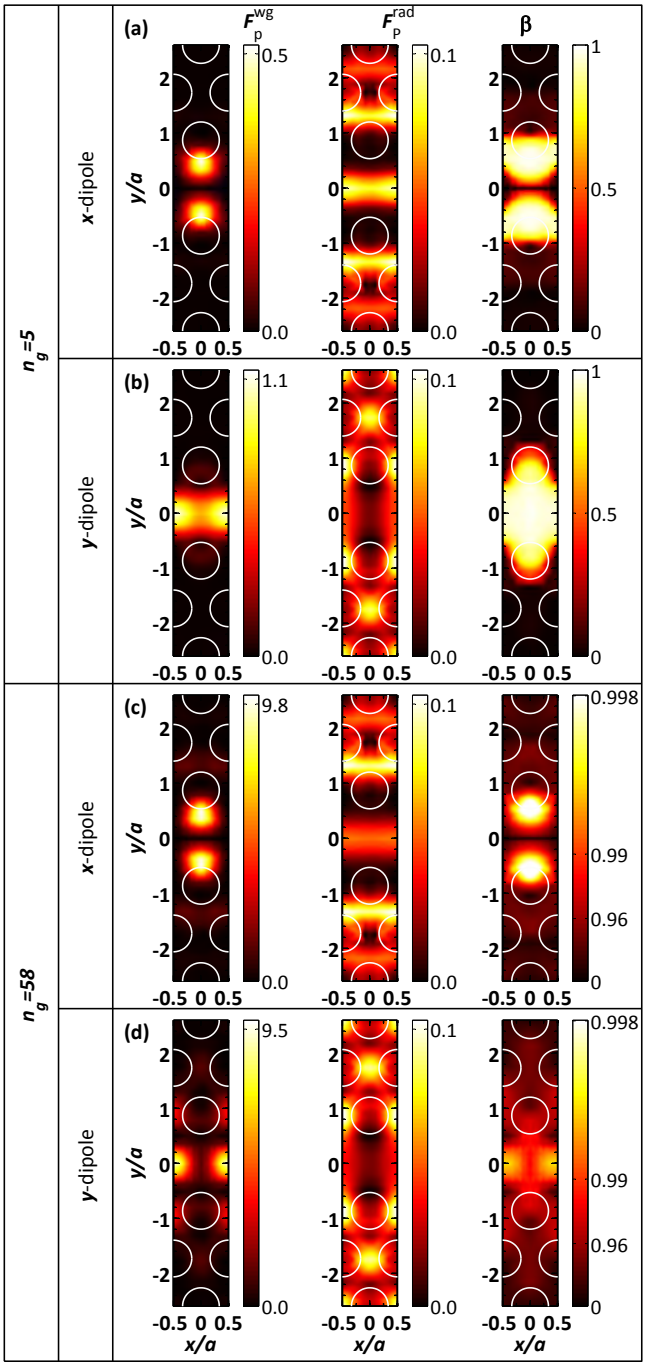

Figure 3.9: The spatial dependence of the waveguide Purcell factor (left column), the Purcell factor resulting from coupling to unguided radiation modes (center column), and the corresponding radiative β-factor, right column. (a) and (b) are at $N_g = 5$, and (c) and (d) are at $N_g = 58$. (a) and (c) plots are for x-oriented dipoles and (b) and (d) for y-oriented dipoles. Note the highly nonlinear scale on β factor maps in (c) and (d).

The spatial maps of the β-factor are also very intriguing. In the fast light regime, where the F_p^{wg} is relatively low, β-factors above 93% are readily visible. However, The high β-factor positions in figure 3.9(a) and (b) are limited to the center of the waveguide. Interestingly, for the dipoles in the slow light

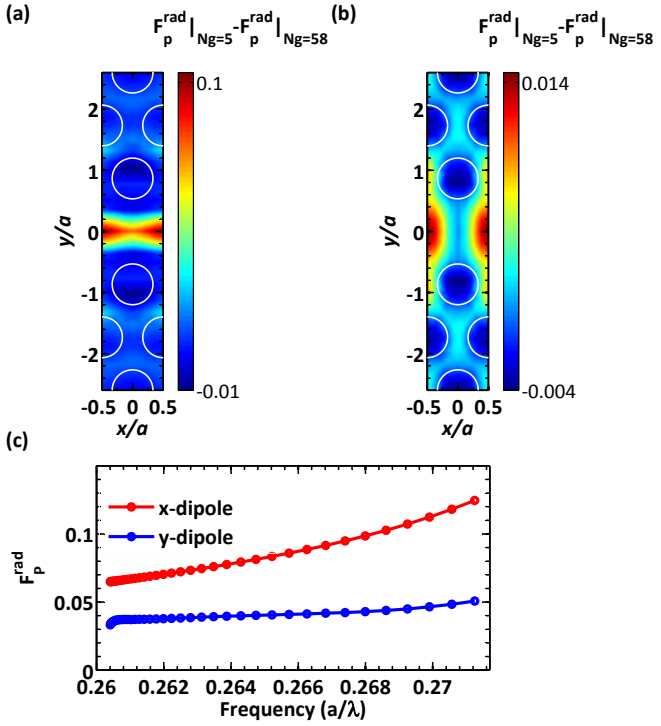

Figure 3.10: $F_p^{\text{rad}}|_{N_g=5} - F_p^{\text{rad}}|_{N_g=58}$ for x-oriented dipoles (a), and for y-oriented dipoles (b). The frequency dependence of the coupling to radiation continuum is found to be highly nontrivial and position dependent. (c) Frequency sweep of F_p^{rad} for x and y-oriented dipoles in the antinode of E_y.

region of the spectrum, the beta factor is higher than 0.99 for a very wide range of the dipole positions. Also note that the color bar in the 3.9c and d is highly nonlinear. Accurate Spatial positioning for many of the quantum emitters considered for scalable quantum information processing, e.g. quantum dots, nitrogen vacancy centers and etc., is challenging. The very wide spatial range of the β-factor for dipoles in the slow light region of the PCW can help relieve the requirement on spatial positioning of the emitters. These results are in well agreement with the previous work [96–98]. Furthermore, these results give a more extensive and detailed understanding of the potential of PCWs for efficient single emitter-photon interface, as well as single photon sources.

Figure 3.10 presents the frequency dependence of the coupling to radiation modes for the two dipole orientations. We plot the difference in F_p^{rad} between $N_g = 58$ and $N_g = 5$ for different dipole positions. Figure 3.10(a) shows $F_p^{\text{rad}}|_{N_g=5} - F_p^{\text{rad}}|_{N_g=58}$ for x-oriented dipoles. The value of F_p^{rad} appears to be higher by a factor of 2 at fast light region along the center of the waveguide. The main dispersive behavior for y dipoles is also observed in the center of the waveguide. However the increase in F_p^{rad} for x-oriented dipole is more than y-oriented dipole. It is also interesting to note that this dispersive behavior happens at the node of the E_x of the PCW mode (x component of the electric field). Figure 3.10(c) shows detailed frequency dependence of F_p^{rad} for x- and y-oriented dipoles at the antinode of E_y (the same spatial positions as 3.8).

The next section presents some of the convergence tests carried out to ensure the validity and accuracy of the results presented so far.

3.5.3 Convergence test results

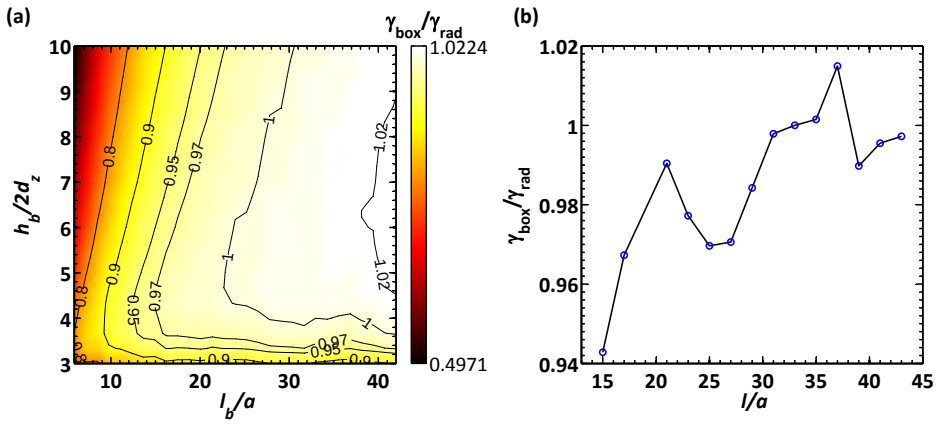

Figure 3.11: (a) Dependence of γ_{box} on the size of the integration box. For much of the parameter range γ_{box} is within 5% of the γ_{rad}. (b) Dependence of the γ_{box} on the actual size of the simulation domain. Both a and b are calculated for y-oriented dipole in the anti-node of the E_y field. The frequency of the dipole corresponds to $N_g = 58$.

Figure 3.11 presents some of the convergence tests carried out to ensure validity of the simulations and choice of the radiation box size. We choose $\gamma_{\text{box}}/\gamma_{\text{rad}}$ as the target parameter for convergence tests, where γ_{box} is the amount of radiation captured by radiation box of size h_b and l_b and γ_{rad} is the final value of γ_{rad}. It is clear from figure 3.11(a) that as long the box is long enough or the height of the box is short the value of γ_{box} is independent of the size of the radiation box, within 5%. A change in the length of the box from $15a$ to $40a$ results in around 5% change in the target parameter. Part (b) of figure 3.11 shows the dependence of the γ_{rad} on the size of actual simulation domain. The results in figure 3.11 are obtained using a y-oriented dipole at E_y antinode and $N_g = 58$.

We also studied the effect of the mesh size on the γ_{rad}. Some of the results can be found in appendix B. However, due to the meshing strategy, the results are rather robust to the meshing of the simulation domain. Details about the meshing of the simulation domain can be found in appendix B.

In the lower part of the figure 3.11(a), the value of $\gamma_{\text{box}}/\gamma_{\text{rad}}$ appears to decrease with decreasing height of the box in this range. However, one should also note that size of the active boundary condition is equal to $6d_z$. Hence, the integration over the radiation box, in this range captures contributions from the waveguide mode. Moreover, as discussed in appendix A, there is always a residual reflection at the boundaries of the waveguide and this residual reflection mostly is radiated to the air domain and captured by the lower radiation boxes.

We repeated the same tests for dipoles at a few more positions, orientations and frequencies and got similar results in terms of convergence. Hence, we conclude that the results in section 3.5.2 are accurate within 5%.

3.5.4 Comparison to experiments

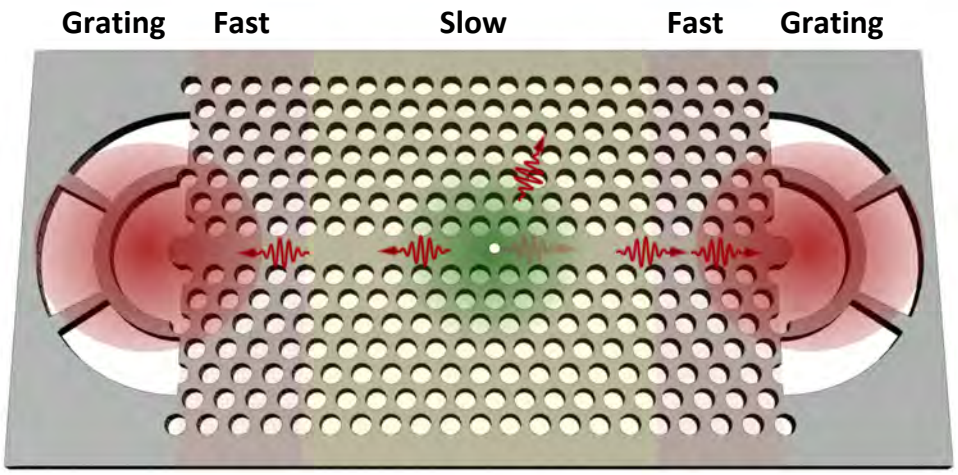

Figure 3.12: An sketch of the sample designed to extract the β-factor experimentally. The white circle in the center of the figure resembles a QD. The emitted photons mostly couple to the waveguide mode. The two sections on the right and left, indicated as fast, are the fast light regions. The two second order Bragg gratings couple the waveguide mode perpendicularly out of the sample. The green spot in the center of the waveguide is the aboveband excitation of the quantum dots.

Substantial experimental effort has been spent on demonstrating high coupling efficiency between quantum emitters and PCWs [22, 23, 99–102]. In a recent work [23], our group tried to estimate the maximum of coupling to F_p^{rad} and use this to establish a lower limit on the value of the β-factor. We studied InAs quantum dots that were embedded in the center of a GaAs membrane. Two sets of samples with different types of out-couplers were used. Figure 3.12 shows one the designs for this work. The design involves a slow light section in the center of waveguide, marked as slow in 3.12. This section is designed to have relatively high N_gs in the frequency around the peak of the QD inhomogeneous broadening. However, the waveguides with high N_g are relatively more lossy and it is harder to couple the light out of them [42, 43, 49]. Hence, we couple the high N_g section to the two modified waveguides where the lattice constant is stretched propagation direction. This region is marked as fast in 3.12. The fast light region spectrally overlaps with the slow light frequencies of the slow section [114]. For the main part of the experiments, the sample is terminated with second order Bragg gratings on the both ends 3.12 [115, 116], see the next section for more details about the out-couplers. The other design has the same structure as this one, however one of the out-couplers is replaced by an inverse taper to allow photon collection from the side of the waveguide [117]. The insets in 3.13 (a) and (b) show SEM images of the different out-couplers used. See chapter 4 or reference [23] for more details on the working principle of a similar structure. The two out-coupler act well to suppress the reflection back into the waveguide.

In order to establish an upper bound on the coupling of QDs to radiation modes, we collected the light from the two out-couplers and looked for the dots that showed inhibited decay rates. In order to suppress the coupling to the waveguide further, samples were terminated by photonic crystals in one end, hence creating Fabry-Pérot resonances. The slowest inhibited dot found on these waveguides

was chosen as a reference dot. This dot was spectrally in between two Fabry-Pérot resonances. The decay rate of this dot was assumed to be totally due to coupling to radiation modes, Γ_{ref}, neglecting the waveguide contribution. Extensive details regarding the method can be found in [23]. This value is a upper bound on γ_{rad}, and as an upper bound, it agrees well with the simulation results from the previous section. Also, this value is higher than the value of coupling to the radiation modes from the dots sitting in the stretched lattice waveguide in where the decay to waveguide is enhanced [23].

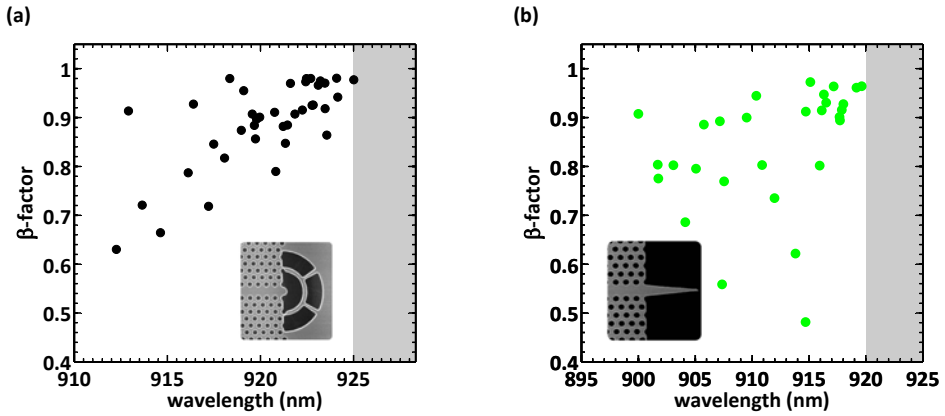

Figure 3.13: An statistical study of the coupling to the waveguide mode from single quantum dots. (a) The statistics collected from the sample with Bragg gratings in both ends. (b) Statistic of decay rate from a sample where one end is terminated with a Bragg grating and the other end is terminated with an inverse taper. The insets show the SEM image of the respective out-couplers. The gray areas in both sections of the figure are the band gaps of the corresponding waveguide.

Two set of samples with out-couplers in both ends were used to collect statistics of quantum dot decay rates. The β-factor was extracted from the experimental data as $\beta = \frac{\Gamma_{dot} - \Gamma ref}{\Gamma_{dot}}$. The quantum dots were excited using a pulsed laser at 800 nm. A total of 71 dots were studied in the two waveguides. Most of the dots studied had F_ps in the range of 2-3. Figure 3.5.4 shows the β-factor of the dots versus their emission wavelength. Figure 3.5.4 (a) is the data collected from a sample with gratings on both ends (similar to sketch in 3.12). The data in the right panel of 3.5.4 are extracted from the waveguides with tapers in the end. Both samples show relatively high β-factors. For most of the dots the β-factor is higher than 85%. Also, there is a clear correlation between the wavelength of the emission and the β-factor. As expected, due to the slow light effect, the decay rate of the dots is enhanced close to the band-edge of the waveguide. The β-factor reported in this work constitutes a lower bound on the actual beta factors mainly because the reference dot is still coupled to the waveguide. This means that the decay rate of the dot has a component that comes from the waveguide mode contribution.

Further measurement under P-shell excitation on the same waveguides revealed a quantum dot with decay rate of $6.28\,\text{ns}^{-1}$. The β-factor for this dot is extracted to be 98.8% which is the highest measured in this work. The single quantum dot nature of the emission line was verified with Hanbury-Brown-Twiss measurement. These measurements combined with the theoretical results in section 3.9 further proves the potential of PCWs for deterministic light matter interaction, and opens the path for realization of 1D atoms, on-chip photon transistors, CNOT gates, and deterministic single photon sources.

3.6 Out-coupling of light from planar nanostructures

The efficient out-coupling of photons from planar nanostructures like PCWs is the next step towards utilizing these structures for QED applications. In this section we numerically study the efficiency of different out-couplers in-coupling the light out of waveguides. To do so, we calculate the electric and magnetic fields close to the nanostructure and use a far-field transformation to calculate the far-field pattern of the nanostructure. The coupling to the objective is obtained as the ratio of the power in the N.A. of the objective to the total power emitted from the nanostructure.[1]

A second order Bragg grating has the advantage of coupling the light orthogonally out of the chip. This is particularly advantageous for the samples that are sitting in a cryostat. Periodic gratings alter the propagation of light by adding momentum to its original momentum. A grating with periodicity l adds a momentum equal to $m2\pi/l$ to impinging light. The operation principle of the second order Bragg grating is based on canceling out the in-plane momentum of the light k, by a periodic grating which has the periodicity of the wavelength [115]. The inset in figure 3.13 shows a SEM image of a second order grating. This grating consists of a periodic array of air layers and GaAs layers, where width of the air layer and material layer are equal to $\lambda_0/2$ and $\lambda_0/2n$ respectively. A field propagating in the plane of the grating with momentum k receives a momentum equal to $-k$ and couples out of the grating. We have experimentally observed that two periods of the grating is enough to efficiently couple the light out of the waveguide.

The inverse taper out-couplers work based on adiabatic coupling of the light out of waveguide [117]. The inset in figure 3.5.4 shows a SEM image of a inverse taper grating. The optimal length of this grating is around $6a$ [117]. In a grating type structure 50% of the light is lost due to the symmetry of structure. On the contrary, all the light coming out of a taper propagates in the same direction, which means that, in principles, all of it can be collected.

Considerable effort has been spent of optimizing the collection efficiency of light emitted from the photonic nanostructures, mainly the photonic crystal cavities [118–121]. These studies normally tie with the Q-factor optimization of the cavities (to certain degree Q-factor and collection efficiency are competing parameters) [54, 122–124]. The ideal case would be to have all the emitted photons go out within the N.A. of the collection objective. Also it is highly desirable to obtain a Gaussian shape for the far-field pattern, so that the coupling to single mode fiber is more efficient.

According to Huygens principle, knowledge of electric and magnetic field on a surface Ω enclosing all the sources is enough to extract the field distribution at any point outside the surface, see figure 3.14 for an sketch. Based on this principle, the electric field at a point can be calculated using the Stratton-Chu integral equation [125, 126].

$$\vec{E}_{far} = \frac{ik}{4\pi}\vec{r}_0 \times \oint_{\Omega} [\vec{n} \times \vec{E} - \eta r_0 \times (\vec{n} \times \vec{H})] e^{ik\vec{r}\cdot\vec{r}_0} dS, \tag{3.21}$$

where Ω is the surface enclosing the sources, n is the normal to integration surface, E and H are the

[1] I thankfully acknowledge significant contributions from S. Mahmoodian to the results of this section.

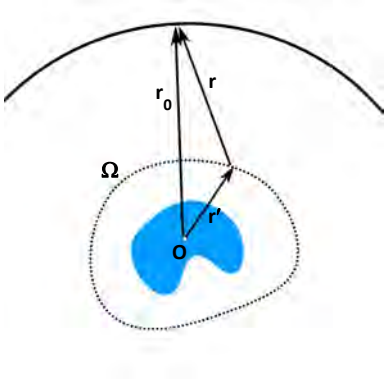

Figure 3.14: A sketch showing the far-field calculation principles. O is the center of the coordinate system. Knowledge of the electric and magnetic fields on the surface Ω is enough to calculate the field intensities anywhere outside this surface.

electric and magnetic fields on the surface of integration, and η is the impedance of the medium (refer to figure 3.14 for r_0 and r). The built-in feature of COMSOL, numerically computes the integral in equation 3.21 to calculate the electric field at far distances from the integration surface. Alternatively, flowing the procedure in [122] the far-field can be related to the near-field , using the fourier transform, with assumption that Ω is a infinite plane. We have verified that the two methods produce the same results.

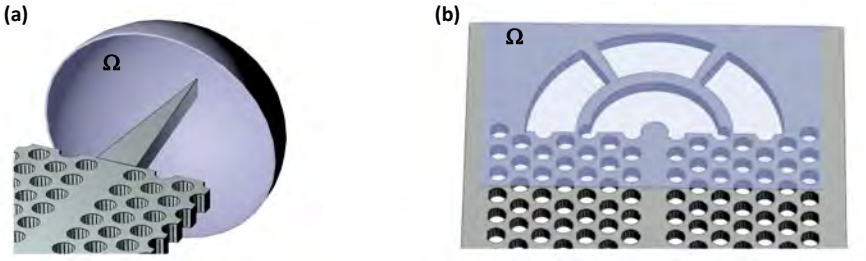

Figure 3.15: The far-field domains for (a) taper out-couplers and (b) for grating out-couplers.

Figure 3.15 shows the integration domains used to calculate the integral in equation 3.21. For the taper out-couplers, we choose to use a hemisphere surface as the integration domain, since it better captures the field pattern around the taper, while a flat surface works better for the grating structure, since it is a planar geometry. The diameter of the hemisphere in 3.15(a) is chosen to be $6a$. The set up of the rest of simulation domain is similar to 3.7, except for the fact that the active boundary conditions are not necessary for this type of calculations. We use a dipole source in the waveguide to excite the out-couplers. We sweep the frequency of the dipole source to obtain the frequency dependence of the collection efficiency from the out-couplers.

Figure 3.16(a) shows the collection efficiency of inverse taper out-coupler. The rectangles in figure 3.16(a) mark the collection efficiency with NA of 0.82 and circles correspond to collection by $NA = 0.65$. Collection efficiencies of order of 0.7 are readily achievable with the taper design. The collection efficiency appears to be broadband and almost constant over a range of 40 nm. Figure 3.16(b) shows the far-field pattern of $|E|^2$ for the taper at the wavelength marked by red circle in part (a). The field

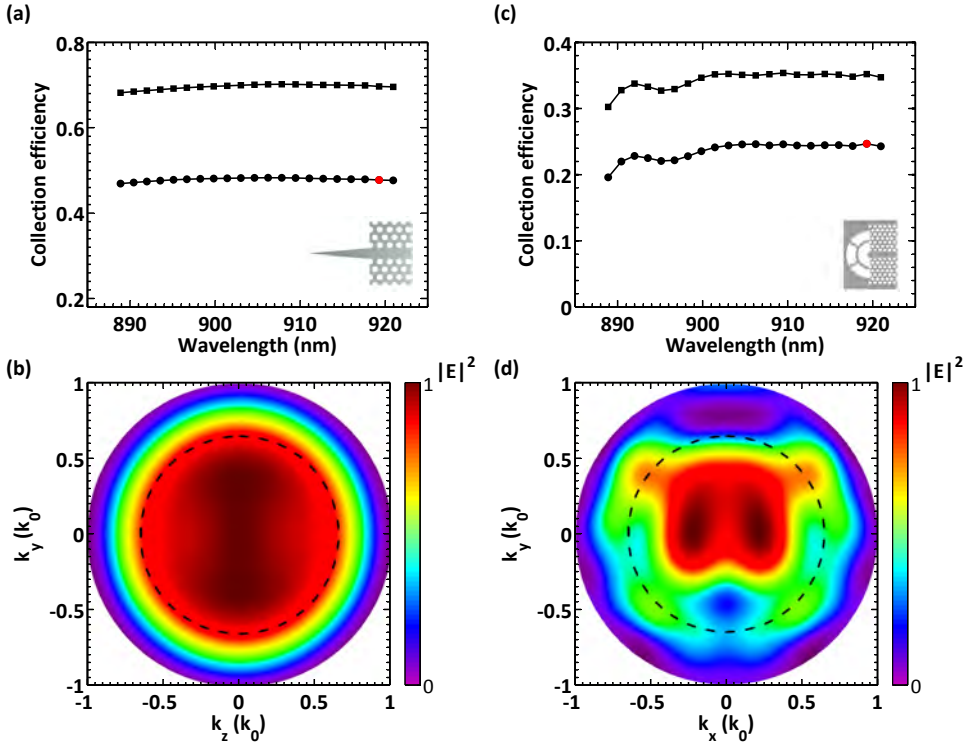

Figure 3.16: (a) The collection efficiency to the first lens from the tapered out-couplers versus wavelength. Circles mark the collection efficiency by an objective with NA=0.65 and rectangles mark NA=0.82 (b) the far-field pattern of the taper out-coupler for the frequency marked as red color in part (a). The dashed circle is the NA=0.65. (c) and (d) the same as (a) and (b) but for second order Bragg gratings. Note that the maximum efficiency achievable for a grating out-coupler is limited to 50%.

profile appears to have a shape close to a Gaussian in z direction. However, in the y direction the field profile appears to deviate from a Gaussian and has two side lobes.

Figure 3.16(c) shows the collection efficiency of a second order Bragg grating out-coupler. The maximum achievable collection efficiency is around 35% for NA of 0.82. This value appears to be broadband within 40 nm. Figure 3.16(d) shows the far-field pattern of the electric field. The field pattern significantly deviated from an ideal Gaussian, which means that the coupling to the fiber will be worse than the inverse taper design.

The designs above can be further improved by putting a ridge waveguide between the out-coupler and the photonic crystal section, which was studied later in the group. Also, for the Bragg grating design, including a distributed Bragg reflector underneath the sample will help to couple back the down going part of the field and hence improve the collection efficiency. Similarly the distance between the membrane and the substrate can be engineered to achieve better collection efficiencies as done for cavities in the past [118, 120].

3.7 Conclusions

We have used frequency domain finite element method to solve Maxwell's equations and extract local density of states for emitters in different photonic crystal nanostructures. Previous work had already shown significant inhibition of the decay rate of emitter due to the effect of the photonic band gap. By sweeping the position of the emitter, we created very detailed maps, showing spatial and orientation dependence of decay rate of emitters in the band gap of a photonic-crystal membrane. Our results indicate that local density of states in a PhC membrane is highly position dependent, and is inhibited by factors of 10 to 180. These value tend to be broadband, for frequencies in the band gap of PhC.

We studied the position and frequency dependence of LDOS in a PCW. We separated the contributions to the LDOS from the leaky mode continuum and the waveguide mode. This allowed us to calculate the coupling efficiency of emitters to a PCW. The main challenge in these calculations was to effectively terminate the waveguide without significant reflections. We overcame this by using active boundary conditions on two ends of the waveguide. We further used a second box that captures the radiation continuum and not the waveguide mode to calculated the power emitted to the leaky modes and to further increase the accuracy of our results. The results show that the coupling to the radiation modes is not significantly modified from the case of a PhC. The spatial maps confirmed a high suppression of coupling to radiation modes. We also showed that at high N_gs the β-factor is in general higher than 98% and that the value of β in slow light regime is relatively insensitive to the position of the emitter. The results also showed that even in low N_gs, very high β-factors are achievable in the center of PCW. Backed by these results, in a collaboration inside the group, we could experimentally demonstrate very efficient coupling between GaAs QDs and PCWs. β-factors as high as 98% were experimentally observed.

The calculation of the electric field profiles for PhCs and PCWs further revealed possibility of light localization due to the presence of a dipole, dipole induced cavities. For the case of PhC, these cavities have Q-factors in the range of $F_p\gamma_0$. For a GaAs QD in the PhC membrane this value would be on the order of 10^7 . This field localization around the dipole might be useful in creating strong dipole-diploe interaction at short ranges.

Finally, we studied different out-couplers and numerically extracted their far-field patterns and collection efficiencies. Our results indicate that collection efficiencies of up to 80% are possible. Further work in our group has shown that the collection efficiency can be improved by using a mode adapter between the out-coupler and the PCW. These out-couplers play an important role in efficiently extracting the light from the chip.

Chapter 4

Resonant excitation of quantum dots in photonic-crystal waveguides

As discussed in the previous chapter, a photonic-crystal waveguide provides a nearly deterministic interface to the embedded quantum dots. This allows the embedded quantum dots to modulate the transmission spectrum of the waveguide. In this chapter, we present the experimental details of resonantly exciting a quantum dot in a photonic-crystal waveguide (PCW). We discuss the geometry of the sample that allows us to probe the transmission of the PCW inside a cryostat, while maintaining the efficient coupling of the embedded emitters to the propagating mode of the waveguide. The s-shell transition of InAs quantum dots is dark to the resonant laser due to the background doping and charge traps around the QD. It is known that a weak aboveband laser incident on the sample can activate this transition. We reassess how the weak aboveband laser can reactivate the QD transitions and make them visible to the resonant laser. Most of the literature in solid state quantum optics community deal with QDs embedded in bulk GaAs. We adapt these techniques to PCWs. In our preliminary measurements, we observe the QD transitions as extra noise in the transmission spectrum of the waveguide. Also we observe a transmission dip of 3% in our preliminary measurements. In our main measurement, we observe a contrast of up to 30% in the transmission spectrum of the waveguide. Auto correlation measurements on the transmitted light confirm the single quantum dot origin of the observed transmission dip. The sample degrades over time, nevertheless we are able to obtain resonant excitation in our sample even after long periods by changing the wavelength of the aboveband laser. The results pave the way for resonant excitation of QDs in the Purcell regime inside a PCW , which enables many exciting experiments such as the observation of the giant optical nonlinearity, demonstration of single photon switching, and photon sorting. The next section provides a review of the past experimental effort to excite quantum dots resonantly in the bulk GaAs material as well as in different nanostructures.

4.1 Introduction and literature review

Scalable quantum computing in any platform, requires coherent and efficient interaction between the qubits. Photons are considered as the means to mediate the coherent interaction in proposals based on atoms [15], molecules, superconductors [127], and quantum dots [128]. Most of the proposals involve single photons on resonance with the internal energy levels of the qubits to mediate this interaction. However, resonant interaction between photons and quantum dots is not straight forward and was not realized until recently [129–133].

The first attempts to observe photoluminescence from single quantum dots were limited to above-band excitation schemes [134–137]. Later, different strategies such as differential reflection and transmission as well as higher shell excitation were employed to study QDs [138–143]; see also [144] and references there in. However, resonance fluorescence from single QDs remained an open challenge until recently. The main challenges towards observation of resonance fluorescence was to separate the fluorescence from the excitation laser. Muller *et al.* used a planar geometry and excited a quantum dot from the side of the sample while collecting emission from the top [129]. This allowed to separate the excitation laser from the emission of the QD and to observe anti-bunching in the collected photons. Around the same time, several other groups managed to resonantly excite the quantum dots using different methods [132, 133]. Shortly after, spin resolved resonance fluorescence, coherent spin initialization and readout was demonstrated [145, 146]. Two experiments demonstrated that a single QD can coherently modulate the intensity of a laser beam [147, 148]. Very recently, two groups demonstrated generation of ultra coherent photons from single quantum dots under weak coherent excitation [149, 150]. A major advantage of exciting the QDs resonantly is to eliminate the dephasing and recently highly indistinguishable single photons from single quantum dots were observed under resonant excitation [151]. However, s-shell transitions of a quantum dot are inhomogeneously broadened because of spin and charge fluctuations in the environment of the QD [152–157] and fourier transform limited transitions are observed only in short time scale (10 µs) [152].

Majority of the QDs are grown with Stranski-Krastanov method, also referred to as self-assembly method. Since the particular growth method several traps also form around the QDs. Charge trapping and escape happens frequently in these traps [152]. As a result, the charge configuration of the QD environment changes over time scales of milliseconds. These charges affect the transition frequency of the QD through coulomb interaction. However, the resulting energy shifts are on the order of the linewidth of the QD transition, and hence the result is broadening of the QD transition (spectral diffusion). The spin of the nucleus of the atoms that form the QD can also give rise to a similar effect through the Overhauser effect [152]. Also, a single charge, electron or hole, trapped inside the QD can shift the QD transition by several milli-electron volts. Such a charge can have lifetimes of microseconds to milliseconds. This type of charging effects result in blinking of the QD transition.

In order to achieve resonance fluorescence from QDs with high yield, two approaches have been used. The first approach is to place the QD layer inside a p-i-n diode and apply a forward bias. This allows to deterministically define the charge state of the QD and reduce the charge fluctuations in the environment [144, 145, 147, 149, 152, 158]. Another approach is to use a weak aboveband laser to

optically activate a given transition in the QDs [150, 156, 159–162].

Reference [161] gives a detailed description of the effect of a faint aboveband laser on the resonance fluorescence from a QD. According to them, the background doping in the environment of the QD gives rise to residual carriers in the QD an the traps around it. This residual charge blocks the emission of the ground state of the QD. According to the article, fluorescence from 90% of the dots is quenched when probed purely resonantly. Adding a weak aboveband laser creates a certain electrostatic equilibrium in the environment of the dot and revives the fluorescence from the ground state. The typical power necessary for the photo-neutralization of the QD is a few tens of pW and does not result in noticeable emission from the QD. Interestingly, the weak aboveband laser shifts the transition energy of the QD state by several GHz. The time scales for the photo-neutralization of the QDs is around 10 µs, and the QD remains active for hundreds of micro seconds after the aboveband laser is turned off.

Efficient collection of the emission from QDs is another challenge for utilizing them in quantum information processing. All of the experiments discussed above are done with quantum dots in homogenous environment or with very wide waveguide-like structures where collection efficiencies are very poor [163, 164]. Utilizing nanostructures around the quantum dots allows to efficiently collect the emission and deterministically interface the QDs with single photons [22–24, 165], see also [30] and references there in. However, resonant excitation of quantum dots in nanostructures has its own complications. In general, the dimensions of a nanostructures are on the order of wavelength of the photon. This means that the distance between the QD and the material interfaces are in around 1/4 of wavelength of the emission. This may increase dephasing, blinking, and other effects due to the short distance between the QD and the surfaces [93].

The first resonant experiments were done using quantum dots strongly coupled to nanophotonic cavities [166, 167]. Englund *et al.* measured reflection from a QD strongly coupled to an L3 photonic crystal cavity. They used a heating pad to scan the QD-cavity system through a CW laser [166, 168]. Srinavasan *et al.* achieved resonant excitation of polaritons in a strongly coupled microdisk-QD system [167]. Later, several other groups also reported resonant excitation of a strongly coupled QD-cavities systems [169–171]. The main advantage of a strongly coupled QD-cavity system is the broadened cavity polaritons. This helps fight spectral diffusion and dephasing of the quantum dot transitions.

Significant effort has also been spent on exciting the QDs in nanostructures in the Purcell regime. Faraon *et al.* managed to excite a QD weakly coupled to a PhC cavity and observed a transmission contrast of 30% [116]. However, they only reported a single measurement without further analysis. Rakher *et al.* demonstrated up to 50% contrast in reflection of a quantum dot weakly coupled to a micropillar cavity [172]. They embedded the QD layer in a p-i-n which allowed them to control the electric field at the QD layer and deterministically charge the QD. Arnold *et al.* recently reported resonant excitation of trions in micropillar cavities and observed phase shifts up to 6% [173]. In reference [174], the authors managed to observe the transitions of a charged quantum dot coupled to a L3 PhC cavity. They used a p-i-n structure to apply an electric field over the QD layer. Unfortunately, the article does not give any numbers for the linewidth of the transitions; however, the current running

through the device is mentioned to be up to 20 mA and even shifts the cavity resonance by a few GHz. Pinotsi *et al.* also tried to use a p-i-n diode to stabilize the transitions of a QD in a L3 PhC cavity. They managed to observe photoluminescence, however the linewidth of the detected photons was far from being fourier transform limited [175]. Two groups observed resonance fluorescence from QDs in membrane photonic waveguides [176, 177]. In both cases, the approach was to excite the QD with a laser beam that was orthogonal to the waveguide and suppress the direct scattering of the resonant laser to the waveguide by its polarization [176, 177]. Another interesting approach is to create Fabry-Perot cavities between a distributed Bragg mirror underneath the QD layer and a mirror formed on the tip of a fiber [178]. This a1llows to efficiently interface the QD to the cavity through Purcell enhancement and directly couple the cavity to the fiber.

Electrical gating of quantum dots, in the case of QDs in bulk medium and also in the case of micropillar cavities, work very well to suppress the charge fluctuations and deterministically prepare the ground state of the QD. There are a few reports of electrical tuning of the QDs in thin membranes [174, 175, 179], however these implementations suffer from different problems and all have failed to observe linewidth limited transitions. As discussed earlier, there are several reports of using a weak aboveband lasers to stabilize the QD transitions and reduce the spectral diffusion [151, 161]. In this thesis, we also use a weak laser, either at 800 nm or at 850 nm to activate the ground state of our emitter.

Our aim is to excite the QD coupled to a PCW resonantly. Next section discusses the experimental considerations including the sample structure and the experimental setup.

4.2 Experimental considerations

As discussed in the previous chapter, a QD in A PCW is efficiently coupled to the waveguide mode. As a result, the photons launched to the waveguide will interact strongly with the QD. When frequency of the laser is on resonance with the transition line of the QD, the photons get reflected. This is a result of interference between the photons scattered from the QD and the photons transmitted [180], see next chapter for more theoretical details. This effect can be seen in the transmission spectrum of the waveguide when scanning the laser over the linewidth of the QD. However, the reconstruction of the transmission spectrum of the waveguide is complicated by several effects, i.e. charge diffusion and blinking of the QD line, as well as the residual Fabry-Perot resonances caused by imperfect optical components.

As discussed before, a weak repump laser can cure the blinking and the spectral diffusion to a certain degree. We also modulate this laser to turn the QD transition ON and OFF during the scans. This way we get a reference signal to normalize the transmission spectrum of the waveguide and eliminate the effects from the imperfect optical components. Next section discusses the structure of the sample.

4.2.1 Sample structure

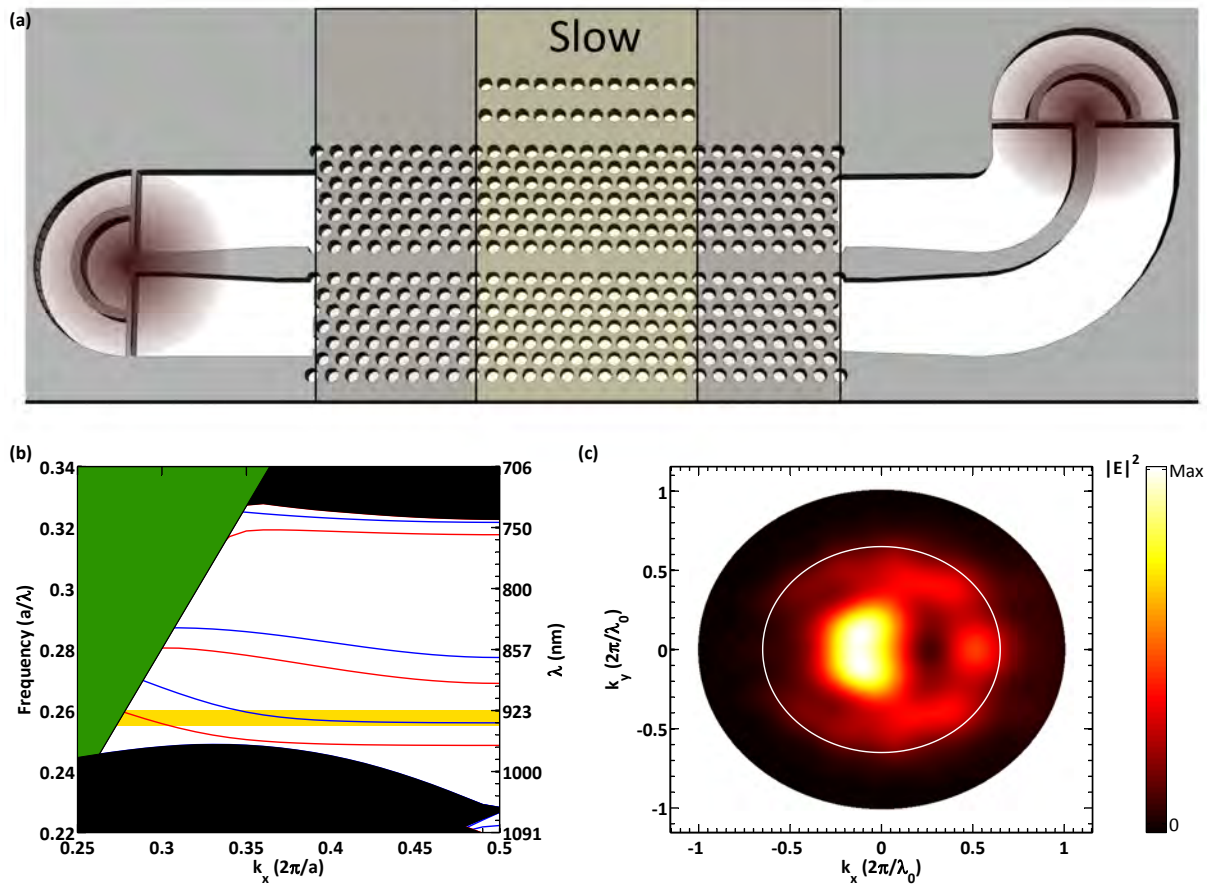

Figure 4.1: . (a) A sketch of the sample. The slow-light sections are marked as slow. (b) Bandstructure of the sample. The blue lines are the bands belonging to the slow-light section and the red ones belong to fast-light section. The green shaded region marks the continuum of the radiation modes and black regions mark the modes guided in the photonic-crystal membrane. The slow-light waveguide and the fast-light waveguides spectrally overlap in the yellow shaded region and hence the light transmission in the yellow shaded region is enhanced. (c) The far-field pattern of the out-coupling gratings. The white circle is collection to N.A. 0.65

In this section, we outline the design parameters of the sample used for the main part of the experiments. The designed sample is shown schematically in figure 4.1(a). It is composed of a slow-light PCW, which is coupled to fast-light PCWs on both sides, which are coupled to a ridge waveguide and then an output grating. The membrane has a thickness of 160 nm and is entirely composed of GaAs which has a refractive index of $n = 3.464$ at 10 Kelvin. The membrane has a single layer of InAs quantum dots in the center. The slow-light photonic waveguide is patterned with a triangular array of holes with radius r =72 nm and lattice period a = 235 nm. A line defect of missing holes in the array forms the waveguide. The fast-light PCW has the same parameters as the slow PCW, but the lattice period is stretched to $1.07a$ along the propagation direction. As shown in figure 4.1(b), this ensures that, at wavelengths where the group velocity of the slow-light region is low, the fast-light

waveguide supports a mode with a larger group velocity. The slow-light section is 8.00 µm long, while the fast-light section is 15.6 µm long. A short slow-light section is used to minimize disorder induced backscattering and out-of-plane scattering, as it has previously been shown that both increase with decreasing group velocity [42] . Even though the transition from the slow-light waveguide to the fast-light waveguide is abrupt, it has been shown that evanescent modes mediate efficient coupling between two such waveguides [114], and thus a high transmittance is expected. The fast PCWs are coupled to ridge waveguides with a width of $\sqrt{3}a$ corresponding to the center-to-center distance of the rows of holes adjacent to the waveguide. The ridge waveguides are then tapered down to a width of 266 nm over a length of $5 \times 1.07a$. The waveguide on the right in figure 4.1(a) arcs through 90 degrees before it reaches the grating. This arc has a large radius of curvature of $5a$ which reduces bend losses.

The out-coupling gratings are based on the design presented in Ref. [116]. The gratings act as a second order Bragg reflector that couples light in the ridge waveguide mode to out-of-plane modes. The grating is composed of alternating layers of concentric circles separated by $\lambda/2n$, where n is the refractive index of air/GaAs, and $\lambda = 922$ nm is the design wavelength. We have improved on the design in Ref. [116] by coupling into each grating from a ridge waveguide of width λ/n which enhances the magnitude of the field that falls in to the numerical aperture of our collection lens. This far-field radiation pattern is illustrated in figure 4.1(c). The white circle indicates the numerical aperture of our collection lens which is NA = 0.65. We have computed that $\sim 90\%$ of the light coupled upwards is collected by the first lens. Two gratings are arranged to have orthogonal polarization in the far-field to further avoid excitation laser from coupling to collection optics.

4.2.2 Experimental setup

Figure 4.2 shows sketch of the experimental setup. The sample is sitting inside a helium flow cryostat. The pressure inside the sample chamber is normally down to 1×10^{-6} mBar. The sample holder is in contact with a copper cold-finger. A temperature sensor and a heater are in thermal contact with the cold finger. The cold finger is cooled down through direct contact with helium flow that comes from a helium dewar. A temperature controller keeps the temperature constant (typically around 6.5 K) by controlling the helium flow and the heater. The cryostat is mounted on a pair of motorized positioning stages with the resolution of 100 nm. This allows us to move the sample relative to the collection and excitation spot, as shown in figure 4.2(a).

A modified microscope is used to optically access the sample. Both the resonant and the repump laser are focused on the sample through an Olympus objective with $N.A. = 0.65$. The excitation and collection are separated using a 50% beamsplitter inside the microscope, see figure 4.2(a). The collected light is sent through a halfwave plate and a polarizing beamsplitter to filter its polarization, as shown in 4.2(b). A long-pass optical filter is used in the collection to cut out the direct reflection of the repump laser and also any emission below the cutoff wavelength. At the end, the collected light is coupled to a single mode fiber. The single mode fiber acts as an spatial filter that limits the collection spot to 1.4 µm^2. The collected light is then sent to a pair of fiber-coupled APDs for photon counting and auto correlation type measurements.

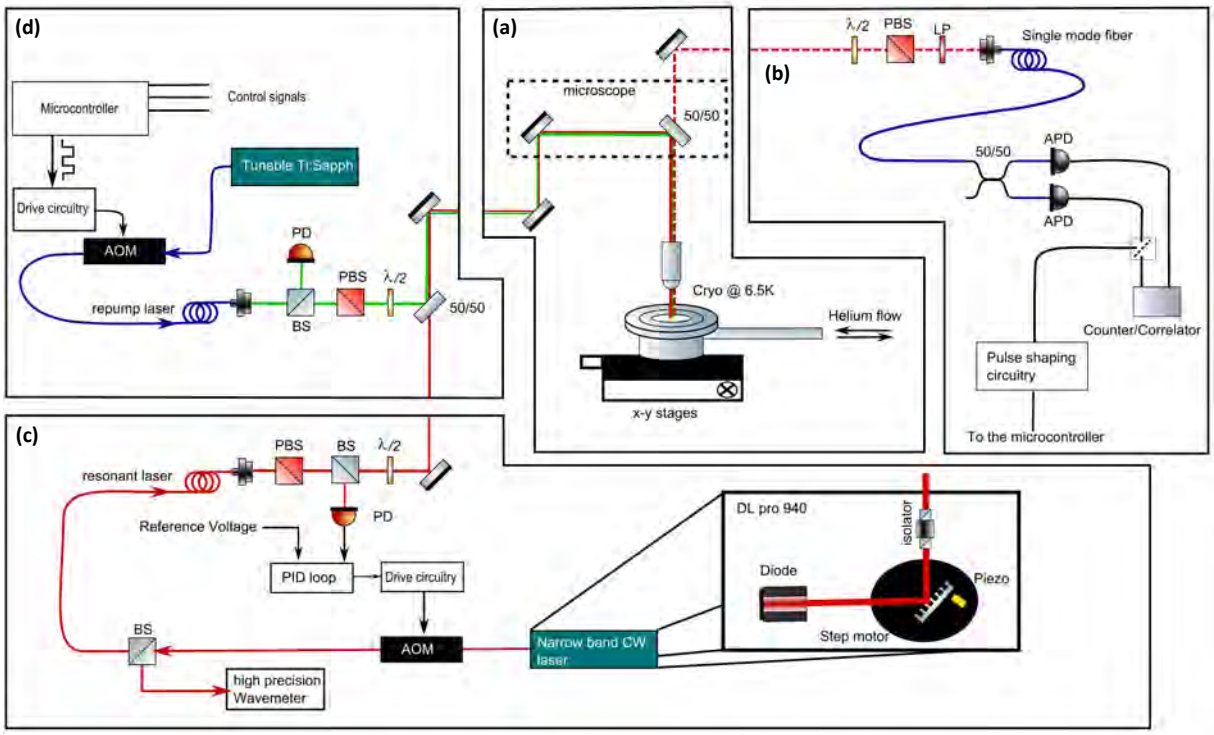

Figure 4.2: . Sketch of the experimental setup. (a) The sample is sitting in a helium flow cryostat. The cryostat is mounted on a pair of stages with 100 nm spatial resolution. A modified optical microscope is used to optically access the sample. The collection and excitation lasers are separated using a 50% beamsplitter. (b) The collected light is sent through a halfwave plate and polarizing beam splitter and coupled to a single mode fiber. The collected light is later detected using two fiber-coupled APDs. (c) A narrow-band CW laser is scanned through the resonance of the QD. The sketch in the right hand side shows the internal structure of the laser. The intensity of the laser is stabilized using an AOM and a PID loop. The laser light is sampled and sent to a high precision wavemeter to monitor the wave length and assure single mode operation. (d) The repump laser is regulated with an AOM. The experiment and the data acquisition is controlled through microcontroller to a high degree.

A narrow band CW laser, DLpro 940 from Toptica, is used to excite the QD lines resonantly, referred to as resonant laser. DLpro 940 is an external cavity tunable laser in Littrow configuration, see 4.2(c). The laser operates from 904 nm to 985 nm. The diode is composed of a broad-band internal cavity, and a narrow-band external cavity. The external cavity is formed between the diode and a grating. The design uses two mechanisms to tune the laser wavelength. For long range tuning, the angle of grating is changed. For short range tuning (up to 50 GHz), the grating angle is changed using a piezo-actuator in fine steps. The same signal is also fed-forward to change the diode current, which changes the frequency of the internal cavity. This combination provides a mode-hope free scanning range up to 50 GHz and linewidths better than 20 MHz. However, as a result of modulation of the diode current the output power of the laser varies as the wavelength is scanned. We use an acusto-optical modulator (AOM) and a PID loop to stabilize the output power of the laser. The signal to control the diode current and the grating controller are connected to the computer, which controls

the experiment.

We monitor the resonant laser using a high precision wavemeter (WS7 from HighFinesse). The wavemeter works based on interference patterns generated in its interferometers. The spatial interference patterns from a Fizeau interferometer are projected on a CCD line array and read out. The wavemeter has a relative accuracy of around 10 MHz. The wavemeter also outputs the interference patterns. We monitor these patterns to assure the single mode operation of the laser. Figure 4.3 shows two different interference patterns while scanning the laser frequency. The y-axis in this figure shows the pixel number on the CCD array while the x-axis shows the scan step. The pattern in figure 4.3(a) is smooth, the peaks are equally spaced and vary continuously as the laser frequency is scanned. On the contrary, the pattern in figure 4.3(b) changes abruptly around the step number 200. At this point, the laser has more than one frequency component. It is also important to note that the wavemeter might still read a single frequency, although the laser has several frequency components. We also monitored the laser with a Fabry-Perot interferometer to check the validity of this method and we did not run into any contradictions.

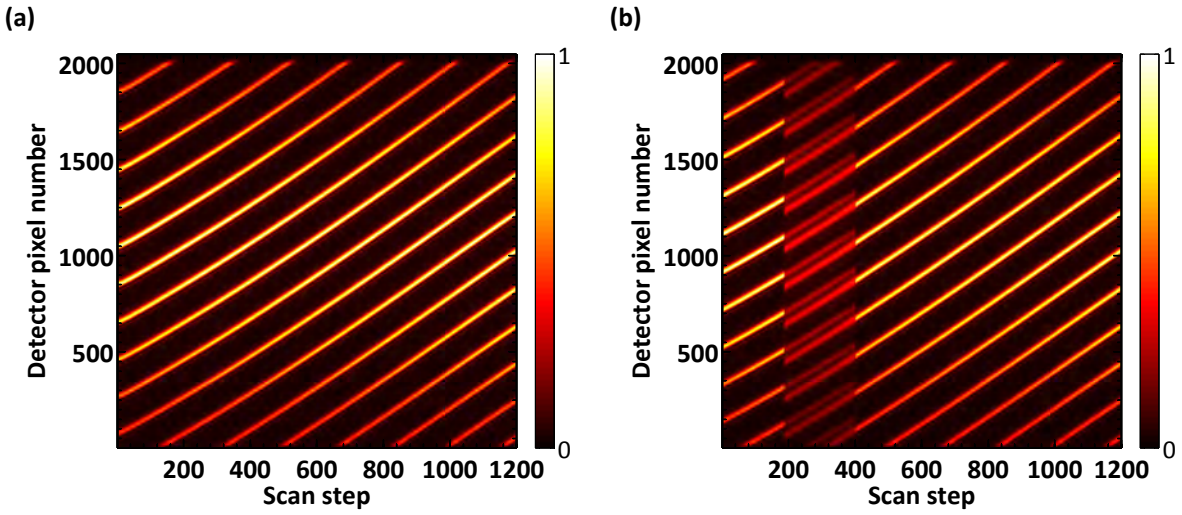

Figure 4.3: Sample interference patterns recorded from the interferometer. (a) A scan without mode hop or mode competition. The laser is single-moded during the scan and the wavelength is swept continuously. (b) A sample scan with a mode competition. The interference patterns are ruined between scan steps 200 to 400. This indicates that there are more than a single lasing line.

We use a widely tunable Ti:Sapph laser in CW mode as the repump laser. In the early versions of the experiment, the laser beam went through a chopper wheel to switch the laser on and off. However, for the most of the later measurements, the laser beam is sent through an AOM to control the laser intensity in timescales of µs, as shown in figure 4.2(d). A polarizing beamsplitter and a half-wave plate are used to match the polarization of the laser to the secondary waveguide mode. The AOM is controlled by the microcontroller to realize different measurements which will be discussed later in this chapter.

The structural configuration of the setup with cryostat sitting on high precision stages makes the

optical path rather unstable and the alignment of the setup drifts over time scales of seconds. In extreme cases, the transmission of the system can vary by 50% over time scales of minutes. Therefore, for the transmission type measurements, it is very important to have a reference measurement to eliminate these types of fluctuations. Also parasitic Fabry-Perot resonances due to imperfect optical components can make the transmission type measurements hard to interpret. The best method to circumvent these problems is to turn off the QD transition and acquire a reference transmission measurement [147, 148]. One can then normalize the transmission of the system while the QD is active to the reference transmission. If the two measurements are done with very short delays, the resulting spectrum is only affected by the presence of the QD.

The repump laser plays an important role in modulating the QD transition and providing the reference measurement. The repump laser can be used in two different ways to obtain a reference signal. One method is to shift the QD transition frequency by increasing the intensity of the repump laser. The other method would be to turn off the repump and wait for a short amount of time for the QD transition to go dark and then acquire a reference measurement. Throughout this chapter we will use both methods. However, we use the second method for the measurements in the next chapter.

The signal from one of the APDs is sent to a pulse shaping circuit and then to a microcontroller that counts the number of detection events in given time windows. The microcontroller switches the intensity of the repump laser ON and OFF, switches the APDs on and off through the gating signal and sends marker signals to the time correlator. The microcontroller is connected to the computer through a USB port. This connection is used to acquire the data and to send commands to the microcontroller.

A typical scan runs as follows: The computer changes the voltage of the diode laser, reads out the frequency of the laser from the wavemeter, and subsequently sends a command to the microcontroller providing certain instructions on the modulation of the repump laser and photon counting intervals. Depending on the command received from the computer, the microcontroller turns the repump signal ON and OFF for a certain amount of time and activates the APDs. It starts the data collection, typically for 40 ms, and sends the collected data to the computer at the end. The cycle continues until the desired scan range is reached.

4.3 Preliminary experiments on the first generation of samples

We did the initial transmission type measurements on the sample that was also used for demonstrating the efficient QD-PCW coupling, in section 3.5.4. The sample is 160 nm thick and has a nominal QD density of $100/\mu m^2$. Figure 4.4(a) shows the SEM image of the sample. The main difference between this sample and final design (discussed previously in section 4.2.1) is the out-couplers that are directly connected to the PCW. The lattice constant of the slow section is equal to 235 nm and the hole radius is 73 nm. We first characterize the sample under aboveband excitation. Figure 4.4(b) shows the emission spectrum of the sample under strong aboveband excitation on the slow-light section while the emission is collected from the grating. The band-edge of the slow-light section is around 926 nm

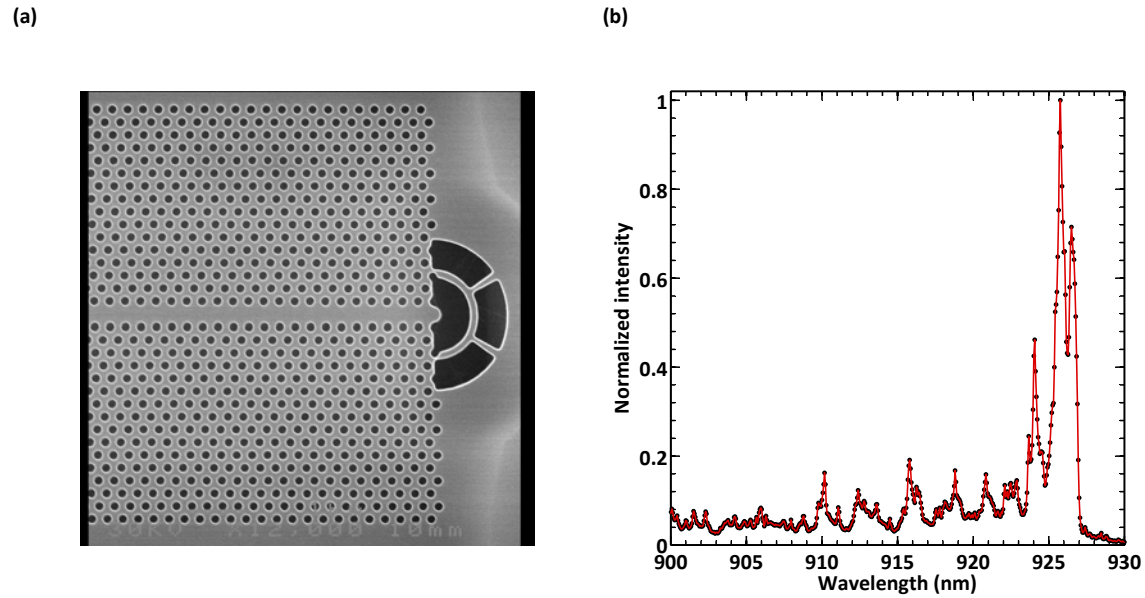

Figure 4.4: (a) SEM image of the sample, showing half of the sample with a grating out-coupler. This sample was the first generation of samples and the grating is directly connected to the PCW. (b) Emission spectrum of sample under high-power aboveband excitation.

and the waveguide has a good transmission over 25 nms.

We turn down the aboveband power and look for single dot lines in the aboveband spectrum. We then turn off the aboveband laser and couple the resonant laser through one of the gratings. Next, we tune the resonant laser to -0.5 nm from the observed QD lines and scan it for around 1 nm in several steps. The intensity of the resonant laser was around 400 pW on the sample which corresponds to $\sim$ 5000 detection events per second on the APDs. However, we failed to observe any signal that we could explicitly attribute to the QD lines observed under aboveband excitation. After several scans over a wide range of frequencies, we noticed extra noise at certain frequency ranges, see figure 4.5(a). These wiggles were previously observed in our group [181] while scanning for the QDs in the same structure. This noisy behavior is most likely related to a QD transition which blinks at time scales of seconds and hence modulates the transmission of the PCW at these time scales. Since the each measurement step takes around one second, the blinking behavior appears as excess noise in the data. The temperature dependence of these wiggles was also checked and it was observed that the wiggles red shift with increasing temperature, as expected from a QD line [181]. The other clear feature in these scans is the relatively narrow Fabry-Perot like fringes in the transmission signal, see for example 4.5(a). These parasitic Fabry-Perot resonances result from residual reflections in the optical setup, most probably between the sample and the beamsplitter on top of the microscope.

We briefly study the time scales of these fluctuations. Figure 4.5(b) shows a time trace of the transmission of the waveguide while very slowly (10 MHz per second) varying the laser frequency in the center of these wiggles. Clearly, the intensity of the transmitted light varies in abrupt steps down to certain values on time scales on the order of tens to hundreds of milliseconds. A similar behavior has been observed in the past for resonance fluorescence from QDs [132, 144, 152], often on slightly

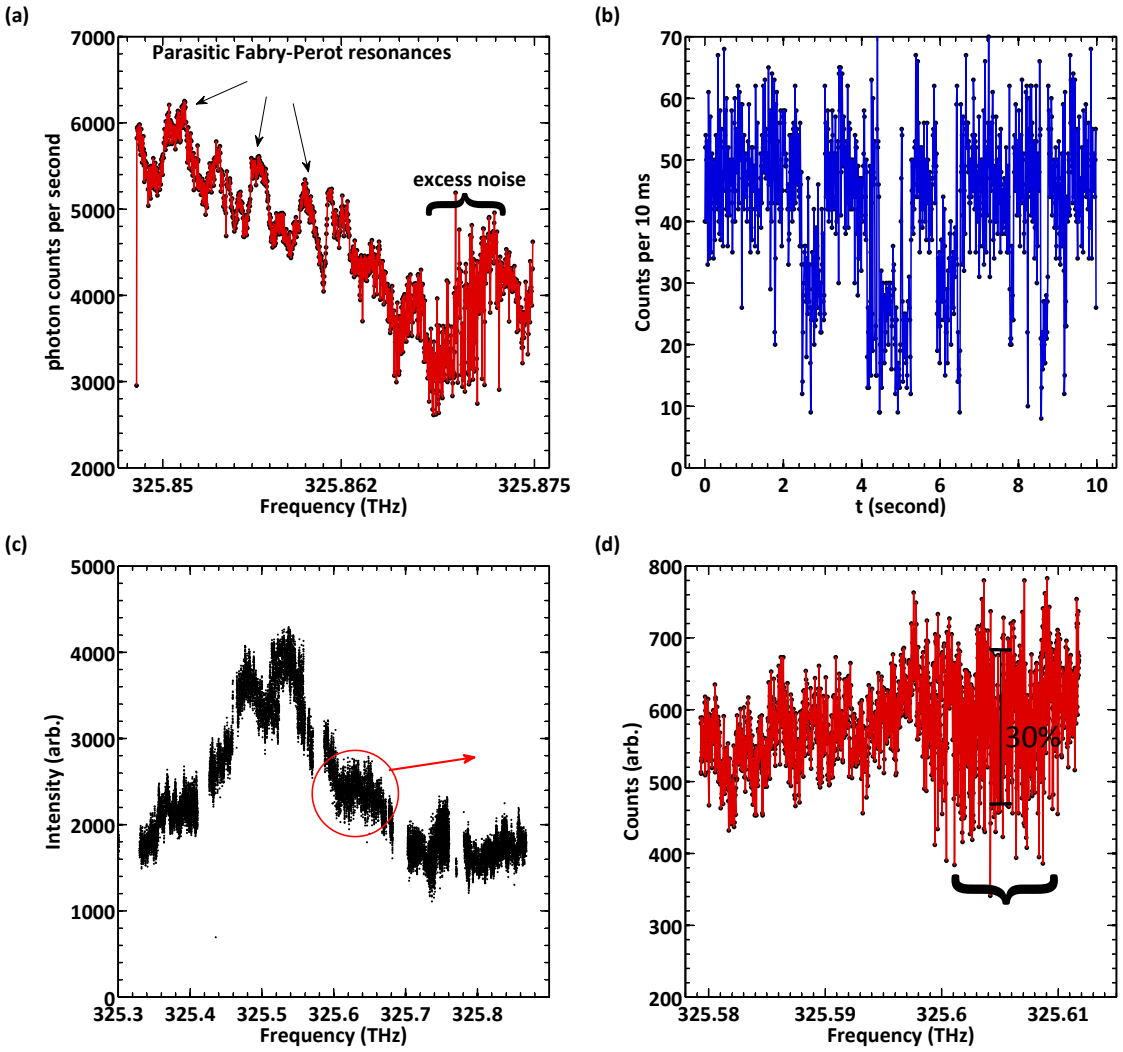

Figure 4.5: (a) Transmission spectrum of the waveguide while scanning the resonant laser over short spectral range. The important feature in this scan is the excess noise on the right hand side of the plot, marked by a bracket. Also notice the fine Fabry-Perot peaks in the scan. These are due to multiple reflections between some of the optical elements in the setup. (b) A time trace taken while slowly (10 MHz per second) scanning the resonant laser around 325.605 THz. The transmitted number of photons changes in abrupt steps. (c) Collection of several short range scans. The big transmission peak results from the reflections in the transition from the slow waveguide to the fast waveguide. (d) A zoom in on the area marked by the red circle in part (c). The observed wiggles are more intense than in part (a).

shorter time scales. Most probably these abrupt changes in the transmission of the waveguide are due to blinking in the QD transition through a carrier escape or trapping of a charge inside the QD or traps around it. It is also important to mention that during these scans the laser frequency is changed in steps of 10 MHz per second and duration of some of the fluctuations in the photon detection events correlate with this value. However, we double checked that laser spectrum was single peaked all the time. The only other explanation for these dips could be higher order resonances of some other dots.

Fluctuations in figure 4.5(b) with a width of one second correspond to approximately 10 MHz change in the laser frequency. However, one would expect a much broader resonance than 10 MHz for the higher transitions of a QD. We also observed that these wiggles disappear when we apply a weak aboveband laser and reappear when the aboveband is cut off. We tried to use this fact to obtain a differential signal; however, the revival time of the transition was longer than 1 second.

Figure 4.5(c) shows a transmission spectrum of the waveguide over a spectral range of 600 GHz. The big peak in the center of the spectrum is most probably due to residual reflections at the interface of the slow and the fast waveguide. These reflections form cavities with Q-factors up to 1000. We observed several of the mentioned wiggles at different frequencies, one is marked in 4.5(c) with red circle. Figure 4.5(d) shows a zoom-in on the most intense signal observed in the measurement with contrast on the order of 20-30%.

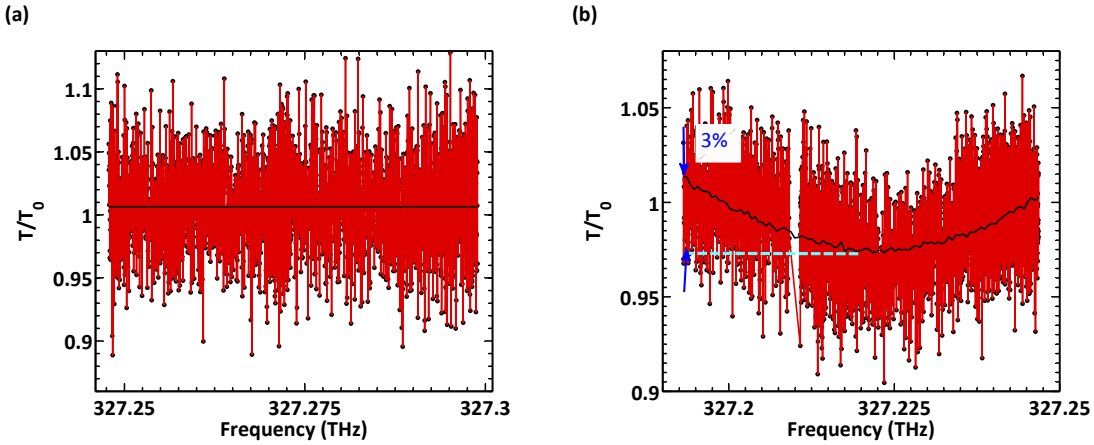

Figure 4.6: (a) Normalized transmission spectrum of the waveguide (T/T_0). T/T_0 is a flat line when there are no QDs in resonance with the laser. We used a chopper to modulate the aboveband laser and we integrate the counts in the ON and OFF periods of the laser and divide the counts in the ON window by the counts in the OFF periods to obtain the (T/T_0). (b) A QD creates a small dip in the transmission of the system. We made sure that the feature is not due to laser itself. The width of the dip is as wide as 15 GHz, and it is broadened due to charge fluctuations and pure dephasing. Solid black lines are guides to the eye.

Parasitic Fabry-Perot resonances in these measurements make it hard to observe the signatures of QDs. One way of eliminating the effect of the parasitic Fabry-Perot resonances and other fluctuations in the transmitted field intensity is to shift away or turn off the QD and take a reference measurement, as discussed before. One can divide the actual measurement with the reference measurement to extract the T/T_0. T/T_0 only includes the signal from the QD and all the parasitic effects are eliminated. Figure 4.6(a) shows an example of such a measurement. This type of spectrum is called transmission spectrum of the system. The transmission spectrum for the most of scans we have done is a flat line as in figure 4.6(a). The advantage of these types of measurement is to remove any fluctuations in the detected light intensity that are not from the QD layer. Elimination of the parasitic Fabry-Perot resonances allows detecting the small signals easily. Figure 4.6(b) shows a dispersive transmission dip observed during these scans. The dip has a full width half max of 15 GHz. This linewidth is too wide

for a typical QD line and is most probably broadened due to charge fluctuations in the environment. We checked that this feature is not due to flaws in the measurement setup, e.g. laser having several frequency components or chopper wheel acting asynchronously. We also observed a spectral shift in this dip, with increasing the aboveband power, which is another signature typical of QDs [161].

Theoretically, we expected much stronger and stable dips in our transmission. However, lack of strong contrast in the transmission measurements can be attributed to several facts. First of all, the high density of the QD on the sample could play a role. Most experiments that have reported strong resonant signals and narrow linewidths are done on samples with low densities of QDs [153,154]. This could be due to the fact that a lower density of QDs means less defects and less traps in the QD environment. The second important reason could be the fact that the sample was fabricated one year before the first resonant measurements were performed on it and it was used for several other measurements. The sample could degrade from oxidization and also the many cool-down and heat-up procedures (thermal cycles). Moreover, during the period that the sample was in the cryostat, there was an accident where the vacuum broke while the sample was still cold. A thick layer of ice formed in the cryostat and on the sample which might have created defects on the surface of the sample as well and further degraded its quality. Hence, we fabricated a new batch of structures on a lower density sample and repeated the measurement. The next section describes some of these measurements.

4.4 Measurements on the second generation of the samples

We fabricated a new set of structures on a sample with lower density of QDs. The design of the sample is discussed in section 4.2.1. The insert in figure 4.1(a) shows SEM image of the sample. The density of the dots on the new generation of the samples is around $10/\mu m^2$. We observed two slightly different behaviors during the course of the measurements. We observed a strong contrast around 30% during first 3 days as the sample was fresh. However, after a few thermal cycles, the contrast of the signal dropped, the band-edge of the waveguide moved slightly and the response of the QD transition to the repump laser changed. We present the measurements in the chronological order as they were performed.

4.4.1 Early stages of the measurement

We started by characterizing the sample under aboveband excitation and later measured its transmission spectrum. Figure 4.7 shows the emission spectrum of the sample under strong and weak aboveband excitation. We excited the sample in the middle of the slow-light waveguide and collected the emission from the straight out-coupler. The excitations wavelength was 800 nm. Figure 4.7(a) shows the emission spectrum under strong aboveband excitation. Under strong excitation, the single emitter lines are saturated and hence the spectrum is dominated by the density of states of the nanostructure. The band-edge of the slow-light waveguide is at 916.7 nm, and as explained earlier, the transmission and emission spectrum of the waveguide are dominated by the overlap of slow-light

band and fast-light band, the yellow area in 4.1(a). Part (b) of the figure shows the emission spectrum under weak aboveband excitation. Several single emitter lines with different intensities are visible.

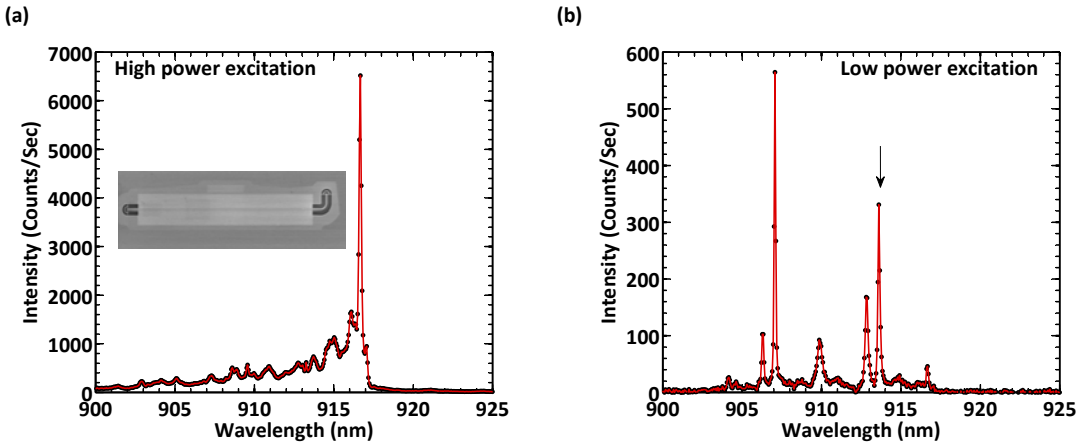

Figure 4.7: (a) Emission spectrum of the second generation sample under high-power aboveband excitation. The excitation spot is in the slow-light region of the structure. The excitation wavelength is around 800 nm. The excitation power corresponds to 20 µW on the sample. The sharp feature around 916.7 nm is the band-edge of the waveguide. In this excitation regime the single dot lines are saturated and the emission spectrum corresponds to the DOS of the nanostructure. (b) Emission spectrum of the waveguide under the same conditions as in part (a) but at a much lower power. The excitation power corresponds to 150 nW before the lens. Several single dot lines are visible in the spectrum. The black arrow points to the exciton that is the target of most of the experiments in this thesis.

After identifying several QD lines under aboveband excitation, we started the resonant transmission type measurement. We tuned the resonant laser to close proximity of one of the QD lines, marked with arrow in 4.7(b). We launched the resonant laser in to the waveguide from the bent grating and collected the transmission from the straight grating. The intensity of the resonant laser is denoted by $P_{resonant}$ hereafter. For the measurements discussed in this subsection, we used a 800 nm repump laser to produce reference T_0, and also to activate the QD transitions [161]. We modulated the repump laser with a frequency of 500 Hz. The power of the repump laser is denoted by P_{repump} hereafter. Also it is worth adding that the resonant transmission measurements reported in this subsection were done after four cool-down and heat-up cycles.

Figure 4.8 shows the transmitted photon rates during the ON and OFF periods of the repump laser. A clear dispersive signal is observed around 328.01 GHz during the OFF periods of the repump laser 4.8(a) top. This signal is observed within 30 GHz distance from the observed emission line, marked with arrow in 4.7(b). During the ON periods of the repump laser, the QD transition is not observed in the transmission spectrum. Most probably, the QD line shifts to a higher frequency; however, we scanned the region around ±100 GHz from the initial position of this signal and we did not find any other signatures. This could mean that the ground state of the QD changes to a different configuration, most probably to a different charge configuration. Interestingly enough the transition revives quickly after the repump is turned off. Figure 4.8(b) shows the transmission spectrum of the

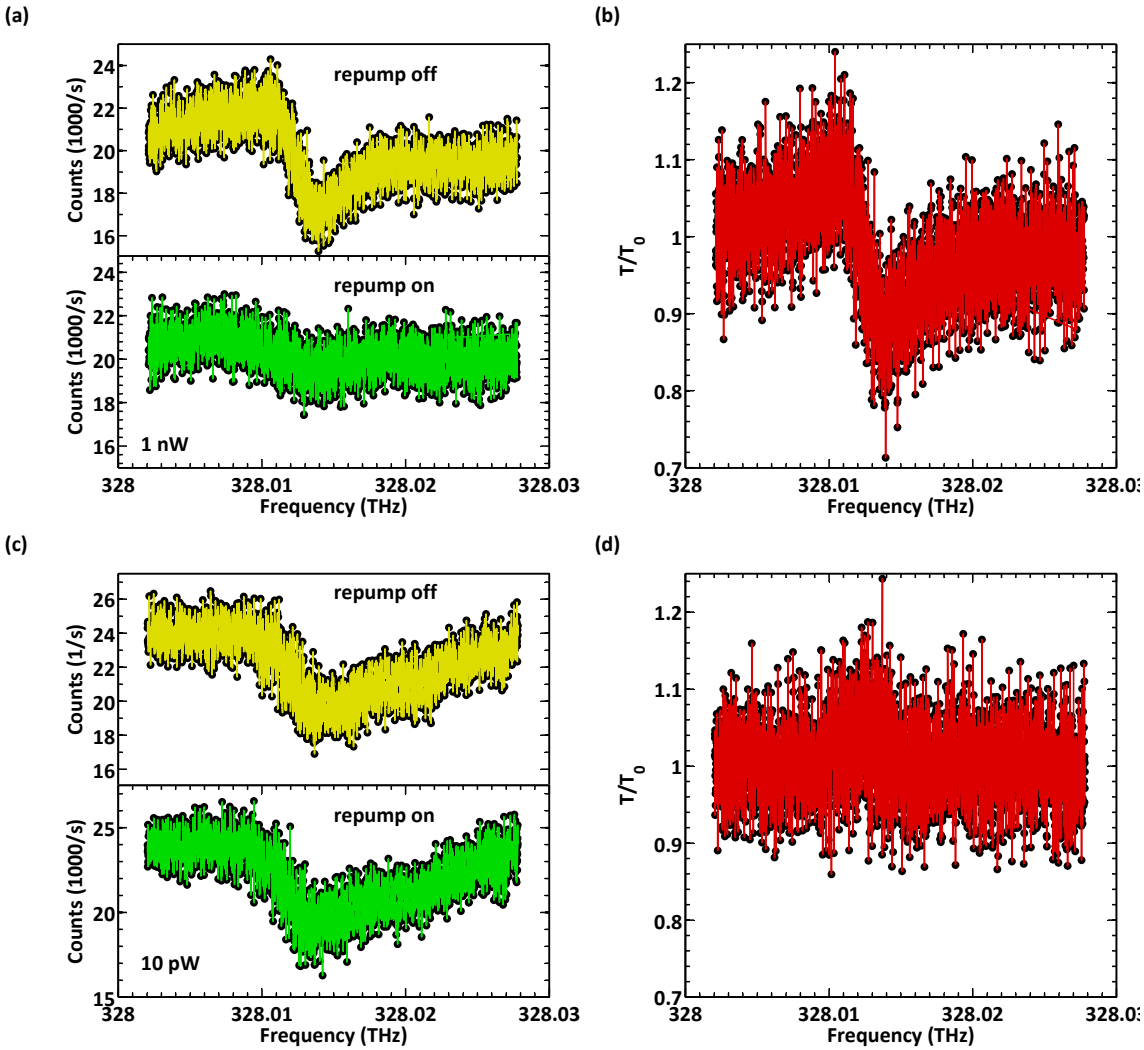

Figure 4.8: (a) The transmitted photon flux during the OFF periods of the repump laser, top and during the ON periods, bottom. (b) Transmission spectrum of the waveguide under conditions in (a). The spectrum is obtained as ratio of the top plot over the bottom plot in part (a). The P_{repump} was around 1 nW. As seen on these scans, during the repump ON period, the QD signal is shifted away (or turned off) to a high degree. (c) and (d) The same as (a) and (b) but with much lower repump intensity. When repump laser is turned down, the revival effect prevails while the QD does not shift away during the ON period. Also clearly the width of the signal in part (c) appears to be larger than part (a).

sample, T/T_0. We divide the signal in the top part of the part 4.8(a) by the one in the bottom part to get T/T_0. As clear from 4.8(a) and 4.8(b), a peak and a dip is observed in the transmission of the system. This is due to a Fano-type resonance between the reflections on the slow to fast waveguide transitions and the light scattered from the QD. More details and a full theoretical treatment will be presented in the next chapter.

Figure 4.8(c) and (d) present the transmitted photon flux and the transmission spectrum of the

waveguide under very weak repump intensity, P_{repump} =10 pW. The dispersive behavior can still be observed in 4.8(c); however, the transmitted photon fluxes in the two periods of repump ON and OFF are almost the same. Also the width of the signal in part (c) appears to be wider than the one in part (a). We attribute this to reduced spectral diffusion as a result of the applied repump laser [152]. We repeated these measurements while the repump laser was turned off totally and the dispersive signal from the QD totally washed away.

Another interesting feature of these measurements is the suppression of the parasitic Fabry-Perot resonances observed in the first generation of samples, see figure 4.5. The new design of the gratings with the attached ridge waveguides and also the orthogonal polarization of the two out-coupling gratings help to suppress these artifacts.

4.4.2 Later stage of the measurements

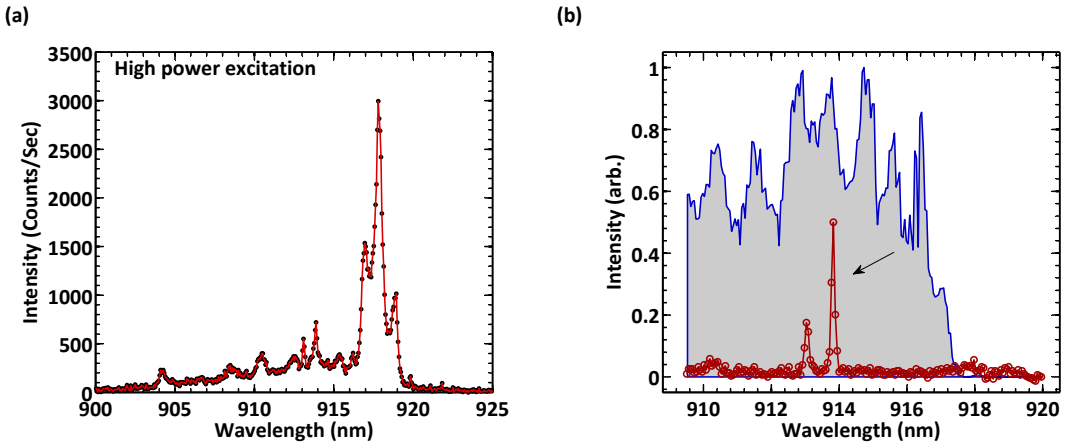

Figure 4.9: (a) The emission spectrum of the sample under high power aboveband excitation. The band-edge of the sample appear to have shifted by as much as 2 nanometers relative to initial value. Also the band-edge is not as sharp as the initial measurements. (b) Emission spectrum of the sample under weak aboveband excitation, red dotted curve. This spectrum is very similar to the one in figure 4.7(b). The gray area with blue outline shows the transmission spectrum of the waveguide over a large range. This spectrum has a resolution around 30 GHz.

The sample quality degrades over time because of oxidization and also due to the cool-down and heat-up cycles. After several days of the measurement the sample spectrum changed. Interestingly, this change was abrupt and potentially due to the cool down procedure where the helium flow was not regulated correctly and the heater worked under full power for several minutes at the same time as there was a high helium flow. Figure 4.9(a) shows the emission spectrum of the waveguide after the abrupt change of the spectrum. The band-edge appears to have shifted as much as two nanometers. Also the shape of the band-edge is now smoother compared to the past. The dotted red line in figure 4.9(b) shows the emission spectrum under low-power excitation. The low power spectrum is very similar to the low power spectrum in earlier stages of the measurement, see figure 4.7(b).

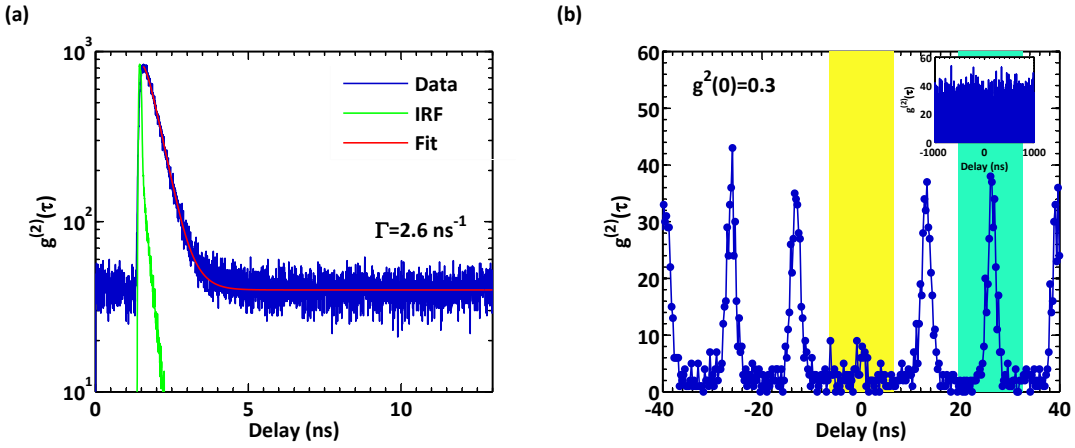

Figure 4.10: (a) Time-resolved photoluminescent from the QD under pulsed wetting layer excitation. The red curve is fit with a single exponential function. The green curve is the IRF of the setup. (b) Auto correlation measurement of the emission. The anti-bunching around the zero time-delay indicates that the line understudy belongs to a single emitter. The $g^2(0)$ is 0.3. The inset shows the $g^2(\tau)$ on time scale of 1 µs. The QD does not blink on these time scales.

The gray area with blue outline in figure 4.7(b) shows the transmission spectrum of the sample. This spectrum has been obtained by tuning the resonant laser under 30 GHz step and collecting the transmitted light intensity. In this stage of the measurement the dot line of interest for us is close to the resonance of the Fabry-Perot cavity.

Now that we have found a suitable candidate we perform a detailed characterization before proceeding to the resonant transmission measurements. The blue curve in figure 4.10(a) shows the time-resolved photoluminescence for the QD line under wetting layer excitation. The curve fits well with a single exponential function. The red curve is the fit from the theory. The fitting procedure is the same as explained in 2.2.1. From the theoretical fit, the decay rate of the QD is 2.6 ns^{-1}. From the single exponential nature of the decay, we conclude that the exciton line is a charged exciton. This conclusion is based on the observation that the neutral exciton have dark states and the spin flip between the bright and dark state results in a bi-exponential decay in the photoluminescence curve [7].

Figure 4.10(b) shows the autocorrelation measurement of the QD line under wetting layer excitation. The excitation power is around the saturation power. The clear anti-bunching around the zero time-delay confirms that the line under study is a single exciton line. We extract the value of $g^2(0)$ by integrating the counts in a 13 ns window around the zero delay peak, marked by yellow area in 4.10(b), and dividing it by the average of the area under 5 of the near peaks. We extract the value of $g^2(0)$ to be 0.3. This confirms that the transition is coming from a single QD. The inset is this figure shows the $g^2(\tau)$ over longer time scales. The graph appears to be flat indicating lack of any blinking on time scale of μs.

Following these characterization steps we continue to resonant transmission scans. We use a

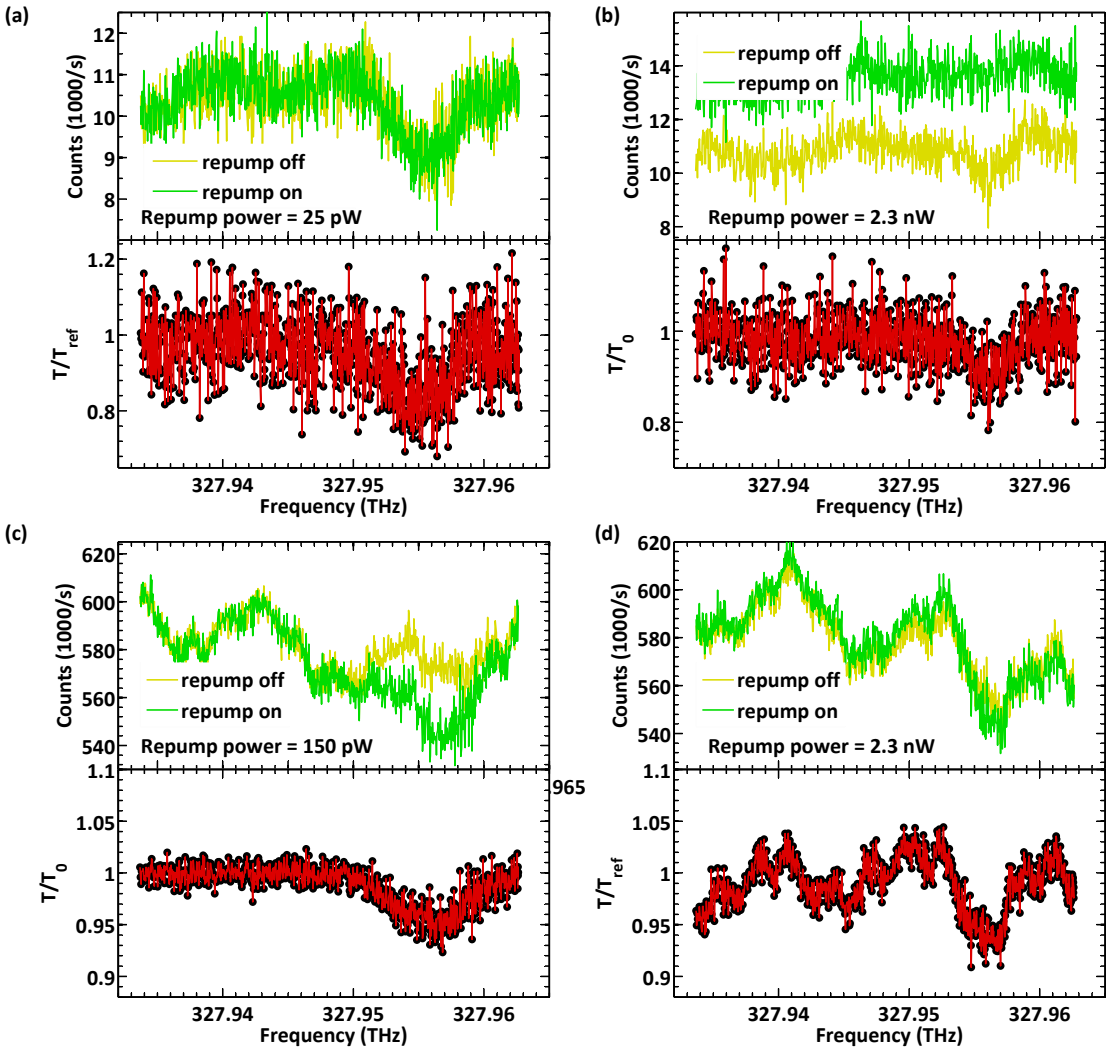

Figure 4.11: (a) The transmitted photon flux, top panel, and the transmission spectrum of the waveguide, bottom panel, under resonant excitation with 4 pW. The yellow and the green curves belong to the ON and the OFF periods of the repump laser respectively. The repump power is 25 pW. The QD line does not wash away in the OFF period of the repump laser. Hence, the transmission spectrum is normalized to a different reference measurement. (b) The same as (a) but with P_{repump} =2.3 nW. We extract the transmission spectrum by dividing the photon flux in the OFF periods of repump laser by the photon flux in the ON periods of the repump laser. Note that we have subtracted background counts in the repump on period when extracting the lower panel in this section. (c) Same as the pervious parts but with 240 pW resonant laser and 150 pW repump power. The QD transition turns off quickly after the aboveband laser is turned off hence we extract the transmission spectrum by dividing the photon flux in the ON period to the photon flux in the OFF period. (d) The repump power is 2.3 nW and the resonant power is 240 pW. The bottom panel is extracted by dividing the photon flux in the ON period by a reference measurement that was taken later with repump laser turned off. However, the curve is not flat far from the QD transition, due to setup drifts. This makes the curve unreliable and hard to interpret.

repump laser close to the edge of the wetting layer to get a better contrast. The measurement procedure is the same as section 4.4.1. The repump laser is turned ON and OFF with a frequency of 500 Hz. We integrate the photon flux during the ON and OFF periods. We extract the transmission spectrum of the resonant laser by dividing the two numbers. However, depending on the intensity of the repump and the resonant laser, the QD transition behaves differently over the ON and OFF periods. Figure 4.11 shows the transmitted photon flux and the transmission spectrum of the waveguide under different resonant and repump powers. The top panel in figure 4.11(a) shows the transmitted photon flux and the bottom panel shows the transmission spectrum. The repump laser power is relatively low, P_{repump} =25 pW. The resonant laser intensity is $P_{resonant}$ =4 pW. When P_{repump} and $P_{resonant}$ are low, the transition is revived and the blinking is cured by the repump laser during the ON period of the repump laser. However, during the OFF period of the repump laser the transition does not go to the dark state due to the low $P_{resonant}$ and relatively short OFF periods (2 ms). For low resonant and repump powers, the photon flux is equal during the ON and OFF periods of the repump laser. Hence one needs to normalize to the photon flux to a reference measurement to extract the transmission spectrum. We extract the reference measurement by turning the repump laser totally off during a measurement.

Part (b) of figure 4.11 shows the same plots as (a) but with a higher value of repump laser, P_{repump} =2.3 nW. The repump laser revives the QD line during the ON periods. However, since the P_{repump} is high enough, the QD frequency shifts away during the ON period. Note that the resonant laser is still low and the transition does not go to the dark state during the OFF periods of repump laser. When the repump power is high and the resonant power is low, the QD transition washes away during the ON periods of repump laser and the transmission spectrum can be extracted as the ratio between the photon flux in the two windows. The transmission dip in 4.11(b) is two times less than the ones observed in 4.8 which we attribute mainly to increased spectral diffusion and blinking of the QD transition, see next chapter for a detailed description and analysis.

Parts (c) and (d) of this figure show the photon flux and transmission spectrum of the system for significantly higher resonant laser power, $P_{resonant}$ =240 pW. The P_{repump} is 150 pW in part (c), and P_{repump} =2.3 nW in part (d). When $P_{resonant}$ is increased while the P_{repump} is relatively low, figure 4.11(c), the QD transition quenches shortly after the repump laser is turned off and stays off as long as the repump laser is OFF. Therefore, we divide the counts on the ON period by the counts in the OFF period to extract the transmission spectrum of the waveguide. The dip in transmission spectrum in part (c) is half the dip in parts (a) and (b) as a result of the higher excitation power and saturation of the emitter.

Figure 4.11(d), shows the photon flux and the transmission spectrum of the system when the repump laser and the resonant laser are both high. The photon flux is around the same value in the ON and the OFF periods of the repump laser. Therefore, we normalize the transmission spectrum to the reference measurement. The main issue with normalizing to a reference measurement that is taken after some time is that the drift in the alignment of the optical setup changes the transmitted photon flux, hence the extracted spectrum is not clean and reliable, as seen in the bottom panel of part (d) compare to the bottom panel of the part(c).

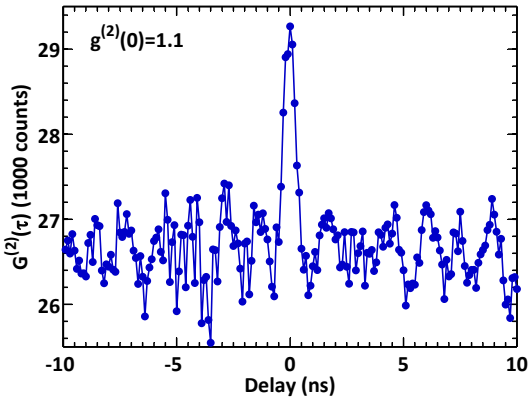

Figure 4.12: Autocorrelation function of the transmitted light while the laser is on resonance with the transmission dip. The resonant laser power is 167 pW and the repump laser power is around 400 pW. The $g^2(0)$ is around 1.1. This value is without any de-convolution of the IRF of the detection setup, and the actual $g^{(2)}(0)$ is as high as 1.25 after deconvolution with the setup IRF. This will be discussed in details in the next chapter.

At this stage, we check the photon statistics of the transmitted light. According to the theory [182], in the case of a single emitter efficiently coupled to the waveguide, the transmitted photons bunch. For a coherent field, significant portion of the single photon components get reflected by the emitter, while multi-photon components have an enhanced probability of being transmitted; see next chapter for a complete explanation. In order to assure that the dip in the transmission spectrum is due to a single emitter, we did auto-correlation measurements on the transmitted light while the resonant laser was tuned in the dip in the transmission spectrum of the waveguide. We choose the $P_{resonant}$ to be 167 pW and the repump laser power is around 400 pW. Figure 4.12 shows the results of the autocorrelation curve versus delay-time, $G^2(\tau)$. The peak around the zero time-delay indicates bunching of the transmitted photons as expected from the theory. The value of the normalized autocorrelation function at zero delay ($g^2(0)$) is around 1.1. This value is directly read out from the curve without de-convolving the ($g^2(\tau)$) and the actual value is around 1.25, since the IRF of the measurement setup is relatively broad. This will be discussed in the next chapter in more details. As a sanity check, we turned the repump laser OFF and repeated the measurement. The result was a flat histogram as expected from a coherent state.

4.4.3 The final measurements

The data recorded in the previous section clearly shows modulation of the transmission of a PCW with a single quantum dot. However, the data quality is not very good and the behavior of the QD transition versus P_{repump} makes it hard to interpret the data. In order to extract the transmission spectrum of the waveguide more reliably, we decreased the modulation frequency of the repump laser to 2.5 Hz. The reason behind this is that when the repump laser is off for significantly long times the QD transition would go off for the range of the P_{repump} and the $P_{resonant}$ in our experiments. This

will be further investigated in the rest of this chapter when we investigate the lifetime of the ground state.

Figure 4.13(a) shows the transmitted photon flux under $P_{resonant} = 1.4\,\text{pW}$. The yellow curve shows the detected count rates during the ON periods of the repump laser while green curve shows the count rates during the OFF periods of the repump laser. The whole measurement now takes longer than before, around 12 minutes. The bigger fluctuation on the detected photon flux (the left hand side of the left side 4.13(a)) are due to drifts in the position of stages under the cryostat. Figure 4.13(b) shows the transmission spectrum of the system reconstructed from part (a). The small peak and slight asymmetry in the transmission spectrum are results of the Fano-resonance in the system. However, since the QD is close to the resonance of the cavity, the Fano-resonance shape is less pronounced than in figure 4.8.

The top panel in part (c) of figure 4.13 shows the transmitted photon flux and the transmission spectrum of the system under much higher resonant laser power, 4.17 nW. The collected light has to be attenuated by a factor of around 50 to avoid damages to the APDs. The repump laser intensity is set to $P_{repump} = 850\,\text{pW}$. The bottom panel shows the transmission spectrum of the system. The contrast of the dip decreases with increasing resonant laser power due to saturation of the QD transition. Figure 4.13(d) shows the same quantities but with $P_{repump} = 1.5\,\text{nW}$. The transmission dip appear to be narrower when the repump laser is higher. We attribute this to reduction of charge fluctuations for higher repump laser power. However, a further increase in P_{repump} by a factor of two totally quenches the transmission dip during the ON periods of the repump laser. The behavior is very similar to the one reported in the supplementary of reference [177].

4.4.4 Effect of the repump wavelength and intensity on the transmission dip

As seen in the previous section, the repump laser has several effects on the QD transition (the dip in the transmission spectrum). We first study the effect of the repump laser wavelength on the contrast in the transmission spectrum of the system. Figure 4.14 shows the observed transmission dip versus the wavelength of the repump laser. The transmission dip appears to be maximum when the wavelength of the repump laser is around the wetting layer of the sample. This is probably due to the fact that creating charge carriers in the wetting layer more effectively influences the QD and the traps around it. In contrast when the wavelength of the repump laser is around 830 nm and below, more carriers are created in the bulk GaAs, which results in more free charges in the environment of the QD. The other interesting feature in figure 4.14 is the sharp increase in the dip contrast around 858 nm. The same behavior is observed in the PLE spectrum of the sample. That is, the emission intensity of the QD line increases sharply around this wavelength. We attribute this to an absorption resonance inside the wetting layer. Note that the solid black line is a mere guide to the eye, and our measurements are particularly down sampling the range between 840 nm to 850 nm. Since the photo-absorption is low in this range, the repump laser is not expected to be effective.

We also observe a shift of the transmission dip with increasing repump power. Figure 4.15 shows

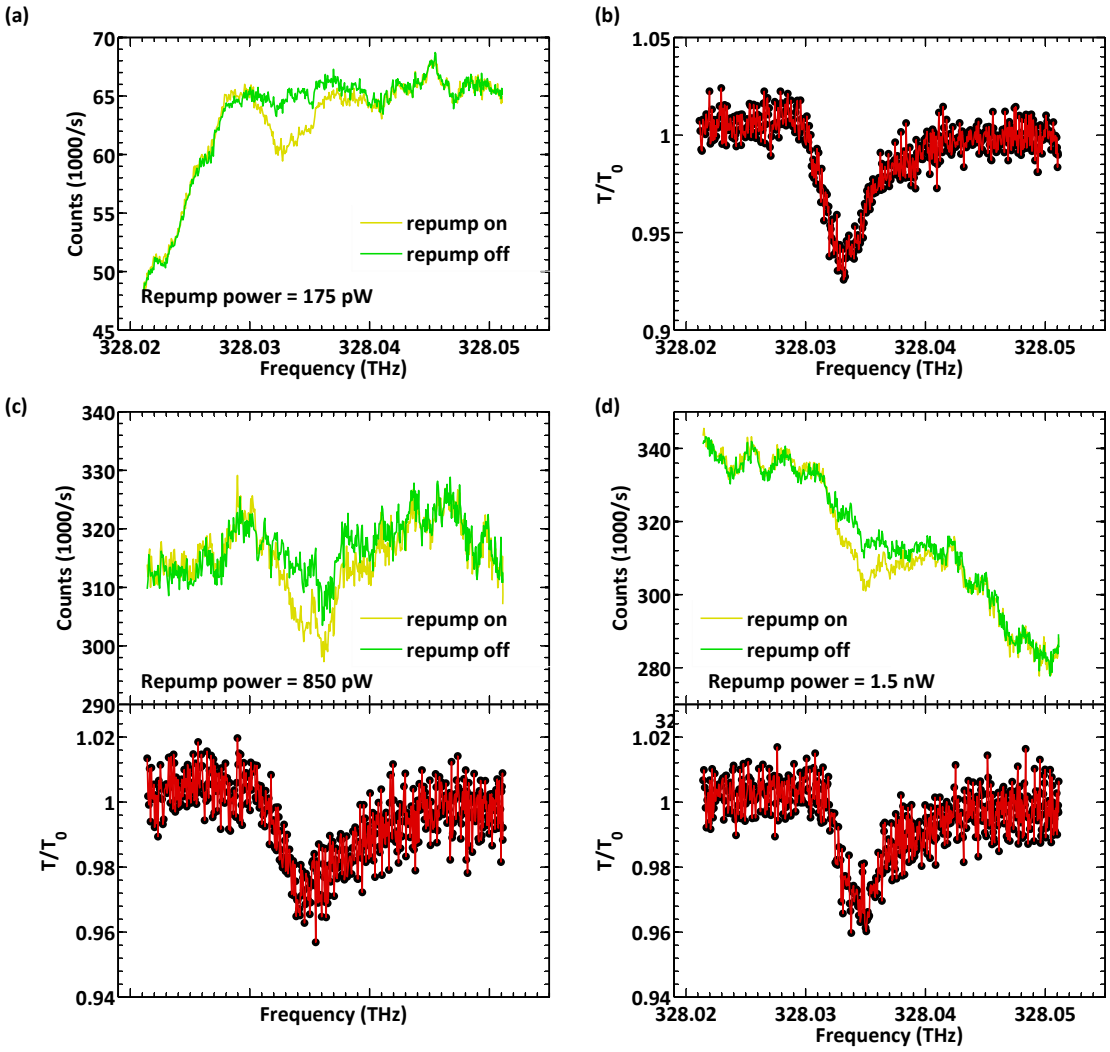

Figure 4.13: (a) The transmitted photon flux under weak resonant excitation ($P_{resonant} = 1.4\,\text{pW}$). $P_{repump} = 175\,\text{pW}$ and the repump laser is modulated with 2 Hz to assure that the QD transition becomes dark during the OFF period of the repump laser. The yellow curve and green curve show the transmitted photon flux in the ON and OFF periods of the repump laser respectively. (b) The transmission spectrum of the waveguide under the same conditions as (a). Overtime the transmission dip has reduced to around 8% due to sample degradation. (c) The transmitted photon flux, and the transmission spectrum under strong resonant excitation, $P_{resonant} = 4.17\,\text{nW}$. The count rates are after attenuation by a factor of 50. The attenuation is necessary to avoid damages to the APDs. The repump laser power is 850 pW. (d) The same as (c) but with $P_{repump} = 1.5\,\text{nW}$. The width of the transmission dip reduces with increased repump laser power.

the frequency of the transmission dip versus P_{repump}. The measurement procedure is the same as in figure 4.11 (The repump laser is turned ON and OFF at 500 Hz). The frequency of the transmission dip appears to first red shift and then blue shift while increasing the repump laser intensity. This shift is also observed in reference [161] and attributed to the quantum confined stark shift due to charge configurations in the environment of the QD. The intensity of the resonant laser is around 8 pW for

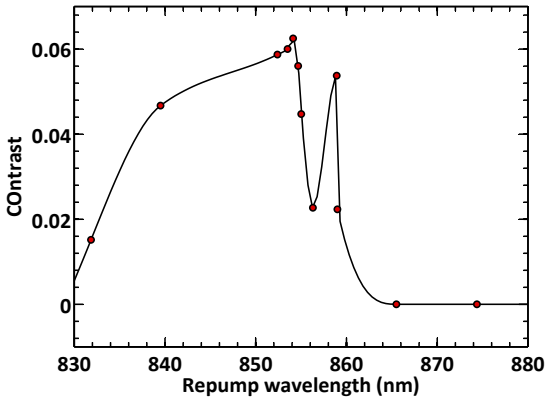

Figure 4.14: Contrast of the transmission dip versus the repump wavelength. $P_{resonant}$ is around 8 pW. The repump laser intensity is varied to get the maximum contrast. The transmission dip appears to be maximum when the wavelength of the resonant laser is inside the wetting layer. The sharp peak around 858 nm is due to some absorption resonance inside the wetting layer. The solid black line is a mere guide to the eye and particularly down samples the range of 840 nm to 850 nm. The sample is not absorptive in this range, hence we do not expect any effect from the repump laser in reviving the QD transition.

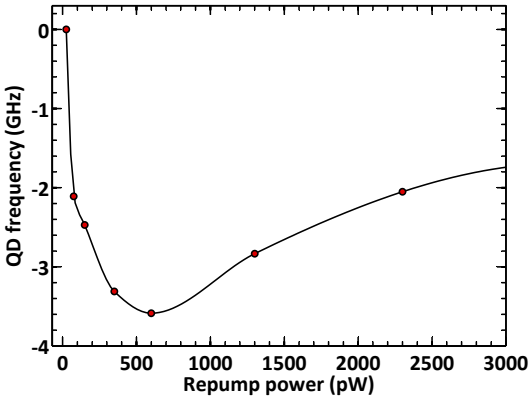

Figure 4.15: (a) Position of the transmission dip versus repump laser power. The resonant laser power corresponds to 8 pW. Solid black curve is guide to the eye. The transition of the QD first red-shifts with increasing repump laser power and then blue shifts.

these measurement.

4.4.5 Measurement of the ground state lifetime and revival time constant

As observed so far, the ground state of the exciton is a meta-stable state, either associated with the presence of certain charge configuration in traps around the QD or the presence of a single electron

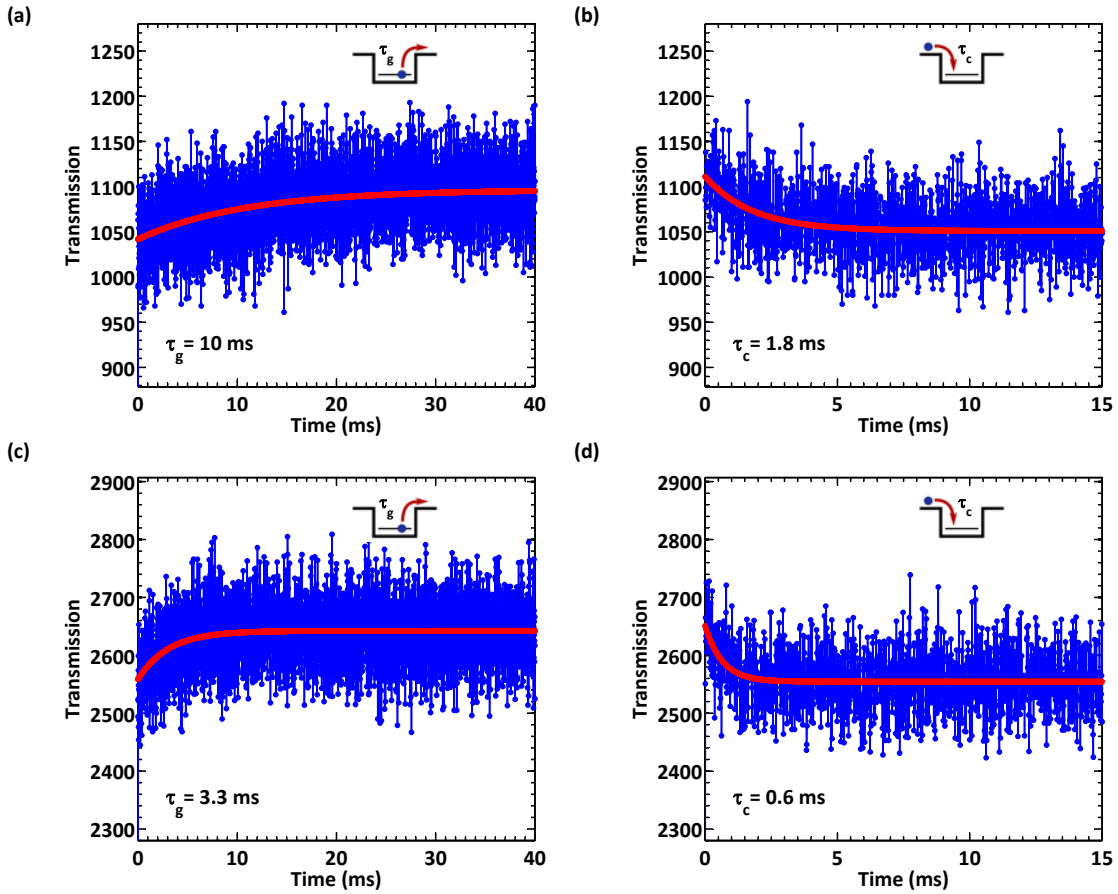

Figure 4.16: (a) Decay of the ground state to dark state as a function of time. At t=0 the repump laser is turned OFF and the change in transmission versus time is recorded. The procedure is repeated for several periods and the results are summed. (b) Revival of the ground state from dark state as a function of time. At t=0 the repump laser is turned on and again the change in transmission versus time is recorded. The solid red lines are single exponential fits to the data. From the fits in (a) and (b) we extract a ground state lifetime of 10 ms and a revival time constant of 1.8 ms. The intensity of the resonant laser and the repump laser are 6.2 pW and 500 pW respectively. The measurements in (c) and (d) are the same as (a) and (b) except for $P_{resonant} = 62$ pW and $P_{repump} = 1$ nW. In these cases τ_c and τ_g are extracted to be 3.3 ms and 0.66 ms.

inside the QD to form a charged exciton. In order to figure out the lifetime of this ground state and the time scales required for preparing the correct ground state, we monitor the transmission of the system versus time while toggling the repump laser ON and OFF at one Hertz. The resonant laser is tuned into the center of the transmission dip. Figures 4.18(a) and (c) show the time evolution of the transmission. The repump laser is initially ON for a long time and is turned OFF at time zero. The transmission of the waveguide appears to increase over time scale of τ_g. This time constant is the lifetime of the ground state of the QD. For the measurements in part (a) the intensity of the resonant laser and the repump laser are 6.2 pW and 500 pW respectively. From single exponential fit to the data in part (a), we extract a ground state lifetime of 10 ms for above specified powers. For the measurements in part (c), $P_{resonant} = 62$ pW and $P_{repump} = 1$ nW and we extract τ_g =3.3 ms. Figure

4.18(b) and (d) show the time evolution of the waveguide transmission during the ON period of the repump laser. At time zero, the repump laser is turned on after being OFF for 0.5 s. The transmission of the waveguide appears to drop with a time constant of τ_c. We attribute this time constant to the time it takes to revive the QD transition. The intensity of the repump and resonant laser in parts (b) and (d) correspond to the ones in (a) and (c) respectively. From single exponential fits to these curves, we extract τ_c to be 1.8 ms for part (b) and 0.6 ms for part (d).

4.4.6 Others efforts to increase the transmission dip contrast

We tried several methods to increase the contrast of the dip in the transmission spectrum of the system. In reference [152], it is shown that by decreasing the total measurement time, it is possible to obtain fourier transform limited transitions. However, this requires that the total measurement time is less than the time scale of the charge and spin noises in the environment. We believe that the dominant noise in our case is the charge noise, since the spin noise is independent of the sample [152] and has much lower amplitude than we observe. Hence, we tried to do the transmission scans in as short time scales as possible. However, the shortest time scales we achieved were around 0.2 s, which is much longer than the expected time scales.

Another factor limiting the transmission dip could be the phonon sideband of the QD transition. In order to check the influence of these sidebands, we filter the transmission using a monochromator setup with full-width half-maximum of 30 GHz. Figure 4.17(a) shows the transmitted photon flux after being filtered with the monochromator. The two slopes in this figure are due to sharp spectral response of the monochromator. Figure 4.17(b) shows the transmission spectrum corresponding to the part (a). The transmission spectrum in figure 4.17(b) is very similar to the one in 4.13(c). Therefore, we conclude that the phonon sidebands are not the limiting factor in our case.

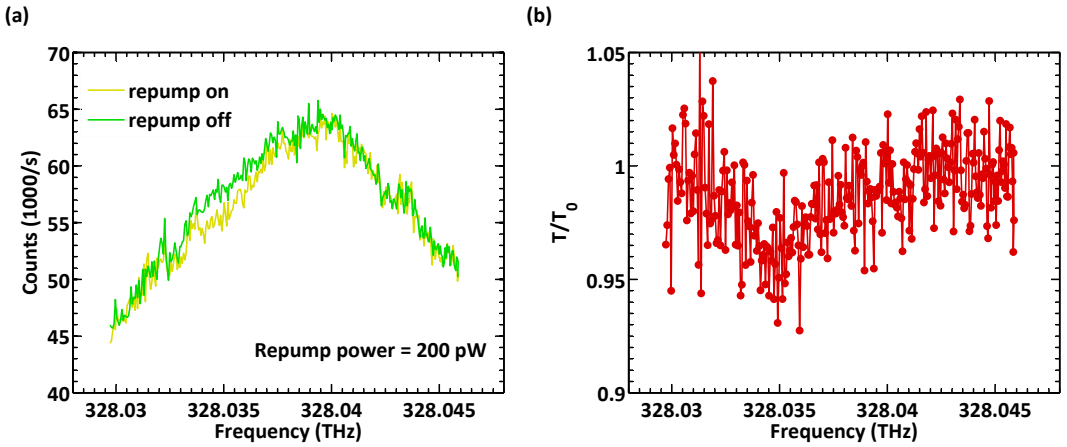

Figure 4.17: (a) the transmitted photon flux after being filtered with a monochromator. The resonant laser and repump laser intensities are $P_{resonant} = 4.17$ nW and $P_{repump} = 800$ pw. The slopes in plot are due to spectral response of the monochromator. (b) The transmission spectrum corresponding to(a). The transmission spectrum is very similar to the one in 4.13(c).

The oxides on the surfaces of the nanostructure could also be responsible for increasing the charge fluctuation in the environment since they act as active trap sites. We tried to etch away these oxides using a digital etching step. However, the band-edge of the PCW shifts to lower wavelengths after the digital etching step and the QD was not inside the primary band of the waveguide any more. In order to shift the waveguide mode back to the initial wavelength, we deposited HfO_2 on the sample using monolayer deposition techniques. Figure 4.18 shows the emission spectrum of the waveguide after the deposition. The band-edge of the waveguide is at the desired wavelength; however, the low power emission spectrum is significantly more polluted than before and high background emission can be seen in the emission spectrum. Also the single emitter lines are clearly broader than expected. We tried the same measurement as in the past, however we failed to see any resonant signal from the QD.

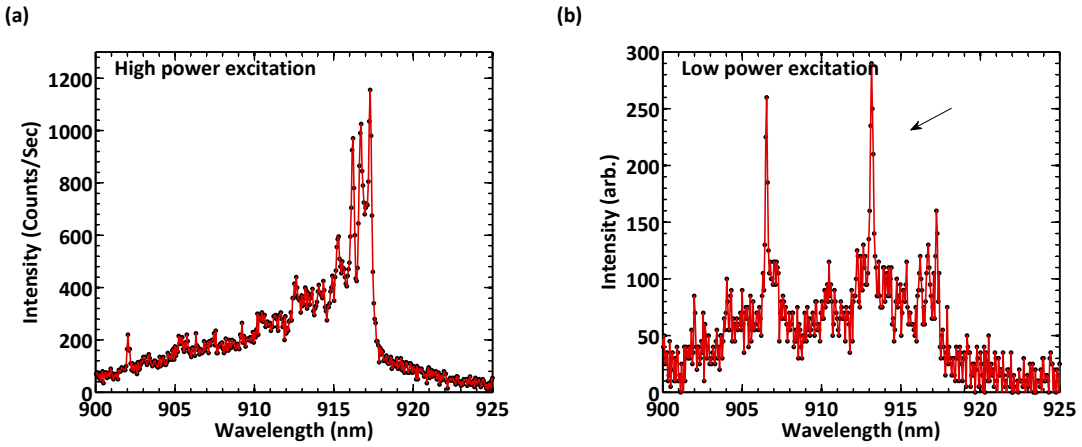

Figure 4.18: Emission spectrum of the sample after HfO_2 deposition, (a) under high-power excitation, and (b) under low-power excitation. The band-edge is approximately around the same wavelength it was before digital etching. The QD transitions are also around the same value as before. However, there is significant background emission, and the emission spectrum is much more polluted compared to the spectrum before the deposition, figure 4.7. Also, the emission peaks in part (b) are much wider than the peaks in figure 4.7.

We later fabricated 3 other samples and tried the resonant measurements on them. In the first fabrication run, the band-edge of the waveguides was outside the range of the available CW lasers. In the second run, the aboveband emission spectrum of the sample was much dimmer than the initial measurements in figure 4.7 and 4.9 indicating that something might be wrong with the piece of the QD wafer. The third sample was similar to the primary sample of these measurements and we tried the resonant measurements on 4 different waveguides in that sample; however, we did not get a resonant signal. Although the yield is low, this observation is not a surprise. The resonant scattering is known to be low-yield when there is no control over electrostatic environment of the QD (no electric contacts) [160] and references there.

4.5 Conclusions and outlook

In this chapter, we presented the experimental effort towards resonant scattering from InAs quantum dots in photonic-crystal waveguides. We designed a PCW structure composed of a slow light PCW which enables efficient light matter coupling, and two fast light PCWs that facilitate the light coupling and transport on the chip. We observed several different behaviors from QDs in our measurements. In the preliminary stage of the measurement, we observed excessive noise in the transmission spectrum of our waveguide which we attributed to the embedded emitters. We used a repump laser to activate the transitions of our QDs and we observed 3% dip in the transmission of our system on the first generation of samples. Later, We observed up to 30% contrast in the transmission spectrum of the sample with lower density of dots. The sample degradation was a serious problem during the course of the measurement. However, we were able to counter the degradation using different repump schemes. We also reported the behavior of the QD transition as a function of the repump power and wavelength. Finally, we studied time scales related to activation and deactivation of the QD transition as a result of applied repump laser.

The results reported in this chapter can be further improved in several ways. Firstly, a post processing step can be added to the measurement procedure. One possible implementation of the post processing step is as follows. The resonant laser intensity is increased to high levels over short time scales, $\approx 1\,\mu s$. The transmitted count rates are integrated in this window. Based on the count rates in this window one keeps or discards the measurement results in the subsequent window. Another possibility would be to resonantly characterize the sample and identify the QDs with reasonable resonant count rates and then build nanostructures around them. This could increase the chances of observing resonant signal from QDs in the nanostructures. Finally, implementing electric gates on the sample can allow one to apply an electric field across the QD layer. This electric field can help pin the charge state of the QD and also reduce the charge noise in the environment of the dot.

Chapter 5

Single-photon nonlinearity induced by a single quantum dot in a photonic-crystal waveguide: theory and experiment

This chapter partly builds on reference [183]. As mentioned and discussed in the earlier chapters, an efficiently coupled QD-PCW is a versatile platform for quantum optics at the fundamental photon levels. Optical nonlinearities at the single photon level, where one photon and two photons interact differently with the system, are one of the important blocks for classical and quantum information processing. In this chapter, we experimentally show that a single quantum dot can efficiently modulate transmission of a PCW and modify the photon statistics of the transmitted field. We measure the transmission spectrum of a PCW around the resonance frequency of a well-coupled QD and show that the QD induces a dip in the transmission spectrum of the PCW. We study the power dependence of the transmission dip and observe that the critical photon number for saturation of the transmission spectrum is below 1. The photon statistics of the transmitted field show a pronounced bunching of the photons as a result of the single photon components being preferentially reflected. The raw value of normalized autocorrelation around the zero delay time is 1.08 and we estimate it to be around 1.17 after deconvolution with the instrument response function of the setup.

The power dependence of the transmission, and also the bunching in the photon statistics of the transmitted field, indicate an optical nonlinearity at single photon level, and further highlight the potential of PCWs for quantum optical experiments and quantum information processing. Further work in the direction of these results would enable photon sorters, QND detectors, and single photon transistors.

5.1 Introduction and literature review

Nonlinear interaction between photons has far-reaching applications in classical and quantum information processing [14, 15]. However, optical interaction between photons is very weak and only observable at high intensities. Kerr type nonlinearities in bulk crystals occur at relatively high power scales. Nonlinearities originating from single atoms are also generally weak as result of the small optical cross section of the single emitters. One approach to increase the optical cross section of the atoms would be to use an ensemble of atoms. However, the number of photons required to saturate and ensemble of atoms increases with the number of atoms involved, hence limiting the efficiency of this approach [184]. Alternatively, one can focus the light beam using lenses with high numerical apertures and hence increase the emitter-field interaction. Pioneering work with different quantum emitters has already proven significantly enhanced nonlinear interaction mediated by atoms [185], quantum dots [147, 148] and dye molecules [186] in this configuration. Although this approach provides orders of magnitude enhancement compared to a nonlinear crystal, the photon-photon interaction is still weak for any application in quantum optics. Cavity quantum electrodynamics offers an alternative to achieve strong nonlinear interactions at the single photon level.

Single emitters efficiently coupled to localized cavity or single propagating modes exhibit photon level nonlinearities in their response [184]. A localized mode, a cavity or a waveguide mode, enhances the interaction time of the emitter and the photon and thereby increases the interaction strength. In the atomic optics community, several works with single atoms coupled to different types of cavities have already demonstrated nonlinear interactions at few photon levels [19, 21, 187, 188], also see recent review article [184]. Very recently, Tiecke *et al.* reported switching the phase of a light field based on internal state of an atom [20]. Excitingly, photon-photon switching at few photon level was reported in reference [189].

As discussed in chapter 3, engineered nanostructures enable efficient and deterministic interfacing of the quantum emitters. As a result, observation of optical nonlinearities on the single photon level is possible. There are several reports of optical nonlinearities at few-photon levels in the quantum dot community, with QDs strongly coupled to different cavities. Englund *et al.* reported optical nonlinearity in the few photon limit in the reflection spectrum of an strongly coupled QD-cavity system [166]. They used an L3 photonic crystal cavity with embedded quantum dots and achieved a contrast of 60% in the reflection spectrum of the cavity due to a strongly coupled quantum dot. They extracted the kink of the saturation to be around 0.5 photons inside the cavity which corresponded to 20 nW. Later, the same group studied the quantum nature of this nonlinearity by measuring the autocorrelation function of the reflected photons. They measured the $g^2(\tau)$ versus detuning of the excitation laser from the polariton peaks and observed photon bunching at the cavity frequency and anti bunching when on resonance with the polaritons line [168]. In a third publication from the same group, they reported switching of the reflection of the system [190], where switching of the phase of the reflected field was achieved with around 5 intra-cavity photons.

Around the same time Srinavasan *et al.* reported the nonlinear response of a strongly coupled QD-microdisk cavity [167]. Their system was composed of a fiber side coupled to a microdisk cavity.

They measured the transmission and reflection of the fiber as a function of excitation wavelength and QD-cavity detuning. They observed around 35% contrast in the transmission of the system and the kink of the saturation around 0.1 pW.

Other groups also reported few photon level nonlinearities and optical switching with strongly coupled QD-cavities. Reinhard *et al.* studied the photon statistics of a strongly coupled QD- L3 cavity. They used a procedure to position the quantum dots deterministically in the antinode of the cavity and they could obtain a coherent coupling strength of 141 µeV [169]. They observed $g^{(2)}(0) = 1.5$ in resonance with the bare cavity peak and $g^{(2)}(0) = 0.55$ at resonance with the polariton peaks. In a later work, the group demonstrated fast photon switching using the same system [191]. Nonlinear behavior of quantum dots strongly coupled to micropillar cavities has also been studied [170, 192]. Loo *et al.* also reported few photon level nonlinearity in transmission spectrum of a strongly coupled QD-micropillar cavity. They observed a 25% contrast in the reflection of the cavity and a critical intra-cavity photon number of 0.03 corresponding to 8 photons on the sample per pulse where the pulse width was on the order of the cavity life time [170]. Around the same time two other groups demonstrated optical switching using L3 cavities strongly coupled to a QD [193, 194]. Kim *et al.* demonstrated switching of the polarization of an optical field based on the internal state of a QD. They used the V system resulting from two dipoles of a neutral QD. One of the two dipoles ($|1\rangle$) was in strong coupling with the cavity while the other one ($|2\rangle$) was decoupled from the cavity. They controlled the polaritons of the $|1\rangle$-cavity by optically driving the $|2\rangle$ transition, and hence obtained switching.

All the nonlinearities reported in the quantum photonic community are with QD strongly coupled to nanocavities. However, the main requirement for strong nonlinearities is a highly efficient interaction between the light field and a single quantum emitter. As discussed in chapter 3 nanostructures can provide efficient interface to the coupled emitters in the Purcell regime of QED. Accordingly, a single emitter can offer strong nonlinearities without the need for strong coupling with a cavity [16, 21, 188]. Several groups in the atomic optics community have very recently demonstrated such a possibility [20, 21, 188]. In this respect quantum dots embedded in photonic crystals are ideal candidates since the high coupling efficiency between a PCW and the embedded QDs for a very broad bandwidth has already been demonstrated, see chapter 3 and the references in there.

The main advantage a waveguide over a cavity is its broad bandwidth and true on-chip operation. A long cavity lifetime (large Q-factor and small linewidth) is the main requirement for achieving strong coupling between a QD and a cavity. However, such systems require a mechanism to tune the QD to the resonance of the cavity. More importantly, high Q-factor cavities in general have a non-Gaussian far-field with multiple side peaks [120]. The particular far-field pattern makes these cavities hard to interface efficiently with a fiber. Side coupling these cavities to an on-chip waveguide is either not efficient, or results in significant reduction in the Q-factor of the cavity. On the contrary, a system like a PCW, in addition to being an efficient interface to the QD, allows for direct scaling of the system without the need to couple the light out of the chip. Even the detection can be done on-chip using integrated superconducting detectors [177].

In this chapter, we demonstrate a giant optical nonlinearity in a PCW. The nonlinear behavior is resulting from saturation of a QD coupled to the PCW with high efficiency. The next section starts with a simple description of light scattering from an atom well-coupled to a single mode and then gives exact formulas for a real emitter in a PCW, including residual reflections from different parts of the PCW and effects like spectral diffusion of the QD.

5.2 Theoretical background

In this section, we theoretically analyze the transmission of a single mode efficiently coupled to a single quantum emitter. We refer to the quantum emitter as QD and the 1D system as PCW hereafter, since these terms are more relevant for the experimental work presented in this chapter; however, the results are general and apply to any emitter coupled to a 1D-like system.

From classical scattering problem, it is known that the electric field in a homogenous medium with a single polarizable object can be written as a sum of the incident field and the field scattered from the object [105, 195].

$$\hat{\mathrm{E}}_{\mathrm{Total}} = \hat{\mathrm{E}}_{\mathrm{incident}} + \hat{\mathrm{E}}_{\mathrm{scattered}}, \tag{5.1}$$

where $\hat{\mathrm{E}}_{\mathrm{Total}}$ is the total field in the medium, $\hat{\mathrm{E}}_{\mathrm{incident}}$ is the field applied to the medium, and $\hat{\mathrm{E}}_{\mathrm{scattered}}$ is the field scattered by the object.

For a QD sitting at $x = 0$, the coherent part of the scattered electric field is related to the expectation value of the atomic operator $s_- = |g\rangle\langle e|$ as [103, 196]:

$$\hat{\mathrm{E}}_{\mathrm{QD}} = i\sqrt{\frac{\Gamma}{2}}\langle s_-\rangle \left(\hat{\mathrm{E}}_{\mathrm{PCW}}(-k,x)\Theta(-x) + \hat{\mathrm{E}}_{\mathrm{PCW}}(k,x)\Theta(x)\right), \tag{5.2}$$

where the Θ is the heaviside function, $\hat{\mathrm{E}}_{\mathrm{PCW}}$ is the eigenmode of the waveguide, and first term is the field scattered to the left side of the QD and the second term is the field scattered to the right side of the QD and Γ is the decay rate of the emitter. Note that the scattered field is $\pi/2$ out of phase with the $\langle s_-\rangle$.

The general equations for $\langle s_-\rangle$ under resonant excitation can be found in any quantum optics textbook, see for example [103, 197]. One can easily get the formula for a QD in a 1D system, see first part of this section or reference [196] for an exact derivation. In the weak excitation regime from one side of the PCW, as in section 5.1, $\langle s_-\rangle$ is equal to:

$$\langle s_-\rangle = i\sqrt{\frac{2}{\Gamma}}E_{\mathrm{incident}}, \tag{5.3}$$

where E_{incident} is the amplitude of the field incident on the QD from the left side of the PCW. As clear from the equation 5.1 and equation 5.4, the field scattered from the QD in the weak excitation regime is π out of phase with the excitation filed. Hence, the two fields interfere destructively in the forward direction, and the field intensity on the right hand side of the QD is zero, as pictured in figure 5.1(a).

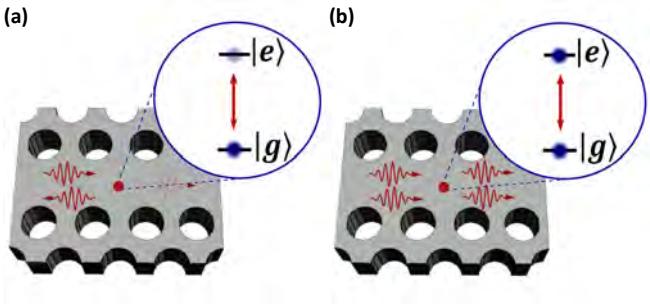

Figure 5.1: (a) At low excitation powers the scattering from the QD is coherent. The photon scattered in the forward direction and the incident photon interfere destructively and cancel out, hence the transmission probability of the photon vanishes in the ideal case. (b) When several photons interact with the QD at the same time, the QD saturates and the multi-photon components have a higher probability of being transmitted.

In the strong driving limit, the QD is saturated by the incident field. In this regime, $\langle s_- \rangle$ is proportional to $\frac{i}{E^2_{\text{incident}}}$. This term vanishes in the strong excitation limit, hence all the field incident on the QD is transmitted, as depicted in figure 5.1(b). In the quantum picture, this saturation already happens for the 2 photon components of the field and the two photon components have a higher probability of being transmitted [181]. Therefore, the saturation of the QD combined with its efficient coupling to the PCW provides an optical nonlinearity at the single photon level.

In the following subsections we derive theoretical formulas to model dynamics of photon scattering off a QD in a PCW. We start with the Hamiltonian for a QD coupled to a single mode and derive the formulas for the transmission coefficient of the QD-PCW system. We later study the quantum effects that stem from the photon nonlinearity of the system.

5.2.1 Full equations for the transmission coefficient

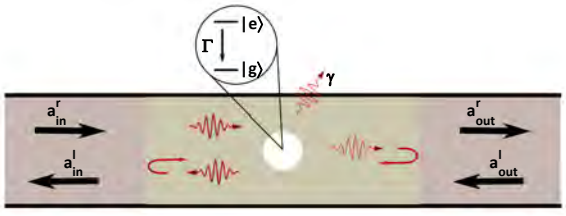

Figure 5.2: A pictorial demonstration of different effects present when a QD is coupled to the propagating mode of a waveguide. There are reflections between different sections of the waveguide that give rise to Fabry-Perot resonances in the waveguide. The emission from the QD also couples to radiation modes with a decay rate of γ. The model for this system is equivalent to the case of a double sided cavity coupled to propagating modes of an ideal waveguide. The left hand side of the waveguide is the input port and the right hand side is the output port.

In this section we study the transmission coefficient of a PCW with a QD efficiently coupled to

it. Figure 5.2 shows the physical picture of the system. A QD in a PCW has several decay channels other than the PCW mode, leaky modes discussed in chapter 3. The coupling to these modes is modeled with their decay rate γ. Also, there are always residual reflections between different sections of a PCW. This situation is very similar to the case of a QD inside a double-sided cavity efficiently coupled to a waveguide on the two ends. We model the effect of these residual reflections through the quality factor of the cavity (Q)[1].

The Hamiltonian of the system can be written as:

$$H = \hbar\omega_0 \hat{s}_z + \hbar(\omega_0 + \delta)\hat{a}^\dagger \hat{a} + i\hbar g(\hat{s}_-^\dagger \hat{a} - \hat{a}^\dagger \hat{s}_-), \tag{5.4}$$

where the first two terms are the energy of atom and the cavity, and the last two terms model the interaction of the QD and the cavity, and g is the coupling strength between the cavity and the QD.

In figure 5.2, a_{out}^r and a_{out}^l are the right and left propagating fields in the output port (right hand side of figure 5.2), and a_{in}^r and a_{in}^l are the right and left propagating fields in the input port (left hand side of figure 5.2). We assume that the system is excited from the left hand side ($a_{\text{out}}^l = 0$). We treat the excitation laser as a classical field and include it in the equations by the field amplitude. As described before the total field in the system can be written as a sum of the incident field (a_{in}^r) and the field scattered from the cavity[2]. That is:

$$\begin{aligned} a_{\text{out}}^r &= i\sqrt{\kappa}\langle\hat{a}\rangle, \\ a_{\text{in}}^l &= a_{\text{in}}^r + i\sqrt{\kappa}\langle\hat{a}\rangle, \end{aligned} \tag{5.5}$$

where κ is the decay rate of the cavity to the waveguide. The Heisenberg equations of motion for the cavity and the atom can be written as:

$$\begin{aligned} \dot{\hat{s}}_- &= i\Delta\omega \hat{s}_- - 2g s_z \hat{a} - \frac{1}{2}(\gamma + 2\gamma_0)\hat{s}_- + G, \\ \dot{\hat{s}}_z &= g(\hat{s}_-^\dagger \hat{a} + \hat{a}^\dagger \hat{s}_-) - \gamma(\hat{s}_z + \frac{1}{2}) + K, \\ \dot{\hat{a}} &= -i(-\Delta\omega + \delta)\hat{a} - \kappa\hat{a} - g\hat{s}_- + i\sqrt{\kappa}a_{\text{in}}^r + H \end{aligned} \tag{5.6}$$

where γ is the decay rate of the emitter to the leaky modes, $\Delta\omega = \omega - \omega_0$ is the detuning between the excitation laser and the QD [3], and γ_0 is the pure dephasing rate of the emitter. For our system, the QD-cavity coupling is in the Purcell regime, that is $\kappa >> g$ (also referred to as bad cavity limit [182]). In this limit, the cavity field can be assumed to be in a stationary state ($\dot{\hat{a}} = 0$). Substituting this to equations in 5.6, one can simplify the equations of motion for the expectation values of atomic operators as:

$$\begin{aligned} \dot{s}_- &= i\Delta\omega s_- - \frac{\Gamma_{\text{WG}}}{2}\left(\frac{1}{f} + t_0\right)s_- - 2i\Omega t_0 s_z, \\ \dot{s}_z &= -\Gamma_{\text{WG}}\left(\text{Re}\,(t_0) + \frac{\gamma}{\Gamma_{\text{WG}}}\right)(s_z + 1) + i\left(\Omega t_0 s_-^* - c.c.\right), \end{aligned} \tag{5.7}$$

[1] This section benefits from the work in reference [196]. However, for most equations in the article, pure dephasing is neglected. In addition, the reference mainly extracts the coherent component of the transmitted field. Moreover we study the quantum statistical properties of the transmission.

[2] Note that for a cavity embedded in a waveguide, if the cavity is removed, the incident light is reflected back.

[3] The definition of $\Delta\omega$ is different from reference [196] by a minus sign.

with

$$\begin{aligned} f &= \frac{\Gamma_{\mathrm{WG}}}{2\gamma_0+\gamma}, \\ t_0 &= \frac{1}{1+\frac{i(\delta-\Delta\omega)}{\kappa}}. \end{aligned} \tag{5.8}$$

where we have used $s_z = \langle \hat{s}_z \rangle$ and $s_- = \langle \hat{s}_- \rangle$. $\Gamma_{\mathrm{WG}} = \frac{2g^2}{\kappa}$ is the decay rate of the QD to the waveguide mode, and $\Omega = a_{\mathrm{in}}^r \sqrt{\Gamma_{\mathrm{WG}}/2}$ is the Rabi frequency of the input field.

The steady-state solution of the equations of motion can be readily derived [196]:

$$\begin{aligned} s_- &= -\frac{4}{\Gamma_{\mathrm{WG}}} \frac{i\Omega t_0 s_z}{t_0 + \frac{\gamma}{\Gamma_{\mathrm{WG}}} + \frac{2\gamma 0}{\Gamma_{\mathrm{WG}}} - \frac{2i\Delta\omega}{\Gamma_{\mathrm{WG}}}}, \\ s_z &= \frac{-0.5}{1+\Omega^2/\Omega_c^2}. \end{aligned} \tag{5.9}$$

where

$$\Omega_c^2 = \frac{|2i\Delta\omega - (\gamma + t_0\Gamma_{\mathrm{WG}} + 2\gamma_0)|^2 \left[\gamma + \Gamma_{\mathrm{WG}} \,\mathrm{Re}(t_0)\right]}{8|t_0|^2[\gamma + 2\gamma_0 + \Gamma_{\mathrm{WG}} \,\mathrm{Re}(t_0)]}. \tag{5.10}$$

is the critical Rabi frequency and corresponds to $s_z = -\frac{1}{4}$. For the purpose of evaluating the nonlinearity in terms of the number of input photons, it is instructive to define a parameter $n_\tau = 2\frac{\Omega^2}{\Gamma^2}$. This parameter corresponds to the mean photon flux in the input field per lifetime of the emitter. The critical photon number can then be define as $n_c = 2(\frac{\Omega}{\Gamma})^2$. For a QD in resonance with the cavity and $\Delta\omega = 0$, the critical photon number is:

$$n_c = \frac{(1 + 2\beta\frac{\gamma_0}{\Gamma})}{4\beta^2}. \tag{5.11}$$

where $\beta = \frac{\Gamma_{\mathrm{WG}}}{\gamma+\Gamma_{\mathrm{WG}}}$ is the collection efficiency of the photons scattered from the QD, as defined and discussed in chapter 3. The critical excitation power P_c corresponds to $\hbar\omega n_c\Gamma$. The transmission and reflection coefficients of the field can be extracted as:

$$\begin{aligned} t &= \frac{\langle a_{\mathrm{out}}^r \rangle}{a_{\mathrm{in}}^r}, \\ r &= \frac{\langle a_{\mathrm{in}}^l \rangle}{a_{\mathrm{in}}^r}. \end{aligned} \tag{5.12}$$

The transmission coefficient of the system under the assumption $\Delta\omega = 0$ and $\delta = 0$ can be simplified to:

$$t = 1 - \frac{\Gamma\beta}{(\Gamma + 2\gamma_0\beta)(1 + n_\tau/n_c)}. \tag{5.13}$$

It is instructive to plot the transmission of the system versus power and detuning. Figure 5.3(a) shows transmissions of the QD-PCW system versus excitation power and the detuning from the QD, while $Q = 1000$, $\beta = 0.96$ and $\delta = 200$ GHz. Figure 5.3(b) shows the transmission of the waveguide versus detuning from the QD at low excitation powers. A peak and a dip are visible in the transmission around the resonance of the QD. The dip is a result of coherent reflection of the incident photons by the QD transition as discussed so far. The peak, however, is a result of interference between the light scattered from the QD and the light scattered from the cavity [180]. The Fano-resonance between the light scattered from the QD and the cavity scattering induces a transparency window. In this window, the transmission of the system is higher than transmission of the bare cavity [198]. Figure 5.3(c) shows transmissions of the system versus excitation power when at resonance with the QD

frequency. The transmission of the system is inhibited by the QD at low excitation powers. As also seen from equation 5.13, the transmission of the system ($|t|^2$) has a quadratic power law dependence and pronounced saturation is seen while increasing the excitation power.

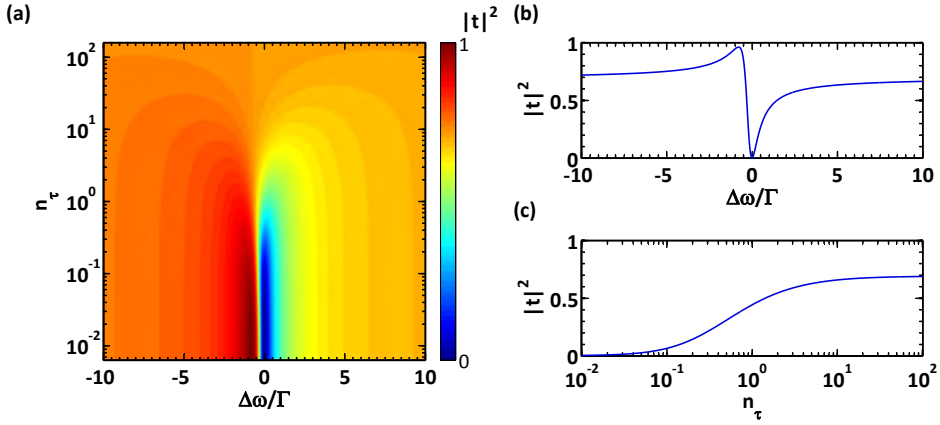

Figure 5.3: (a) The transmission of the PCW-QD system versus power and detuning from the QD. (b) The transmission of the system in the very weak input power regime. The peak in the transmission is a result of Fano-resonance between the cavity and the QD, where QD opens a transmission channel. (c) Transmission of the system versus excitation power on resonance with the QD ($\Delta\omega = 0$). The parameters used for these plots are $Q = 1000$, $\beta = 0.96$ and $\delta = 200$ GHz.

Note that equations 5.12 are only valid for the coherent part of the transmitted field. The coherent part of the transmission is the relevant quantity when doing homodyne measurements. For the photon counting measurements, as in this thesis, the measured transmission of the system is the total transmitted field, which is a sum of coherent and incoherent parts. The incoherent component of the scattering from the QD can be extracted as:

$$\frac{P_{\text{incoh}}}{a_{\text{in}}^{r\,2}} = 1 - \left(|t|^2 + |r|^2 + \gamma|\langle s\rangle|^2/a_{\text{in}}^{r\,2}\right). \tag{5.14}$$

and the total transmission can be evaluated as:

$$T = |t|^2 + \beta P_{\text{incoh}}/2a_{\text{in}}^{r\,2}. \tag{5.15}$$

Figure 5.4(a) shows the coherent and incoherent components of the transmitted field and the coherent component of the reflection versus excitation power. The parameters used for this plot are $Q = 1000$, $\beta = 0.96$ and $\delta = 0$. The system with these parameters constitutes a nearly ideal system. Most of the light transmitted at low excitation powers appears to be incoherent; however, the higher power transmission appears to be totally coherent. Also, most of the reflection at low power excitation appears to be coherent with the incident laser. Part (b) of this figure shows the total transmission of the system and the coherent transmission of the system. The total transmission of the system has a linear power law dependence at low powers, typical of a single emitter.

Finally, the transmission spectrum of the system can be reconstructed as:

$$\frac{T}{T_0} = \frac{T}{t_0^2}. \tag{5.16}$$

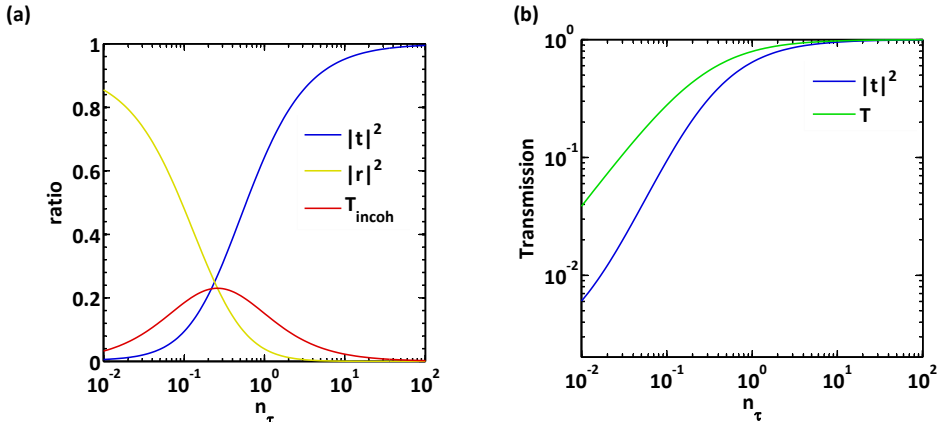

Figure 5.4: (a) The coherent transmission (blue), incoherent transmission (red), and the coherent component of the reflection of the QD-PCW system versus resonant power for a nearly ideal system. At the low power regime most of the transmission is incoherent, since the parameters in this mode are close to a nearly ideal system and most of the incident field is coherently reflected. At higher powers the transmission is mostly coherent. Also note that $R_{\text{incoh}} = T_{\text{incoh}}$ (b) The total transmission of the system (green) and the coherent component of the transmission (blue) versus resonant power. The parameters used for these plots are $Q = 1000$, $\beta = 0.96$ and $\delta = 0$.

This equation is the most relevant equation for modeling the experimental data. The optical nonlinearity discussed so far also has implications for the statistics of the transmitted photons. In the next section, we present a theoretical models to compute $g^{(2)}(\tau)$ of the transmitted light.

5.2.2 Autocorrelation function of the transmission

The quantum nature of the light is presented in its photon statistics. The easiest method to experimentally characterize a light field is to measure the correlation on the arrival times of its photons ($G^{(2)}(\tau)$) [103].

$$G^{(2)}(\tau) = \langle \hat{a}^\dagger(0) a^\dagger(\tau) a(\tau) a(0) \rangle. \tag{5.17}$$

In our case we, we are mostly interested in the statistics of the transmitted field. The $G^{(2)}(\tau)$ for the transmitted field can be written as:

$$\begin{aligned} G^{(2)}(\tau) = \langle & \left(t_0 a_{\text{in}}^r - i\sqrt{\frac{\Gamma_{\text{WG}}}{2}} t_0 \hat{s}_-^*(0) \right) \left(t_0 a_{\text{in}}^r - i\sqrt{\frac{\Gamma_{\text{WG}}}{2}} t_0 \hat{s}_-^*(\tau) \right) \times \\ & \left(t_0 a_{\text{in}}^r + i\sqrt{\frac{\Gamma_{\text{WG}}}{2}} t_0 \hat{s}_-(\tau) \right) \left(t_0 a_{\text{in}}^r + i\sqrt{\frac{\Gamma_{\text{WG}}}{2}} t_0 \hat{s}_-(0) \right) \rangle. \end{aligned} \tag{5.18}$$

As discussed in the previous chapter, in the final stage of the measurement, the QD of interest was close to resonance with the cavity. For the simplicity we set $t_0 = 1$ and $\delta = 0$ here on. Under these

assumptions the $G^{(2)}(\tau)$ can be simplified as:

$$\begin{aligned} G^{(2)}(\tau) =& {a_{\text{in}}^r}^4 - 4\sqrt{\frac{\Gamma_{\text{WG}}}{2}}{a_{\text{in}}^r}^3 \operatorname{Im}\left[\langle \hat{s}_-(0)\rangle\right] + \Gamma_{\text{WG}}{a_{\text{in}}^r}^2\left(\frac{1}{2} + \langle \hat{s}_z(0)\rangle\right) + \\ & \Gamma_{\text{WG}}{a_{\text{in}}^r}^2 \operatorname{Re}\left[\langle \hat{s}_-^\dagger(0)\hat{s}_-(\tau) - \hat{s}_-^\dagger(0)\hat{s}_-(\tau)^\dagger\rangle\right] + \Gamma_{\text{WG}}\sqrt{\frac{\Gamma_{\text{WG}}}{2}}a_{\text{in}}^r \operatorname{Im}\left[\langle \hat{s}_-^\dagger(0)\hat{s}_z(\tau)\rangle\right] \\ & - \frac{\Gamma_{\text{WG}}}{2}\sqrt{\frac{\Gamma_{\text{WG}}}{2}}a_{\text{in}}^r \operatorname{Im}\left[\langle \hat{s}_-(0)\rangle\right] + \Gamma_{\text{WG}}\sqrt{\frac{\Gamma_{\text{WG}}}{2}}a_{\text{in}}^r \operatorname{Im}\left[\langle \hat{s}_-^\dagger(0)\hat{s}_-^\dagger(\tau)\hat{s}_-(0)\rangle\right] + \\ & (\frac{\Gamma_{\text{WG}}}{2})^2\langle \hat{s}_-^\dagger(0)\hat{s}_z(\tau)^\dagger\hat{s}_-(0)\rangle + \frac{1}{2}(\frac{\Gamma_{\text{WG}}}{2})^2\left(\frac{1}{2} + \hat{s}_z(0)\right). \end{aligned} \tag{5.19}$$

The normalized auto correlation function $g^{(2)}(\tau)$ can be written as:

$$g^{(2)}(\tau) = \frac{G^{(2)}(\tau)}{\langle\left(a_{\text{in}}^r - i\sqrt{\frac{\Gamma_{\text{WG}}}{2}}\hat{s}^*(\tau)\right)\left(a_{\text{in}}^r + i\sqrt{\frac{\Gamma_{\text{WG}}}{2}}\hat{s}(\tau)\right)\rangle^2} \tag{5.20}$$

In order to calculate $g^{(2)}(\tau)$, one needs to apply the quantum regression theorem [103] to the equations in 5.7 and get the equations governing the two time ($\langle \hat{s}_i(0)\hat{s}_j(\tau)\rangle$) and three time averages ($\langle \hat{s}_i(0)\hat{s}_j(\tau)\hat{s}_k(0)\rangle$) in equation 5.20. In both cases, the resulting equations are of the form $\langle \dot{\hat{S}}\rangle = M\langle \hat{S}\rangle + D$. For the two time averages these have the following form

$$\begin{aligned} \frac{d}{d\tau}\langle \dot{\hat{S}}\rangle &= \begin{bmatrix} \langle \hat{s}_-^\dagger(0)\hat{s}_-^\dagger(\tau)\rangle \\ \langle \hat{s}_-^\dagger(0)\hat{s}^(\tau)\rangle \\ \langle \hat{s}_-^\dagger(0)\hat{s}_z(\tau)\rangle \end{bmatrix}, \qquad M = \begin{bmatrix} -i\Delta\omega - f_1 & 0 & 2i\Omega \\ 0 & i\Delta\omega - f_1 & -2i\Omega \\ i\Omega & -i\Omega & \gamma + \Gamma_{\text{WG}} \end{bmatrix} \\ D &= \begin{bmatrix} 0 \\ 0 \\ -0.5(\gamma + \Gamma_{\text{WG}})s_-^* \end{bmatrix}, \qquad f_1 = \gamma/2 + \gamma_0 + \Gamma_{\text{WG}}/2. \end{aligned} \tag{5.21}$$

For the three time averages, the matrix M is the same as above. The other two vectors are:

$$\frac{d}{dt}\langle \dot{\hat{S}}\rangle = \begin{bmatrix} \langle \hat{s}_-^\dagger(0)\hat{s}_-^\dagger(\tau)\hat{s}_-(0)\rangle \\ \langle \hat{s}_-^\dagger(0)\hat{s}^(\tau)\hat{s}_-(0)\rangle \\ \langle \hat{s}_-^\dagger(0)\hat{s}_z(\tau)\hat{s}_-(0)\rangle \end{bmatrix}, \qquad D = \begin{bmatrix} 0 \\ 0 \\ -0.5(\gamma + \Gamma_{\text{WG}})(0.5 + s_z) \end{bmatrix}. \tag{5.22}$$

These equations can be solved analytically only in the very simple cases, e.g. $\Delta\omega = 0$ or $\tau = 0$ [16, 181, 182]. However, the analysis in this thesis require the $g^{(2)}(\tau)$ versus detuning and power. Hence, we revert to solving these equations numerically.

Figure 5.5(a) shows the time dependence of the autocorrelation function versus different values of γ_0. For this plot, we use $n_\tau = 0.06$ and $\beta = 0.96$. The strong bunching around zero time delay is a consequence of the saturation of the emitter when excited with multiple photons. Physically it can be interpreted as follows: when single photons arrive at the emitter one by one (weak excitation), they are coherently reflected by the emitter. When two photons arrive at the emitter with relatively short delays, the QD is saturated and both photons have a higher probability of being transmitted as opposed to the single photons [181]. Therefore, detection of a photon increases the probability of detecting a second photon in short time delays afterwards. Figure 5.5(b) shows the behavior of the $g^{(2)}(0)$ as a function of the n_τ for different values of β. When β is high (relevant for blue and green

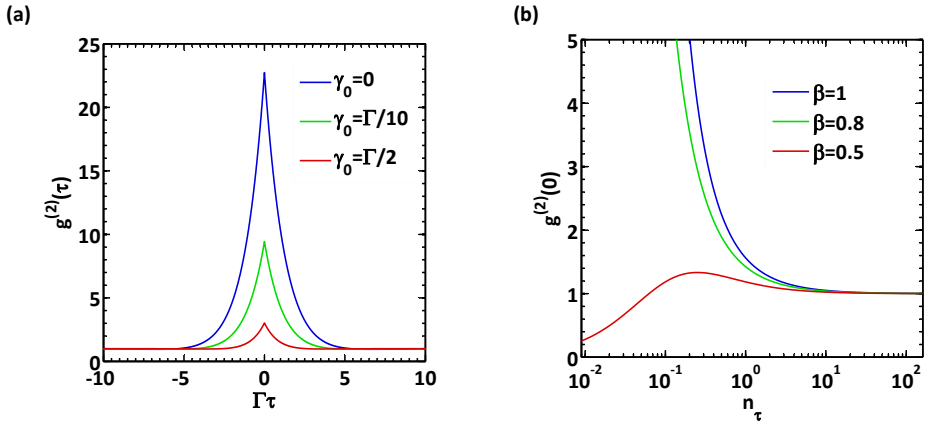

Figure 5.5: (a) $g^{(2)}(\tau)$ versus time for different values of γ_0. The main feature of the $g^{(2)}(\tau)$ is the bunching of the photons around the $\tau = 0$. This is a direct consequence of the nonlinear transmission of the system. For this plot, we use the parameters $\beta = 0.96$ and $n_\tau = 0.06$. (b) The $g^{(2)}(0)$ versus excitation power for different values of β and $\gamma_0 = 0.5\Gamma$. The bunching of the photons decreases as the excitation power increases as a direct consequence of the saturation of the emitter.

curves), the transmission probability of single photon components increases with increasing n_τ, hence $g^{(2)}(0)$ approaches one. When β is around 0.5, the auto correlation function of the field has different behavior. For $\beta = 0.5$, there is a pronounced anti-bunching of the photons at low excitation powers, followed by a bunching at intermediate excitation powers.

Another phenomena relevant to the QDs is the spectral diffusion of the QD transition [152, 161], where the transition frequency of the emitter changes in time scales longer than the lifetime of the emitter. In the next section, we present the theoretical method to include effect of the spectral diffusion in the models presented so far.

5.2.3 Effect of spectral diffusion and blinking of the emitter

The energy of the s-shell transition of a QD is known to change over time scales much longer than the lifetime of the emitter mainly due to changes in the charge and spin configuration of the environment of the QD [152, 155, 166, 199]; these effects have been discussed in detail in previous chapter. As long as these shifts are within several linewidths of the emitter, the result is spectral broadening of the QD transition (referred to as spectral diffusion here on). When these shifts are much larger than the linewidth of the emitter the result is blinking of the QD transition.

The spectral diffusion can be modeled by including a random detuning in the transition frequency of the QD, that is $\omega = \omega_0 + \delta_0$ where ω_0 is the resonance frequency of the QD and δ_0 is a random variable with a Gaussian probability distribution:

$$P(\delta_0) = \frac{1}{\sqrt{2\pi\sigma^2}} e^{-\frac{\delta_0^2}{2\sigma^2}}. \tag{5.23}$$

In order to obtain the time averaged effect of these fluctuations on the transmitted light intensity and

its statistics, equations 5.16 and 5.20 have to be convoluted with equation 5.23:

$$T^* = \int_{-10\sigma}^{10\sigma} T(\Delta\omega - \delta_0) P(\delta_0)\, \mathrm{d}\delta_0 \tag{5.24}$$

$$g^{(2)*}(\tau) = \int_{-10\sigma}^{10\sigma} g^{(2)}(\tau, \Delta\omega - \delta_0) P(\delta_0)\, \mathrm{d}\delta_0. \tag{5.25}$$

On the other hand, the blinking of the QD can be characterized as the ratio between the time the QD spends in the dark state over the sum of the time spent in the bright and the dark states (α). The effect of blinking can be modeled as:

$$T_{\mathrm{exp}} = (1-\alpha)T^* + \alpha \times 1, \tag{5.26}$$

$$g^{(2)}_{\mathrm{exp}}(\tau) = (1-\alpha)g^{(2)*}(\tau) + \alpha \times 1. \tag{5.27}$$

Physically, these equations can be interpreted as follows: when the QD is in the dark state (with probability of α) the transmitted light is the coherent laser state and when the QD is in the bright state (with probability $(1-\alpha)$) the transmission spectrum and the $g^{(2)*}(\tau)$ are given by equations 5.24 and 5.25 [168,169]. Hence a weighted average of the two states gives the experimentally observed transmission spectrum and the $g^{(2)}(\tau)$.

In the next section, we present the experimental results where we show that giant optical nonlinearities are within reach with QDs efficiently coupled to PCWs.

5.3 Experimental demonstration

In this section, we present the experimental results, where we resonantly excite a QD which is efficiently coupled to a PCW. The sample used for the experiments is the same as the one in section 4.4. We start by shortly reviewing the structure of the sample and the preliminary measurements.

Figure 5.6(a) and (b) show the principle of operation of the nonlinearity and the structure of the sample. As evident from equation 5.13, high β- factor is beneficial for operation of nonlinearity on single photon levels. Therefore, we choose the quantum dots that are in the slow light section of the waveguide (central section of (a) and (b) of figure 5.6). As discussed in chapter 3, the β-factor in this region is close to unity. The green spot in the center of part (b) represents the repump laser. Figure 5.6(c) shows a SEM image of the three parts of the sample, the out-coupling grating, the slow light region, and the in-coupling grating.

Technical details of resonantly exciting the QD is covered in chapter 4. Part (d) of figure 5.6, shows the transmission spectrum of the waveguide around the resonance of the QD. The transmission of the waveguide is modulated by around 30% due to presence of the QD. The peak in the transmission spectrum is due to a Fano-resonance between the scattering from the QD and the scattering from the cavity, as discussed in section 5.6. The solid black line in part (d) is the fit using equation 5.26. We extract $\beta = 0.88$, $\Gamma = 4.6\,\mathrm{GHz}$ and $\sigma/\Gamma = 3$.

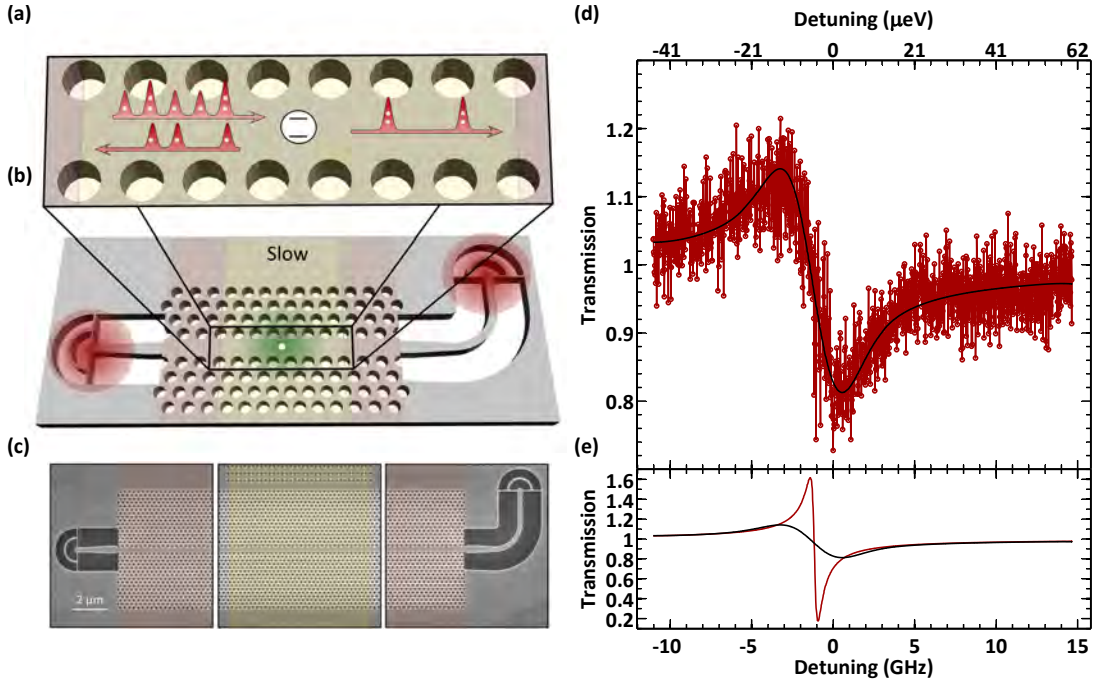

Figure 5.6: (a) Operational principle of resonant scattering with a single quantum dot in a photonic-crystal waveguide. We choose the quantum dots that are in the slow light waveguide. Due to the high β in the slow light section, most of the single photons are coherently reflected. (b) Pictorial sketch of the sample. As discussed in section 4.2.1, the structure of the sample allows the efficient in-coupling of the photons to the chip and subsequently to the slow light section. (c) An SEM image of the fabricated sample, showing the two out-coupling gratings and the slow light sections. (d) Transmission spectrum of the waveguide around the resonance of the QD. The excitation power was $\sim 50\,\mathrm{pW}$ on the sample. The transmission dip is a result of photons being reflected by the QD. The peak is due to a Fano-resonance between the QD and the cavity, as discussed earlier. The solid black line is the theoretical fit to the data from equation 5.26. From this fit, we extract $\beta = 0.88$, $\Gamma = 4.6\,\mathrm{GHz}$ and $\sigma/\Gamma = 3$. (e) The solid redline is the theoretically expected transmission of the PCW around the resonance of the QD, i.e. $\gamma_0 = 0$ and $\sigma = 0$. The solid black line is the fit from part (d).

The red curve in part (e) of figure 5.6 shows the transmission spectrum of the waveguide after deconvolution with the spectral diffusion of the QD. According to this plot, significant modification of the transmission spectrum can be achieved if the spectral diffusion of the QD is controlled. There are several methods to reduce and eliminate the spectral diffusion [152,155]. One method would be to implement electrical gates on the sample and pin down the Fermi-level across the QD layer [149,152]. Additionally, one can stabilize the transition of the QD using active feedback from the QD [154]. Another possibility could be to devise a post processing method and post select the results based on transmission of waveguide on time scales of microseconds, as described in the conclusion section of the chapter 4 (this method is very popular in atomic optics community, e.g. [20]). The results in parts (d) and (e) of figure 5.6 emphasize the exciting possibilities offered by PCWs for efficient light matter interfaces. In the next section we study the nonlinear behavior of the PCW transmission as a result of QD presence.

5.3.1 Nonlinear transmission of the photonic-crystal waveguide

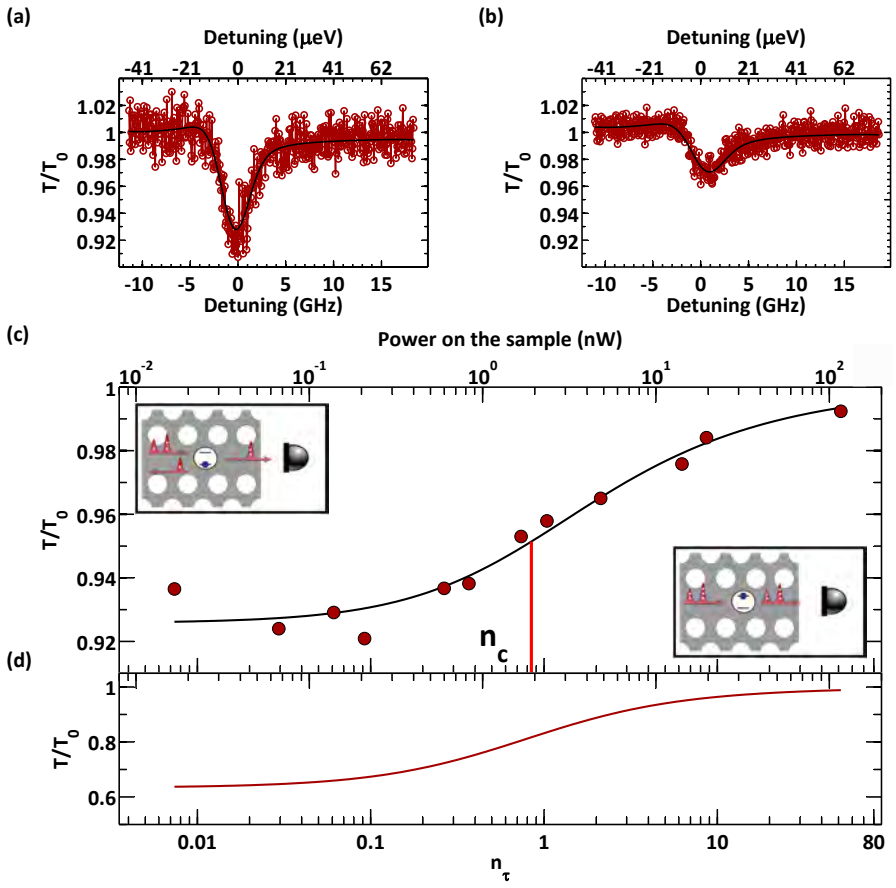

Figure 5.7: (a) Transmission spectrum of the waveguide while $n_\tau \sim 0.11$, and (b) $n_\tau \sim 1.3$. The solid black lines are fits using the equation 5.26. (c) Power dependence of the transmission dip. The bottom axis shows the average photon flux per lifetime of the emitter. The top axis shows the power incident on the sample. The solid black line is the theoretical model from equation 5.26. The n_c is indicated with a vertical red line. A strong saturation of the transmission is observed at high n_τ. (d) The theoretical fit from part (c) after deconvolution with the spectral diffusion of the QD.

In the later stages of the measurement the contrast in the transmission of the PCW decreased, most likely due to numerous cool-down and heat-up cycle, as discussed earlier in section 4.4.2. We measure the transmission of the waveguide versus resonant power to quantify the nonlinearity. The experimental setup is the same as section 4.2.2. We use APDs to quantify the transmission of the setup, therefore we detect the total transmission of the waveguide as opposed to homodyne type measurements which only probe the coherent part. Figure 5.7(a) and (b) show two sample transmission spectrums, corresponding to an excitation power of 0.12 nw and 2.2 nw, corresponding to weak and intermediate excitation powers respectively. Figure 5.7(c), shows the transmission dip versus n_τ. Three different regimes are visible: coherent scattering regime, incoherent scattering regime and saturation. At very low powers the value of the transmission dip is independent of the excitation power for over more than an order of magnitude. At higher powers the transmission is a sum of coherent and incoherent scattering with a linear power law dependence with a slope of one. At even

higher laser powers, the emitter is saturated and the transmission is dominated by the resonant laser and reaches the steady value of one. Solid black line is the theoretical model from equation 5.26. This fit is obtained by recursively fitting the data in this plot and the $g^{(2)}(0)$ which follow later in this chapter. The full fitting procedure is described in appendix C. From these fits we extract $n_c = 0.81$. The other parameters are extracted to be $\gamma_0/\Gamma = 0.79$, $\beta = 0.88$, $\sigma/\Gamma = 3.6$, and $\alpha = 0.4$. Part (c) of the figure, shows the power dependence of the transmission dip as a function of excitation power after deconvolution with spectral diffusion of the QD. The power incident on the sample and the extracted n_τ are different by a factor of three which implies that the in-coupling efficiency of the photons is around 23%. Next, we study the photon statistics of the transmitted field and its behavior versus resonant laser power.

5.3.2 The photon statistics of the transmitted field

In order to further confirm the low power optical nonlinearity, we do autocorrelation measurements on the transmitted field. The autocorrelation measurement allows us to probe photon statistics of the transmitted field. The configuration of the setup is discussed in chapter 4. Briefly, the CW resonant laser is tuned into the transmission dip, and locked to a high precision wavemeter. The collected light from the out-coupler is coupled to a single mode fiber and then split in to two with a fiber-beamsplitter and sent to two fiber coupled APDs. We look at the time delay between detection events on the APDs.

Figure 5.8(a) and (b) show the raw autocorrelation histograms for two different excitation powers, roughly corresponding to the ones in figure 5.7(a) and (b) respectively. We observe the expected bunching of the photons around zero time delay. The strong bunching around zero delay times indicates lack of single photon component in the transmitted light as predicted by theory. In order to sanity check the measurements, we detuned the resonant laser far from the transmission dip and repeated the measurement. As a second check we turned off the repump laser. Both cases produced a flat $g^{(2)}(\tau)$ as expected.

Figure 5.8(c) shows the power dependence of the $g^{(2)}(0)$. The value of the $g^{(2)}(0)$ decreases with the increasing excitation power as a result of the saturation of the QD. The solid black line is the theoretically predicted values, based on the parameters $\gamma_0/\Gamma = 0.79$, $\beta = 0.88$ and $\sigma/\Gamma = 3.6$. As discussed in the previous section these parameters are extracted from a recursive fit of data in figure 5.7(c) and figure 5.8(c). The fitting procedure is described in appendix C. We estimate a critical photon number of ($n_c = 0.81$), which corresponds to 1.9 nW on the sample. Figure 5.8(d) shows the theoretical model when we set the spectral diffusion of the QD to zero. This plot further demonstrates the potential of the efficiently coupled QD-PCW as a light-matter interface at fundamental limits of light intensities, at the single photon level.

Another factor limiting the observed bunching in $g^{(2)}(0)$, is the instrument response function of the measurement setup. Figure 5.8(a) shows the IRF of the setup for autocorrelation measurements. This IRF is extracted by sending 5 ps pluses through the setup and recording the autocorrelation function of the collected light. The fullwidth at half maximum of the IRF curve is around 0.5 ns, very

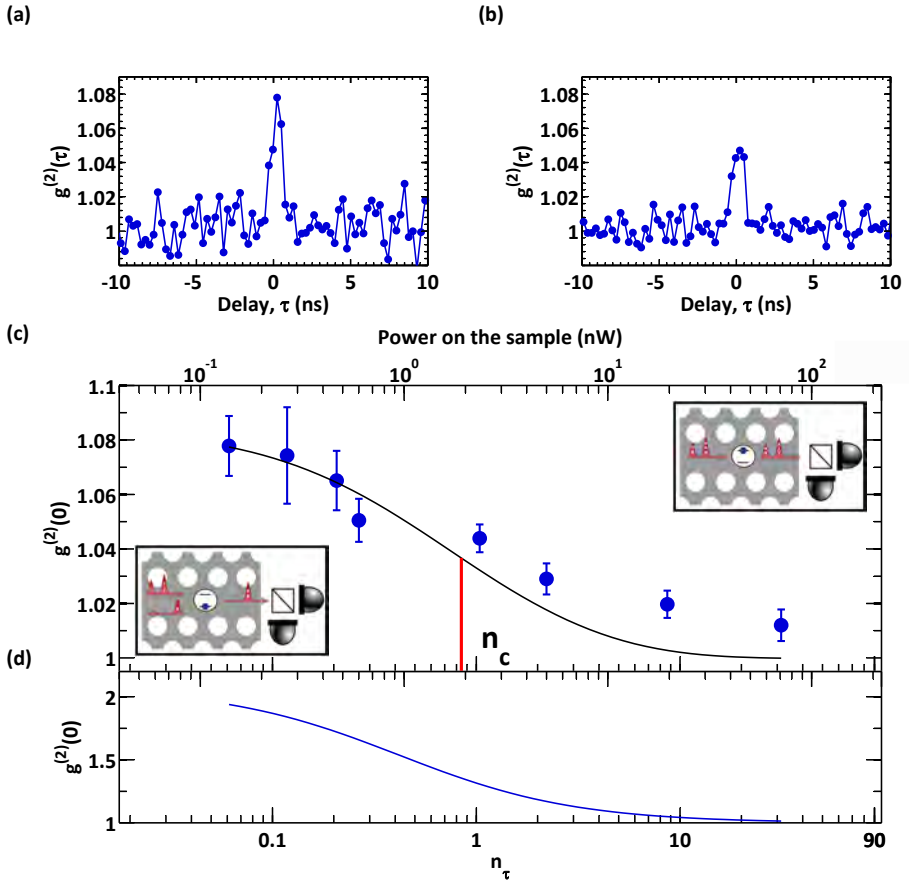

Figure 5.8: (a) and (b), Sample autocorrelation histograms of the transmitted field for the powers corresponding to the ones in figure 5.7(a) and (b) respectively. The bunching around zero time delay is a direct consequence of elimination of the single photon components. (c) Power dependence of the $g^{(2)}(0)$. The bottom axis shows the average photon flux per lifetime of the emitter. The top axis shows the power incident on the sample. The solid black line is the theoretical model from equation 5.27. The n_c is indicated with a vertical red line. A strong saturation of the transmission is observed at high n_τ. (d) The theoretical fit from part (c) after deconvolution with the spectral diffusion of the QD.

close to the lifetime of the QD (0.4 ns). Figure 5.8(b) is $g^{(2)}(0)$ after deconvolution with the IRF of the setup. We plot the fit in 5.8(c) while setting the IRF of the setup to a delta function. The IRF of the setup appears to be limiting the observed bunching $(g^{(2)}(0) - 1)$ by a factor of more than 2 when in the low power regime.

The power dependence of the transmission of the waveguide, along with the antibunching in the autocorrelation measurements, confirm an optical nonlinearity at single photon level. Such a nonlinearity may find applications in classical optical and quantum optical computing. For instance, in the classical regime, one maybe able to build few photon switches that can outperform the electronic transistors for classical computing [200]. In the quantum regime, the observed nonlinearity can be used for quantum demolition photon number detection [26,201], along with nonclassical squeezed state

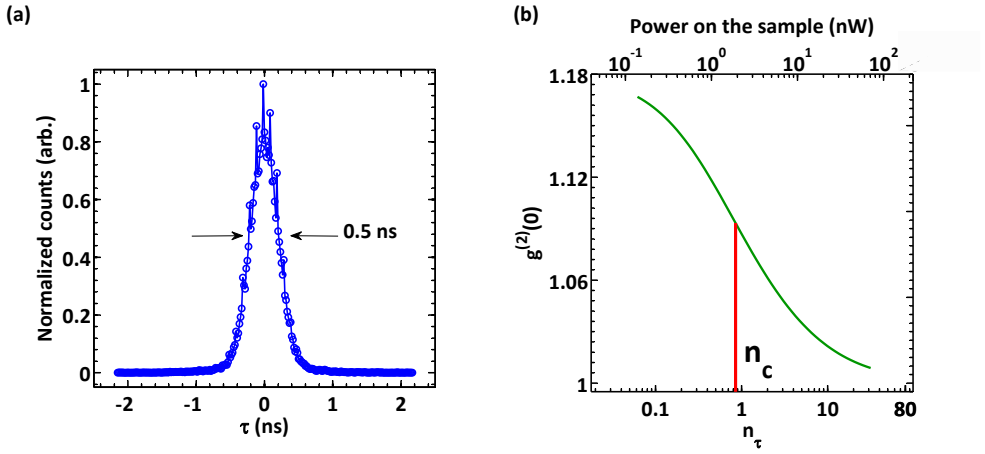

Figure 5.9: (a) Instrument response function of the setup for autocorrelation measurements. The fullwidth at half maximum of the IRF is 0.5 ns, mainly limited by the time response of the APDs. (b) The $g^{(2)}(0)$ as a function of power, after deconvolution of the IRF. This curve is obtained by evaluating the fit in 5.8(c) and setting the IRF to be a Dirac function.

generation [16, 202], and photon sorting based on the number of photons in the field [26].

5.4 Conclusions and outlook

The resonant excitation of single emitters coupled to broadband structures like waveguides paves the way towards many exciting experiments in quantum optics. In this chapter, we studied the transmission of a photonic-crystal waveguide, with a quantum dot efficiently coupled to it. Close to resonance of a efficiently coupled QD, we observed contrasts of up to 30% in the transmission of the waveguide. We observed Fano-resonances between the reflections in waveguide interfaces and the QD, which indicated coherent scattering from the QD. The transmission spectrum of the waveguide versus laser power, showed a pronounced saturation at very low photon intensities, 1.9 nW. Significant photon bunching in the statistics of the transmitted field confirmed that the single photon components had been eliminated. We measured a $g^{(2)}(0) = 1.08$, which was limited by the IRF of the measurement; we estimate that it is around 1.17 after deconvolution with the IRF. Autocorrelation measurements further confirmed the single photon level nature of the nonlinearity and coherence of the scattering from the QD.

These experimental results confirm a giant optical nonlinearity at single photon levels. A natural next step would be to do homodyne type measurements on the transmitted field. This would allow translating the nonlinearity in the photon intensity to nonlinear phase shifts and polarization switching. Additionally, using a magnetic field perpendicular to the sample will sperate the two dipoles of the charged exciton and form a lambda system. Such a system opens up the route towards single photon transistors and Bell-state analyzers [16, 26, 203–205].

Appendix A

Convergence analysis of the height of the active boundary conditions

One of the important parameters in calculations in section 3.5 is the height of the active boundary conditions. Figure A.1 shows the x component of the Poynting's vector (S_x) for 3 different boundary heights at z =0.6 µm. The common feature centered at $x = 0$ is due to coupling to the radiation modes from the dipole emitter. The power flows outwards from the dipole into the right and left. However, in figure A.1(a), where the boundary height is very low, the power is flowing in to the simulation domain from the two ends of the simulation domain, hence the sign of the S_x. This means that the size of the active boundaries is not tall enough and results in excess reflections. Nevertheless, increasing the height of the active boundaries reduces the power reflected from the right and left boundaries. Figures A.1(b) and (c) show S_x for h_{bnd} =360 nm and h_{bnd} =560 nm. The power reflected from the two boundaries appears to be decreasing with increasing height of the active boundaries.

Figure A.2 shows the dependence of the γ_{rad} on the height of the active boundaries for the x- and y-oriented dipoles. The simulation domain is $33a$ long. The dipoles are located at the antinode of E_y and the frequency corresponds to $N_g = 58$. γ_{rad} for the x-oriented dipole (red line in figure A.2) is rather independent of the height of the active boundaries, consistent with the fact that the antinode of E_y overlaps with the node of E_x and hence the dipole does not couple to the waveguide mode. The blue curve in figure A.2 shows the dependence of γ_{rad} for the y-oriented dipole. The γ_{rad} decreases with increasing h_{bnd} till around h_{bnd} = 400 nm and stays almost constant with further increase in h_{bnd}. For the simulations in section 3.5.2 the height of the active boundaries was chosen to be 500 nm.

APPENDIX A. CONVERGENCE ANALYSIS OF THE HEIGHT OF THE ACTIVE BOUNDARY CONDITIONS

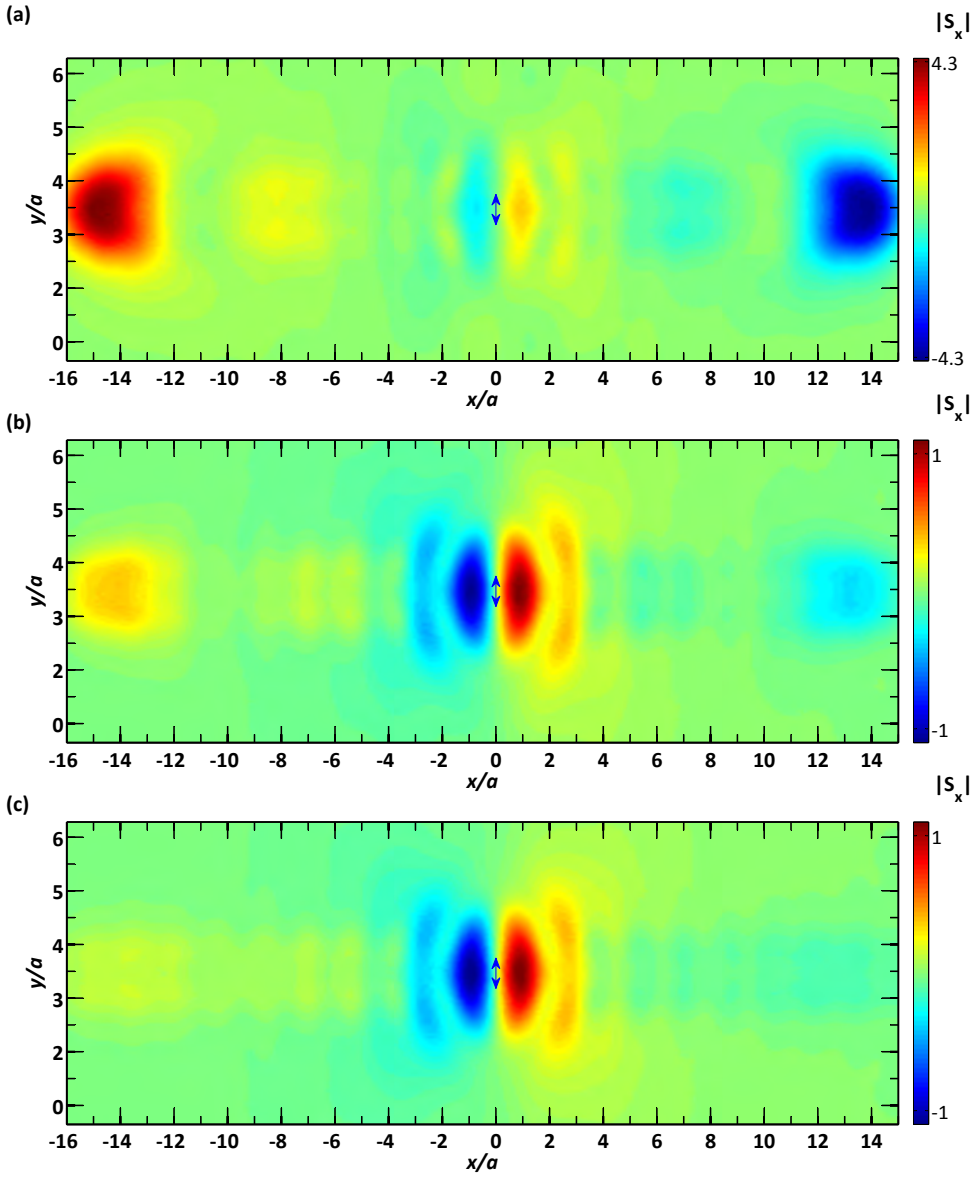

Figure A.1: x component of Poynting's vector at $z = 600$ nm for three different height of active boundaries. (a) $h_{bnd} = 200$ nm, (b) $h_{bnd} = 360$ nm, and (c) $h_{bnd} = 560$ nm.

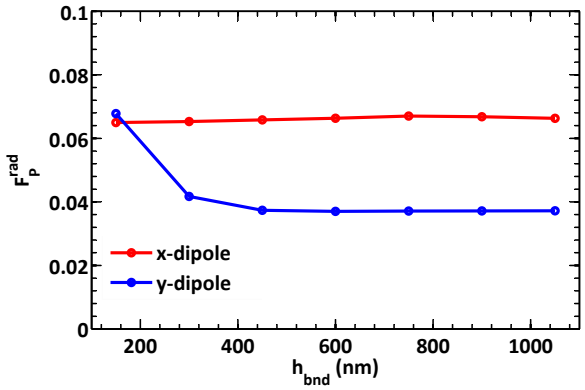

Figure A.2: Dependence of the γ_{rad} on the height of the active boundaries for x- and y- oriented dipoles located in the anti node of E_y at $N_g = 58$. γ_{rad} for the y-dipole becomes independent of the height of the active boundaries for $h_{bnd} > 450$ nm.

Appendix B

Mesh convergence tests

Meshing the simulation geometry can affect convergence of the simulation results significantly. The COMSOL package has very efficient methods to generate meshes of varying size depending on the geometric features of the simulation domain. However, certain guidelines are helpful for adapting the mesh to the requirements of LDOS and far-field calculations.

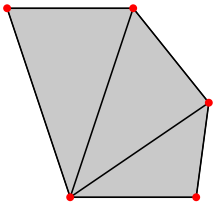

Figure B.1: A 2D mesh showing three triangular elements. The red dots are the mesh nodes.

We use the 2D mesh in figure B.1 to explain a few simple terms about meshing FEM domains before we proceed with the rest of this appendix. Note that all the simulations done in this thesis are 3D, however, meshing concepts are similar in 2D and 3D cases. A simulation domain is divided to mesh elements of different size and possibly geometry. Each red dot in figure B.1 is called a node and each of the triangles is called a mesh element. The mesh in figure B.1 is composed of three triangular mesh elements and 5 mesh nodes.

When meshing a structure, COMSOL uses the maximum allowed size of elements as the user control parameter. That means one can limit the maximum distance between the mesh nodes as an input parameter to the meshing algorithm. It is important to note that the software calls this parameter "Maximum element size". However, this is a misnomer and can lead to confusions, since a mesh element is a surface in 2D case, and a volume in 3D case.

Figure B.2 shows the cut through of a sample mesh in the center of membrane. The cyan region on the left side of the figure B.2(a) is used for eigenvalue calculation. The eigenvalue calculation domain has the identical mesh as the two ends of the waveguide (the cyan regions on two ends of the

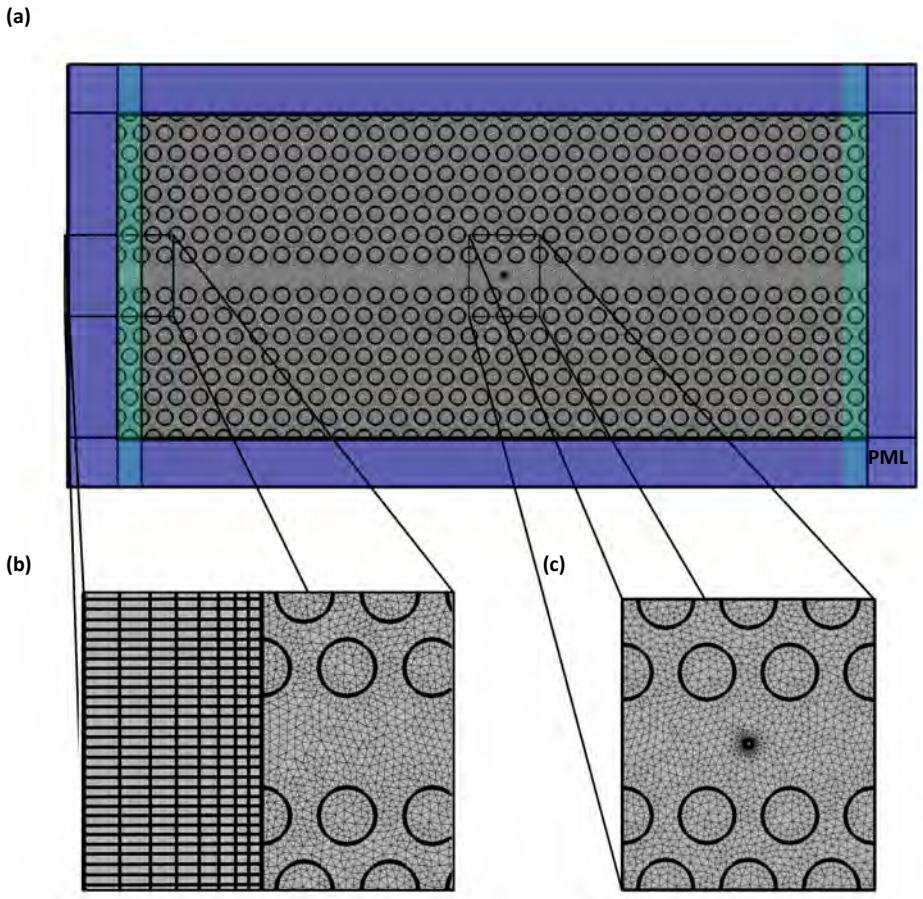

Figure B.2: A cut through of simulation domain with the respective mesh at $z = 0$. The cyan region on the left shows the unit cells used for eigenvalue calculation. The blue regions are the PMLs.

figure B.2(a)). This removes any need for interpolation of results between the simulation domains and improves the accuracy of the simulations. The mesh in the PML is direct translation of the mesh in the boundary of the PML domain. We use very fine meshing around the emitter and inside the box surrounding the emitter to assure that the dipole emitter is well resolved.

The maximum mesh element size in the membrane and also inside the air holes is l_0/n, where n is the refractive index of the material. The mesh size inside the box surrounding the emitter is 10 times finer than this value. The mesh element size in the air domain is set to l_0. The suggestion from the software is to use at least 5 mesh elements per wavelength in material of interest for accuracy of simulation results. However, different simulations have different requirement and different sensitivities to mesh element size at different regions of simulation domain. For most of the simulations we use $l_0 = \lambda/11$. In order to assure that the results are independent of the mesh parameter, we studied the dependence of $\gamma_{\mathrm{box}}/\gamma_{\mathrm{rad}}$ on the value of maximum mesh element size . Table B.1 presents the results from this study. The data shows that the value of control variable changes less than 0.5% with doubling the mesh element size. Based on this, we conclude that the simulations are insensitive to

the mesh element size.

Table B.1: Dependence of $\gamma_{\text{box}}/\gamma_{\text{rad}}$ on the mesh element size.

Maximum element size (nm)	150	120	100	90	80
$\gamma_{\text{box}}/\gamma_{\text{rad}}$	1.0016	1.0022	1.0009	1.0025	1

We run these simulations on a machine with 256 GB of memory, and 4 cpus each with 4 cores. Typically, with mesh elements of 100 nm and simulation domain length of $33a$, the total number of degrees of freedom is around 20 million. It takes 1 hour to get the electric field and LDOS for one dipole. We use the general residual method solver (GMRES) to diagonalize the resulting matrices. We use the multifrontal massively parallel solver (MUMPS), on a coarse mesh, to obtain a preconditioning for the matrices.

Appendix C

Procedure for modeling the experimental data in chapter 5

The experimental data in figures 5.7(a) and (b) is modeled using equation 5.26 and the resulting fits are shown as solid black lines in the respective figures. In this section, we explain how we arrived at these fits. The 5 parameters that govern the nonlinear response of the system are Γ, β, σ, α and γ_0. In the fits, we additionally have a sixth parameter A_0, which is a scaling factor that relates the power incident on the sample to the photon flux at the position of the QD. It includes all the factors relating to the in-coupling of the resonant laser and its propagation to the position of the QD.

from independent time-resolved measurements, we extract a QD decay rate of $\Gamma = 2.6\,\mathrm{ns}^{-1}$. This brings us down to 5 fit parameters, one of which is the scaling factor for the incident power, A_0. The scaling factor is defined as $\langle n \rangle = A_0 P_{\mathrm{input}}$, where P_{input} is the power measured on the sample in units of nano Watts. From equation 5.13, it is clear that the transmission of the waveguide is independent of the power for excitation powers much lower than the critical power, and thus the fit becomes independent of the scaling factor at these powers. Therefore, we fit the transmission spectra recorded at very low resonant power, the four points in the right hand side of the figure 5.7(c), using the 4 remaining fit parameters. We extract an average value of ($\beta = 0.85 \pm 0.18$) from these fits. Figure 5.7(a), shows one of these transmission measurements at very low powers along with the theoretical fit. From this fit, we get ($\beta = 0.84 \pm 0.22$), $\sigma/\Gamma = 2.65 \pm 0.9$, $\gamma_0/\Gamma = 0.63 \pm 1.4$, and $\alpha = 0.5 \pm 0.07$. Note that we can also fit the same curve with three parameters ($\beta = 0.82 \pm 0.20$), $\sigma/\Gamma = 3.35 \pm 0.2$, and $\alpha = 0.5 \pm 0.07$, which indicates that it is not possible to separate the contribution of γ_0 and σ from just the transmission curves.

While A_0 is guaranteed to remain fixed over the entire range of resonant powers investigated in figure 5.7(c) and figure 5.8(c), we expect the spectral diffusion and the pure-dephasing to vary. This is partly due to the fact that we have to change the power of the repump laser as we increase the resonant laser power. We fix the value of β and α extracted from the above fit and only use the

extracted values for σ and γ_0 as our starting guess. Next, we recursively fit the data in figure 5.7(c) and figure 5.8(c), with the three remaining parameters, σ, γ_0 and A_0. This we do in the following way: we start with a guess for γ_0 and fit the data in figure 5.7(c) and extract σ and A_0. We then fit the data in figure 5.7(c) with γ_0 as fitting parameter, while using σ and A_0 extracted in the previous step. Next, we use the value of γ_0 from the last step and redo the fits for σ and A_0. We repeat this process until a steady state for the values of γ_0, σ, and A_0 is reached. Later, we also fit the individual transmission curves versus power, using the value of A_0 and extract an α for each data point. We then average the value of α and feed it back to the recursive fitting routine. We find that the value of α changes between 0.25 and 0.5 for different curves. From the recursive fits, we extract $\gamma_0/\Gamma = 0.79 \pm 0.23$, $\sigma/\Gamma = 3.6 \pm 0.45$, $A_0 = 1.84 \times 10^7 \pm 40\%$, and $\alpha = 0.4$. We note that the values for the spectral diffusion and pure-dephasing extracted in this way should be thought of as an average value over the investigated power range. The final fits are shown as black curves in figure 5.7(c) and figure 5.8(c).

The fit in figure 5.6(d) was also obtained using equation 5.24, however, this measurement was taken in the short period before the sample degraded and unfortunately we cannot take advantage of the same type of detailed study of the power dependence and the decay rate to analyze this measurement. From this fit we obtain $\Gamma = 4.8\,\mathrm{ns}^{-1}$, $\beta = 0.88$ and $\sigma/\Gamma = 3$.

It is worth mentioning that it is possible to fit the power dependence of the transmission and $g^{(2)}(0)$ curves with either only dephasing or diffusion, while setting the other one to zero. However, it is not possible to consistently fit the power dependence of transmission and power dependence of $g^{(2)}(0)$ with only dephasing or only diffusion. Figure C.1 shows the result of recursively fitting the data in figure 5.7(c) and 5.8(c) with two parameters γ_0 and A_0. The fit to the experimental data is very poor.

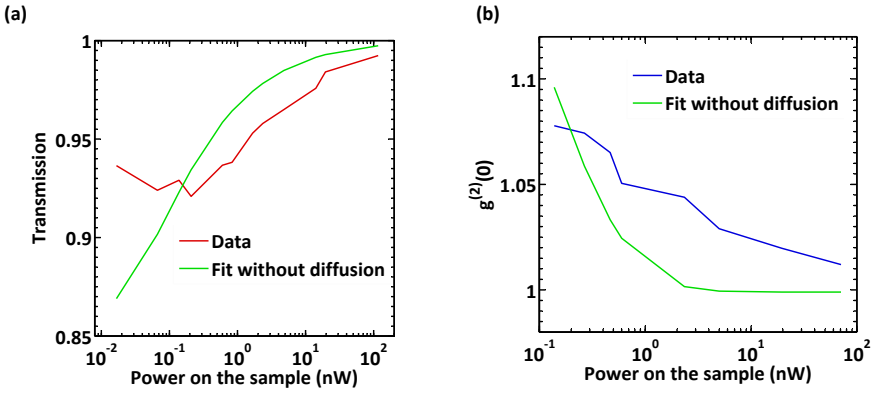

Figure C.1: The theoretical modeling of the experimental data without diffusion. (a) the transmission of the waveguide and the closest fit. (b) $g^{(2)}(0)$ and the closest fit.

Bibliography

[1] B. A. Joyce, P. C. Kelires, A. G. Naumovets and D. D. Vvedensky. *Quantum dots: fundamentals, applications, and frontiers* (Springer, 2005).

[2] P. Harrison. *Quantum wells, wires and dots: theoretical and computational physics of semiconductor nanostructures* (John Wiley & Sons, 2005).

[3] P. Michler. *Single semiconductor quantum dots* (Springer, 2009).

[4] M. Bayer, G. Ortner, O. Stern, A. Kuther, A. A. Gorbunov, A. Forchel, P. Hawrylak, S. Fafard, K. Hinzer, T. L. Reinecke, S. N. Walck, J. P. Reithmaier, F. Klopf and F. Schäfer. *Fine structure of neutral and charged excitons in self-assembled In(Ga)As/(Al)GaAs quantum dots.* Phys. Rev. B **65**, 195315 (2002).

[5] A. Vamivakas and M. Atatüre. *Photons and (artificial) atoms: an overview of optical spectroscopy techniques on quantum dots.* Contemp. Phys. **51**, 17 (2010).

[6] A. V. Khaetskii and Y. V. Nazarov. *Spin–flip transitions between Zeeman sublevels in semiconductor quantum dots.* Phys. Rev. B **64**, 125316 (2001).

[7] J. Johansen, B. Julsgaard, S. Stobbe, J. M. Hvam and P. Lodahl. *Probing long-lived dark excitons in self-assembled quantum dots.* Phys. Rev. B **81**, 081304(R) (2010).

[8] J. Dreiser, M. Atatüre, C. Galland, T. Müller, A. Badolato and A. Imamoglu. *Optical investigations of quantum dot spin dynamics as a function of external electric and magnetic fields.* Phys. Rev. B **77**, 075317 (2008).

[9] B. Urbaszek, X. Marie, T. Amand, O. Krebs, P. Voisin, P. Maletinsky, A. Högele and A. Imamoglu. *Nuclear spin physics in quantum dots: An optical investigation.* Rev. Mod. Phys. **85**, 79 (2013).

[10] E. Yablonovitch. *Inhibited spontaneous emission in solid-state physics and electronics.* Phys. Rev. Lett. **58**, 2059 (1987).

[11] S. John. *Strong localization of photons in certain disordered dielectric superlattices.* Phys. Rev. Lett. **58**, 2486 (1987).

[12] J. D. Joannopoulos, S. G. Johnson, J. N. Winn and R. D. Meade. *Photonic Crystals: Molding the Flow of Light* (Princeton University Press, 2008).

[13] M. A. Nielsen and I. L. Chuang. *Quantum computation and quantum information* (Cambridge university press, 2010).

[14] L. M. Duan and H. J. Kimble. *Scalable Photonic Quantum Computation through Cavity-Assisted Interactions*. Phys. Rev. Lett. **92**, 127902 (2004).

[15] H. J. Kimble. *The quantum internet*. Nature **453**, 1023 (2008).

[16] D. E. Chang, A. S. Sørensen, E. A. Demler and M. D. Lukin. *A single-photon transistor using nanoscale surface plasmons*. Nat. Phys. **3**, 807 (2007).

[17] H. J. Kimble. *Strong Interactions of Single Atoms and Photons in Cavity QED*. Phys. Scripta **T76**, 127 (1998).

[18] O. Astafiev, A. M. Zagoskin, A. Abdumalikov, Y. A. Pashkin, T. Yamamoto, K. Inomata, Y. Nakamura and J. Tsai. *Resonance fluorescence of a single artificial atom*. Science **327**, 840 (2010).

[19] K. M. Birnbaum, A. Boca, R. Miller, A. D. Boozer, T. E. Northup and H. J. Kimble. *Photon blockade in an optical cavity with one trapped atom*. Nature **436**, 87 (2005).

[20] T. Tiecke, J. Thompson, N. de Leon, L. Liu, V. Vuletić and M. Lukin. *Nanophotonic quantum phase switch with a single atom*. Nature **508**, 241 (2014).

[21] A. Goban, C.-L. Hung, S.-P. Yu, J. Hood, J. Muniz, J. Lee, M. Martin, A. McClung, K. Choi, D. Chang, O. Painter and H. Kimble. *Atom–light interactions in photonic crystals*. Nat. Commun. **5** (2014).

[22] T. Lund-Hansen, S. Stobbe, B. Julsgaard, H. Thyrrestrup, T. Sünner, M. Kamp, A. Forchel and P. Lodahl. *Experimental realization of highly efficient broadband coupling of single quantum dots to a photonic crystal waveguide*. Phys. Rev. Lett. **101**, 113903 (2008).

[23] M. Arcari, I. Söllner, A. Javadi, S. Lindskov Hansen, S. Mahmoodian, J. Liu, H. Thyrrestrup, E. H. Lee, J. D. Song, S. Stobbe and P. Lodahl. *Near-Unity Coupling Efficiency of a Quantum Emitter to a Photonic Crystal Waveguide*. Phys. Rev. Lett. **113**, 093603 (2014).

[24] J. Claudon, J. Bleuse, N. S. Malik, M. Bazin, P. Jaffrennou, N. Gregersen, C. Sauvan, P. Lalanne and J.-M. Gérard. *A highly efficient single-photon source based on a quantum dot in a photonic nanowire*. Nat. Photonics **4**, 174 (2010).

[25] S. Kumar, A. Huck and U. L. Andersen. *Efficient Coupling of a Single Diamond Solor Center to Propagating Plasmonic Gap Modes*. Nano Lett. **13**, 1221 (2013).

[26] D. Witthaut, M. D. Lukin and A. S. Sørensen. *Photon sorters and QND detectors using single photon emitters*. Europhys. Lett. **97**, 50007 (2012).

[27] A. Javadi, S. Maibom, L. Sapienza, H. Thyrrestrup, P. D. García and P. Lodahl. *Statistical measurements of quantum emitters coupled to Anderson-localized modes in disordered photonic-crystal waveguides*. Opt. Express **22**, 30992 (2014).

[28] K. Sakoda. *Optical properties of photonic crystals*, volume 80 (Springer, 2005).

[29] E. Istrate and E. Sargent. *Photonic crystal heterostructures and interfaces.* Rev. Mod. Phys. **78**, 455 (2006).

[30] P. Lodahl, S. Mahmoodian and S. Stobbe. *Interfacing single photons and single quantum dots with photonic nanostructures.* arXiv:1312.1079 (2013).

[31] Y. Lai, S. Pirotta, G. Urbinati, D. Gerace, M. Minkov, V. Savona, A. Badolato and M. Galli. *Genetically designed L3 photonic crystal nanocavities with measured quality factor exceeding one million.* Appl. Phys. Lett. **104**, 241101 (2014).

[32] J. Leuthold, C. Koos and W. Freude. *Nonlinear silicon photonics.* Nat. Photonics **4**, 535 (2010).

[33] K. Nozaki, T. Tanabe, A. Shinya, S. Matsuo, T. Sato, H. Taniyama and M. Notomi. *Sub-femtojoule all-optical switching using a photonic-crystal nanocavity.* Nat. Photonics **4**, 477 (2010).

[34] P. Lodahl, A. F. van Driel, I. S. Nikolaev, A. Irman, K. Overgaag, D. Vanmaekelbergh and W. L. Vos. *Controlling the dynamics of spontaneous emission from quantum dots by photonic crystals.* Nature **430**, 654 (2004).

[35] D. Englund, D. Fattal, E. Waks, G. Solomon, B. Zhang, T. Nakaoka, Y. Arakawa, Y. Yamamoto and J. Vučković. *Controlling the spontaneous emission rate of single quantum dots in a two-dimensional photonic crystal.* Phys. Rev. Lett. **95**, 013904 (2005).

[36] Q. Wang, S. Stobbe and P. Lodahl. *Mapping the local density of optical states of a photonic crystal with single quantum dots.* Phys. Rev. Lett. **107**, 167404 (2011).

[37] T. Yoshie, A. Scherer, J. Hendrickson, G. Khitrova, H. M. Gibbs, G. Rupper, C. Ell, O. B. Shchekin and D. G. Deppe. *Vacuum Rabi splitting with a single quantum dot in a photonic crystal nanocavity.* Nature **432**, 200 (2004).

[38] H. Thyrrestrup, L. Sapienza and P. Lodahl. *Extraction of the β-factor for single quantum dots coupled to a photonic crystal waveguide.* Appl. Phys. Lett. **96**, 231106 (2010).

[39] T. Baba. *Slow light in photonic crystals.* Nat. Photonics **2**, 465 (2008).

[40] M. Eichenfield, J. Chan, R. M. Camacho, K. J. Vahala and O. Painter. *Optomechanical crystals.* Nature **462**, 78 (2009).

[41] M. Povinelli, S. G. Johnson, E. Lidorikis, J. Joannopoulos and M. Soljačić. *Effect of a photonic band gap on scattering from waveguide disorder.* Appl. Phys. Lett. **84**, 3639 (2004).

[42] S. Hughes, L. Ramunno, J. F. Young and J. E. Sipe. *Extrinsic Optical Scattering Loss in Photonic Crystal Waveguides: Role of Fabrication Disorder and Photon Group Velocity.* Phys. Rev. Lett. **94**, 033903 (2005).

[43] D. Gerace and L. C. Andreani. *Disorder-induced losses in photonic crystal waveguides with line defects.* Opt. Lett. **29**, 1897 (2004).

[44] S. Mazoyer, J. P. Hugonin and P. Lalanne. *Disorder-Induced Multiple Scattering in Photonic-Crystal Waveguides.* Phys. Rev. Lett. **103**, 063903 (2009).

[45] E. Kuramochi, M. Notomi, S. Hughes, A. Shinya, T. Watanabe and L. Ramunno. *Disorder-induced scattering loss of line-defect waveguides in photonic crystal slabs.* Phys. Rev. B **72**, 161318 (2005).

[46] L. Ramunno and S. Hughes. *Disorder-induced resonance shifts in high-index-contrast photonic crystal nanocavities.* Phys. Rev. B **79**, 161303 (2009).

[47] M. Patterson and S. Hughes. *Interplay between disorder-induced scattering and local field effects in photonic crystal waveguides.* Phys. Rev. B **81**, 245321 (2010).

[48] P. W. Anderson. *Absence of diffusion in certain random lattices.* Physical review **109**, 1492 (1958).

[49] V. Savona. *Electromagnetic modes of a disordered photonic crystal.* Phys. Rev. B **83**, 085301 (2011).

[50] S. R. Huisman, G. Ctistis, S. Stobbe, A. P. Mosk, J. L. Herek, A. Lagendijk, P. Lodahl, W. Vos and P. W. H. Pinkse. *Photonic-crystal waveguides with disorder: Measurement of a band-edge tail in the density of states.* Phys. Rev. B **86**, 155154 (2012).

[51] P. Sheng. *Introduction to Wave Scattering, Localization and Mesoscopic Phenomena: Localization and Mesoscopic Phenomena*, volume 88 (Springer, 2006).

[52] J. Topolancik, B. Ilic and F. Vollmer. *Experimental Observation of Strong Photon Localization in Disordered Photonic Crystal Waveguides.* Phys. Rev. Lett. **99**, 253901 (2007).

[53] J. Topolancik, F. Vollmer, R. Ilic and M. Crescimanno. *Out-of-plane scattering from vertically asymmetric photonic crystal slab waveguides with in-plane disorder.* Opt. Express **17**, 12470 (2009).

[54] Y. Akahane, T. Asano, B.-S. Song and S. Noda. *High-Q photonic nanocavity in a two-dimensional photonic crystal.* Nature **425**, 944 (2003).

[55] L. Sapienza, H. Thyrrestrup, S. Stobbe, P. D. Garcia, S. Smolka and P. Lodahl. *Cavity quantum electrodynamics with Anderson localized modes.* Science **327**, 1352 (2010).

[56] K. Vynck, M. Burresi, F. Riboli and D. S. Wiersma. *Photon management in two-dimensional disordered media.* Nat. Mat. **11**, 1017 (2012).

[57] H. E. Türeci, L. Ge, S. Rotter and A. D. Stone. *Strong interactions in multimode random lasers.* Science **320**, 643 (2008).

[58] J. Liu, P. Garcia, S. Ek, N. Gregersen, T. Suhr, M. Schubert, J. Mørk, S. Stobbe and P. Lodahl. *Random nanolasing in the Anderson localized regime.* Nat. Nanotechnol. (2014).

[59] L. O'Faolain, T. P. White, D. O'Brien, X. Yuan, M. D. Settle and T. F. Krauss. *Dependence of extrinsic loss on group velocity in photonic crystal waveguides.* Opt. Express **15**, 13129 (2007).

[60] N. Le Thomas, H. Zhang, J. Jágerská, V. Zabelin, R. Houdré, I. Sagnes and A. Talneau. *Light transport regimes in slow light photonic crystal waveguides.* Phys. Rev. B **80**, 125332 (2009).

[61] J. Topolancik, F. Vollmer, R. Ilic and M. Crescimanno. *Out-of-plane scattering from vertically asymmetric photonic crystal slab waveguides with in-plane disorder.* Opt. Express **17**, 12470 (2009).

[62] S. Smolka, H. Thyrrestrup, L. Sapienza, T. B. Lehmann, K. R. Rix, L. S. Froufe-Pérez, P. D. García and P. Lodahl. *Probing statistical properties of Anderson localization with quantum emitters.* New J. Phys. **13**, 063044 (2011).

[63] A. Baron, S. Mazoyer, W. Smigaj and P. Lalanne. *Attenuation coefficient of single-mode periodic waveguides.* Phys. Rev. Lett. **107**, 153901 (2011).

[64] M. Spasenović, D. M. Beggs, P. Lalanne, T. F. Krauss and L. Kuipers. *Measuring the spatial extent of individual localized photonic states.* Phys. Rev. B **86**, 155153 (2012).

[65] P. D. García, S. Stobbe, I. Söllner and P. Lodahl. *Nonuniversal intensity correlations in a two-dimensional Anderson-localizing random medium.* Phys. Rev. Lett. **109**, 253902 (2012).

[66] H. Thyrrestrup, S. Smolka, L. Sapienza and P. Lodahl. *Statistical Theory of a Quantum Emitter Strongly Coupled to Anderson-Localized Modes.* Phys. Rev. Lett. **108**, 113901 (2012).

[67] P. D. Garcia, A. Javadi, H. Thyrrestrup and P. Lodahl. *Quantifying the intrinsic amount of fabrication disorder in photonic-crystal waveguides from optical far-field intensity measurements.* Appl. Phys. Lett. **102**, 031101 (2013).

[68] A. Kiraz, P. Michler, C. Becher, B. Gayral, A. Imamoğlu, L. Zhang, E. Hu, W. Schoenfeld and P. Petroff. *Cavity-quantum electrodynamics using a single InAs quantum dot in a microdisk structure.* Appl. Phys. Lett. **78**, 3932 (2001).

[69] S. G. Johnson, M. Povinelli, M. Soljačić, A. Karalis, S. Jacobs and J. Joannopoulos. *Roughness losses and volume-current methods in photonic-crystal waveguides.* Appl. Phys. B **81**, 283 (2005).

[70] M. Nishan, A. Javadi, P. Garcia, P. Lodahl and S. Hughes. *Theory and experiments of disorder-induced resonance shifts and mode edge broadening in deliberately disordered photonic crystal waveguides.* Under perpration .

[71] J. Gao, S. Combrie, B. Liang, P. Schmitteckert, G. Lehoucq, S. Xavier, X. Xu, K. Busch, D. L. Huffaker, A. De Rossi *et al. Strongly coupled slow-light polaritons in one-dimensional disordered localized states.* Scientific reports **3** (2013).

[72] A. Javadi, S. Mahmoodian, I. Söllner and P. Lodahl. *In-depth investigation of quantum emitters in photonic crystal waveguides using finite-element modeling.* Under perpration .

[73] E. M. Purcell. *Spontaneous emission probabilities at radio frequencies.* Phys. Rev. **69**, 681 (1946).

[74] K. H. Drexhage, H. Kuhn and F. P. Schafer. *Variation of the fluorescence decay time of a molecule in front of a mirror.* In *Berichte der Bunsengesellschaft für Physikalische Chemie*, volume 72, p. 329 (1968).

[75] P. Goy, J. M. Raimond, M. Gross and S. Haroche. *Observation of Cavity-Enhanced Single-Atom Spontaneous Emission.* Phys. Rev. Lett. **50**, 1903 (1983).

[76] V. P. Bykov. *Spontaneous emission from a medium with a band spectrum.* Sov. J. Quant. Electron. **4**, 861 (1975).

[77] G. Rempe, H. Walther and N. Klein. *Observation of quantum collapse and revival in a one-atom maser.* Phys. Rev. Lett. **58**, 353 (1987).

[78] R. J. Thompson, G. Rempe and H. J. Kimble. *Observation of normal-mode splitting for an atom in an optical cavity.* Phys. Rev. Lett. **68**, 1132 (1992).

[79] K. Busch and S. John. *Photonic band gap formation in certain self-organizing systems.* Phys. Rev. B **58**, 3896 (1998).

[80] N. Vats, S. John and K. Busch. *Theory of fluorescence in photonic crystals.* Phys. Rev. A **65**, 043808 (2002).

[81] A. F. Koenderink, M. Kafesaki, C. M. Soukoulis and V. Sandoghdar. *Spontaneous emission rates of dipoles in photonic crystal membranes.* J. Opt. Soc. Am. B. **23**, 1196 (2006).

[82] I. S. Nikolaev, W. L. Vos and A. F. Koenderink. *Accurate calculation of the local density of optical states in inverse-opal photonic crystals.* J. Opt. Soc. Am. B. **26**, 987 (2009).

[83] W. L. Vos, A. F. Koenderink and I. S. Nikolaev. *Orientation-dependent spontaneous emission rates of a two-level quantum emitter in any nanophotonic environment.* Phys. Rev. A **80**, 053802 (2009).

[84] Y. Chen, N. Gregersen, T. R. Nielsen, J. Mørk and P. Lodahl. *Spontaneous decay of a single quantum dot coupled to a metallic slot waveguide in the presence of leaky plasmonic modes.* Opt. Express **18**, 12489 (2010).

[85] Y. Chen, T. R. Nielsen, N. Gregersen, P. Lodahl and J. Mørk. *Finite-element modeling of spontaneous emission of a quantum emitter at nanoscale proximity to plasmonic waveguides.* Phys. Rev. B **81**, 125431 (2010).

[86] J. M. Gérard, B. Sermage, B. Gayral, B. Legrand, E. Costard and V. Thierry-Mieg. *Enhanced spontaneous emission by quantum boxes in a monolithic optical microcavity.* Phys. Rev. Lett. **81** (1998).

[87] A. Badolato, K. Hennessy, M. Atatüre, J. Dreiser, E. Hu, P. M. Petroff and A. Imamoğlu. *Deterministic Coupling of Single Quantum Dots to Single Nanocavity Modes.* Science **308**, 1158 (2005).

[88] M. Pelton, C. Santori, J. Vučković, B. Zhang, G. S. Solomon, J. Plant and Y. Yamamoto. *Efficient Source of Single Photons: A Single Quantum Dot in a Micropost Microcavity.* Phys. Rev. Lett. **89**, 233602 (2002).

[89] J. Vučković, D. Fattal, C. Santori, G. S. Solomon and Y. Yamamoto. *Enhanced single-photon emission from a quantum dot in a micropost microcavity.* Appl. Phys. Lett. **82**, 3596 (2003).

[90] S. Noda, M. Fujita and T. Asano. *Spontaneous-emission control by photonic crystals and nanocavities.* Nat. Photonics **1**, 449 (2007).

[91] J. P. Reithmaier, G. Sęk, A. Löffler, C. Hofmann, S. Kuhn, S. Reitzenstein, L. V. Keldysh, V. D. Kulakovskii, T. L. Reinecke and A. Forchel. *Strong coupling in a single quantum dot-semiconductor microcavity system.* Nature **432**, 197 (2004).

[92] E. Peter, P. Senellart, D. Martrou, A. Lemaître, J. Hours, J. M. Gérard and J. Bloch. *Exciton-photon strong-coupling regime for a single quantum dot embedded in a microcavity.* Phys. Rev. Lett. **95**, 067401 (2005).

[93] K. Hennessy, A. Badolato, M. Winger, D. Gerace, M. Atatüre, S. Gulde, S. Fält, E. L. Hu and A. Imamoğlu. *Quantum nature of a strongly coupled single quantum dot-cavity system.* Nature **445**, 896 (2007).

[94] G. Khitrova, H. Gibbs, M. Kira, S. Koch and A. Scherer. *Vacuum Rabi splitting in semiconductors.* Nat. Phys. **2**, 81 (2006).

[95] Q. Wang, S. Stobbe, H. Thyrrestup, H. Hofmann, M. Kamp, T. Schlereth, S. Höfling and P. Lodahl. *Highly anisotropic decay rates of single quantum dots in photonic crystal membranes.* Opt. Lett. **35**, 2768 (2010).

[96] S. Hughes. *Enhanced single-photon emission from quantum dots in photonic crystal waveguides and nanocavities.* Opt. Lett. **29**, 2659 (2004).

[97] V. S. C. Manga Rao and S. Hughes. *Single quantum-dot Purcell factor and β-factor in a photonic crystal waveguide.* Phys. Rev. B **75**, 205437 (2007).

[98] G. Lecamp, P. Lalanne and J. P. Hugonin. *Very large spontaneous-emission β Factors in Photonic-Crystal Waveguides.* Phys. Rev. Lett. **99**, 023902 (2007).

[99] S. J. Dewhurst, D. Granados, D. J. P. Ellis, A. J. Bennett, R. B. Patel, I. Farrer, D. Anderson, G. A. C. Jones, D. A. Ritchie and A. J. Shields. *Slow-light-enhanced single quantum dot emission in a unidirectional photonic crystal waveguide.* Appl. Phys. Lett. **96**, 031109 (2010).

[100] T. B. Hoang, J. Beetz, L. Midolo, M. Skacel, M. Lermer, M. Kamp, S. Höfling, L. Balet, N. Chauvin and A. Fiore. *Enhanced spontaneous emission from quantum dots in short photonic crystal waveguides.* Appl. Phys. Lett. **100**, 061122 (2012).

[101] A. Laucht, S. Pütz, T. Günthner, N. Hauke, R. Saive, S. Frédérick, M. Bichler, M.-C. Amann, A. Holleitner, M. Kaniber and J. J. Finley. *A Waveguide-Coupled On-Chip Single-Photon Source.* Phys. Rev. X **2**, 011014 (2012).

[102] T. Reichert, S. Lichtmannecker, G. Reithmaier, M. Zeitlmair, J. Wembacher, A. Rauscher, M. Bichler, K. Müller, M. Kaniber and J. J. Finley. *Highly directed emission from self-assembled quantum dots into guided modes in disordered photonic-crystal waveguides.* Phys. Rev. B **90**, 115310 (2014).

[103] M. O. Scully and M. S. Zubairy. *Quantum Optics* (Cambridge University Press, 2001).

[104] S. M. Barnett, B. Huttner, R. Louden and R. Matloob. *Decay of excited atoms in absorbing dielectrics.* J. Phys. B: At. Mol. Opt. Phys. **29**, 3763 (1996).

[105] L. Novotny and B. Hecht. *Principles of nano-optics* (Cambridge University Press, 2007).

[106] J. N. Reddy. *An introduction to the finite element method.* 2.2 (McGraw-Hill New York, 1993).

[107] R. D. Cook *et al. Concepts and applications of finite element analysis* (John Wiley & Sons, 2007).

[108] I. M. Vinogradov and M. Hazewinkel. *Encyclopaedia of mathematics* (Kluwer Academic Publ, 2001).

[109] J.-P. Berenger. *A perfectly matched layer for the absorption of electromagnetic waves.* J. Comp. Phys. **114**, 185 (1994).

[110] J. Douglas, H. Habibian, A. Gorshkov, H. Kimble and D. Chang. *Atom induced cavities and tunable long-range interactions between atoms trapped near photonic crystals.* arXiv:1312.2435 (2013).

[111] B. Julsgaard, J. Johansen, S. Stobbe, T. Stolberg-Rohr, T. Sünner, M. Kamp, A. Forchel and P. Lodahl. *Decay dynamics of quantum dots influenced by the local density of optical states of two-dimensional photonic crystal membranes.* Appl. Phys. Lett. **93**, 094102 (2008).

[112] K. S. Kunz and R. J. Luebbers. *The finite difference time domain method for electromagnetics* (CRC press, 1993).

[113] A. F. Oskooi, L. Zhang, Y. Avniel and S. G. Johnson. *The failure of perfectly matched layers, and towards their redemption by adiabatic absorbers.* Opt. Express **16**, 11376 (2008).

[114] J. P. Hugonin, P. Lalanne, T. P. White and T. F. Krauss. *Coupling into slow-mode photonic crystal waveguides.* Opt. Lett. **32**, 2638 (2007).

[115] D. Taillaert, W. Bogaerts, P. Bienstman, T. F. Krauss, P. Van Daele, I. Moerman, S. Verstuyft, K. De Mesel and R. Baets. *An out-of-plane grating coupler for efficient butt-coupling between compact planar waveguides and single-mode fibers.* IEEE J. Quant. Electron. **38**, 949 (2002).

[116] A. Faraon, I. Fushman, D. Englund, N. Stoltz, P. Petroff and J. Vučković. *Dipole induced transparency in waveguide coupled photonic crystal cavities.* Opt. Express **16**, 12154 (2008).

[117] Q. V. Tran, S. Combrié, P. Colman and A. D. Rossi. *Photonic crystal membrane waveguides with low insertion losses.* Appl. Phys. Lett. **95**, 061105 (2009).

[118] S.-H. Kim, S.-K. Kim and Y.-H. Lee. *Vertical beaming of wavelength-scale photonic crystal resonators.* Phys. Rev. B **73**, 235117 (2006).

[119] S. Combrié, A. De Rossi *et al. Directive emission from high-Q photonic crystal cavities through band folding.* Phys. Rev. B **79**, 041101 (2009).

[120] S. L. Portalupi, M. Galli, C. Reardon, T. F. Krauss, L. O'Faolain, L. C. Andreani and D. Gerace. *Planar photonic crystal cavities with far-field optimization for high coupling efficiency and quality factor.* Opt. Express **18**, 16064 (2010).

[121] J. Hagemeier, C. Bonato, T.-A. Truong, H. Kim, G. J. Beirne, M. Bakker, M. P. van Exter, Y. Luo, P. Petroff and D. Bouwmeester. *H1 photonic crystal cavities for hybrid quantum information protocols.* Opt. Express **20**, 24714 (2012).

[122] J. Vuckovic, M. Loncar, H. Mabuchi and A. Scherer. *Optimization of the Q factor in photonic crystal microcavities.* IEEE J. Quant. Electron. **38**, 850 (2002).

[123] K. Srinivasan and O. Painter. *Momentum space design of high-Q photonic crystal optical cavities.* Opt. Express **10**, 670 (2002).

[124] M. Notomi, A. Shinya, S. Mitsugi, E. Kuramochi and H. Ryu. *Waveguides, resonators and their coupled elements in photonic crystal slabs.* Opt. Express **12**, 1551 (2004).

[125] J. D. Jackson. *Classical Electrodynamics* (John Wiley & Sons, Inc., 1999).

[126] *Reference guide.* COMSOL Multiphysics, Burlington, MA, USA (2007).

[127] J. You and F. Nori. *Superconducting circuits and quantum information.* arXiv quant-ph/0601121 (2006).

[128] A. Imamoğlu, D. D. Awschalom, G. Burkard, D. P. DiVincenzo, D. Loss, M. Sherwin and A. Small. *Quantum information processing using quantum dot spins and cavity QED.* Phys. Rev. Lett. **83**, 4202 (1999).

[129] A. Muller, E. B. Flagg, P. Bianucci, X. Y. Wang, D. G. Deppe, W. Ma, J. Zhang, G. J. Salamo, M. Xiao and C. K. Shih. *Resonance Fluorescence from a Coherently Driven Semiconductor Quantum Dot in a Cavity.* Phys. Rev. Lett. **99**, 187402 (2007).

[130] R. Melet, V. Voliotis, A. Enderlin, D. Roditchev, X. L. Wang, T. Guillet and R. Grousson. *Resonant excitonic emission of a single quantum dot in the Rabi regime.* Phys. Rev. B **78**, 073301 (2008).

[131] X. Xu, B. Sun, P. R. Berman, D. G. Steel, A. S. Bracker, D. Gammon and L. J. Sham. *Coherent Optical Spectroscopy of a Strongly Driven Quantum Dot.* Science **317**, 929 (2007).

[132] K. Kuroda, T. Kuroda, K. Watanabe, T. Mano, K. Sakoda, G. Kido and N. Koguchi. *Final-state readout of exciton qubits by observing resonantly excited photoluminescence in quantum dots.* Appl. Phys. Lett. **90**, 051909 (2007).

[133] E. B. Flagg, A. Muller, J. W. Robertson, S. Founta, D. G. Deppe, M. Xiao, W. Ma, G. J. Salamo and C. K. Shih. *Resonantly driven coherent oscillations in a solid-state quantum emitter.* Nat. Phys. **5**, 203 (2009).

[134] J.-Y. Marzin, J.-M. Gérard, A. Izrael, D. Barrier and G. Bastard. *Photoluminescence of single InAs quantum dots obtained by self-organized growth on GaAs.* Phys. Rev. Lett. **73**, 716 (1994).

[135] N. H. Bonadeo, J. Erland, D. Gammon, D. Park, D. Katzer and D. Steel. *Coherent optical control of the quantum state of a single quantum dot.* Science **282**, 1473 (1998).

[136] P. Michler, A. Kiraz, C. Becher, W. V. Schoenfeld, P. Petroff, L. Zhang, E. Hu and A. Imamoğlu. *A quantum dot single-photon turnstile device.* Science **290**, 2282 (2000).

[137] C. Santori, M. Pelton, G. Solomon, Y. Dale and Y. Yamamoto. *Triggered single photons from a quantum dot.* Phys. Rev. Lett. **86**, 1502 (2001).

[138] T. Guenther, C. Lienau, T. Elsaesser, M. Glanemann, V. M. Axt, T. Kuhn, S. Eshlaghi and A. D. Wieck. *Coherent nonlinear optical response of single quantum dots studied by ultrafast near-field spectroscopy.* Phys. Rev. Lett. **89**, 057401 (2002).

[139] A. Högele, S. Seidl, M. Kroner, K. Karrai, R. J. Warburton, B. D. Gerardot and P. M. Petroff. *Voltage-controlled optics of a quantum dot.* Phys. Rev. Lett. **93**, 217401 (2004).

[140] B. Alén, F. Bickel, K. Karrai, R. J. Warburton and P. M. Petroff. *Stark-shift modulation absorption spectroscopy of single quantum dots.* Appl. Phys. Lett. **83**, 2235 (2003).

[141] S. Seidl, M. Kroner, P. Dalgarno, A. Högele, J. Smith, M. Ediger, B. Gerardot, J. M. Garcia, P. M. Petroff, K. Karrai *et al. Absorption and photoluminescence spectroscopy on a single self-assembled charge-tunable quantum dot.* Phys. Rev. B **72**, 195339 (2005).

[142] A. Högele, M. Kroner, S. Seidl, K. Karrai, M. Atatüre, J. Dreiser, A. Imamoğlu, R. J. Warburton, A. Badolato, B. D. Gerardot *et al. Spin-selective optical absorption of singly charged excitons in a quantum dot.* Appl. Phys. Lett. **86**, 221905 (2005).

[143] Y. Wu, X. Li, L. Duan, D. Steel and D. Gammon. *Density matrix tomography through sequential coherent optical rotations of an exciton qubit in a single quantum dot.* Phys. Rev. Lett. **96**, 087402 (2006).

[144] A. Ramsay. *A review of the coherent optical control of the exciton and spin states of semiconductor quantum dots.* Semicond. Sci. Technol. **25**, 103001 (2010).

[145] A. N. Vamivakas, Y. Zhao, C.-Y. Lu and M. Atatüre. *Spin-resolved quantum-dot resonance fluorescence.* Nat. Phys. **5**, 198 (2009).

[146] D. Press, T. D. Ladd, B. Zhang and Y. Yamamoto. *Complete quantum control of a single quantum dot spin using ultrafast optical pulses.* Nature **456**, 218 (2008).

[147] A. Vamivakas, M. Atatüre, J. Dreiser, S. Yilmaz, A. Badolato, A. Swan, B. Goldberg, A. Imamoglu and M. Ünlü. *Strong extinction of a far-field laser beam by a single quantum dot.* Nano lett. **7**, 2892 (2007).

[148] B. Gerardot, S. Seidl, P. Dalgarno, R. Warburton, M. Kroner, K. Karrai, A. Badolato and P. Petroff. *Contrast in transmission spectroscopy of a single quantum dot.* Appl. Phys. Lett. **90**, 221106 (2007).

[149] C. Matthiesen, A. N. Vamivakas and M. Atatüre. *Subnatural linewidth single photons from a quantum dot.* Phys. Rev. Lett. **108**, 093602 (2012).

[150] H. S. Nguyen, G. Sallen, C. Voisin, P. Roussignoi, C. Diederichs and G. Cassabois. *Ultra-coherent single photon source.* Appl. Phys. Lett. **99**, 261904 (2011).

[151] Y.-J. Wei, Y.-M. He, M.-C. Chen, Y.-N. Hu, Y. He, D. Wu, M. Kamp, S. Hoefling, C.-Y. Lu and J.-W. Pan. *Deterministic and Robust Generation of Single Photons From a Single Quantum Dot with 99.5% Indistinguishability Using Adiabatic Rapid Passage.* Nano lett. (2014).

[152] A. V. Kuhlmann, J. Houel, A. Ludwig, L. Greuter, D. Reuter, A. D. Wieck, M. Poggio and R. J. Warburton. *Charge noise and spin noise in a semiconductor quantum device.* Nat. Phys. **9**, 570 (2013).

[153] A. V. Kuhlmann, J. H. Prechtel, J. Houel, A. Ludwig, D. Reuter, A. D. Wieck and R. J. Warburton. *Linewidth of single photons from a single quantum dot: key role of nuclear spins.* arXiv:1307.7109 (2013).

[154] J. Hansom, C. H. Schulte, C. Matthiesen, M. J. Stanley and M. Atatüre. *Frequency stabilization of the zero-phonon line of a quantum dot via phonon-assisted active feedback.* Appl. Phys. Lett. **105**, 172107 (2014).

[155] C. Matthiesen, M. J. Stanley, M. Hugues, E. Clarke and M. Atatüre. *Full counting statistics of quantum dot resonance fluorescence.* Scientific reports **4** (2014).

[156] K. Konthasinghe, J. Walker, M. Peiris, C. Shih, Y. Yu, M. Li, J. He, L. Wang, H. Ni, Z. Niu *et al. Coherent versus incoherent light scattering from a quantum dot.* Phys. Rev. B **85**, 235315 (2012).

[157] M. E. Reimer, G. Bulgarini, R. W. Heeres, B. J. Witek, M. A. Versteegh, D. Dalacu, J. Lapointe, P. J. Poole and V. Zwiller. *Overcoming power broadening of the quantum dot emission in a pure wurtzite nanowire.* arXiv:1407.2833 (2014).

[158] J. Dreiser, M. Atatüre, C. Galland, T. Müller, A. Badolato and A. Imamoglu. *Optical investigations of quantum dot spin dynamics as a function of external electric and magnetic fields.* Phys. Rev. B **77**, 075317 (2008).

[159] A. Henriques, A. Schwan, S. Varwig, A. Maia, A. Quivy, D. Yakovlev and M. Bayer. *Spin coherence generation in negatively charged self-assembled (In, Ga) As quantum dots by pumping excited trion states.* Phys. Rev. B **86**, 115333 (2012).

[160] H. S. Nguyen, G. Sallen, C. Voisin, P. Roussignol, C. Diederichs and G. Cassabois. *Optically Gated Resonant Emission of Single Quantum Dots.* Phys. Rev. Lett. **108**, 057401 (2012).

[161] H. S. Nguyen, G. Sallen, M. Abbarchi, R. Ferreira, C. Voisin, P. Roussignol, G. Cassabois and C. Diederichs. *Photoneutralization and slow capture of carriers in quantum dots probed by resonant excitation spectroscopy.* Phys. Rev. B **87**, 115305 (2013).

[162] L. Monniello, C. Tonin, R. Hostein, A. Lemaitre, A. Martinez, V. Voliotis and R. Grousson. *Excitation-induced dephasing in a resonantly driven InAs/GaAs quantum dot.* Phys. Rev. Lett. **111**, 026403 (2013).

[163] O. Gazzano, S. M. de Vasconcellos, C. Arnold, A. Nowak, E. Galophin, I. Sagnes, L. Lanco, A. Lemaître and P. Senellart. *Bright solid-state sources of indistinguishable single photons.* Nat. Commun. **4**, 1425 (2013).

[164] K. H. Madsen, P. Kaer, A. Kreiner-Møller, S. Stobbe, A. Nysteen, J. Mørk and P. Lodahl. *Measuring the effective phonon density of states of a quantum dot in cavity quantum electrodynamics.* Phys. Rev. B **88**, 045316 (2013).

[165] J. Bleuse, J. Claudon, M. Creasey, N. S. Malik, J.-M. Gérard, I. Maksymov, J.-P. Hugonin and P. Lalanne. *Inhibition, Enhancement, and Control of Spontaneous Emission in Photonic Nanowires.* Phys. Rev. Lett. **106**, 103601 (2011).

[166] D. Englund, A. Faraon, I. Fushman, N. Stoltz, P. Petroff and J. Vučković. *Controlling cavity reflectivity with a single quantum dot.* Nature **450**, 857 (2007).

[167] K. Srinivasan and O. Painter. *Linear and nonlinear optical spectroscopy of a strongly coupled microdisk-quantum dot system.* Nature **450**, 862 (2007).

[168] A. Faraon, I. Fushman, D. Englund, N. Stoltz, P. Petroff and J. Vučković. *Coherent generation of non-classical light on a chip via photon-induced tunnelling and blockade.* Nat. Phys. **4**, 859 (2008).

[169] A. Reinhard, T. Volz, M. Winger, A. Badolato, K. J. Hennessy, E. L. Hu and A. Imamoğlu. *Strongly correlated photons on a chip.* Nat. Photonics **6**, 93 (2012).

[170] V. Loo, C. Arnold, O. Gazzano, A. Lemaître, I. Sagnes, O. Krebs, P. Voisin, P. Senellart and L. Lanco. *Optical Nonlinearity for Few-Photon Pulses on a Quantum Dot-Pillar Cavity Device.* Phys. Rev. Lett. **109**, 166806 (2012).

[171] H. Kim, R. Bose, T. C. Shen, G. S. Solomon and E. Waks. *A quantum logic gate between a solid-state quantum bit and a photon.* Nat. Photonics **7**, 373 (2013).

[172] M. Rakher, N. Stoltz, L. Coldren, P. Petroff and D. Bouwmeester. *Externally mode-matched cavity quantum electrodynamics with charge-tunable quantum dots.* Phys. Rev. Lett. **102**, 097403 (2009).

[173] C. Arnold, J. Demory, V. Loo, A. Lemaître, I. Sagnes, M. Glazov, O. Krebs, P. Voisin, P. Senellart and L. Lanco. *Macroscopic Polarization Rotation Induced by a Single Spin.* arXiv:1411.6377 (2014).

[174] S. G. Carter, T. M. Sweeney, M. Kim, C. S. Kim, D. Solenov, S. E. Economou, T. L. Reinecke, L. Yang, A. S. Bracker and D. Gammon. *Quantum control of a spin qubit coupled to a photonic crystal cavity.* Nat. Photonics **7**, 329 (2013).

[175] D. Pinotsi, P. Fallahi, J. Miguel-Sanchez and A. Imamoglu. *Resonant spectroscopy on charge tunable quantum dots in photonic crystal structures.* IEEE J. Quant. Electron. **47**, 1371 (2011).

[176] M. Makhonin, J. Dixon, R. Coles, B. Royall, I. J. Luxmoore, E. Clarke, M. Hugues, M. Skolnick and A. M. Fox. *Waveguide coupled resonance fluorescence from on-chip quantum emitter.* Nano lett. (2014).

[177] G. Reithmaier, M. Kaniber, F. Flassig, S. Lichtmannecker, K. Müller, A. Andrejew, J. Vuckovic, R. Gross and J. Finley. *On-chip generation, routing and detection of quantum light.* arXiv:1408.2275 (2014).

[178] J. Miguel-Sánchez, A. Reinhard, E. Togan, T. Volz, A. Imamoglu, B. Besga, J. Reichel and J. Estève. *Cavity quantum electrodynamics with charge-controlled quantum dots coupled to a fiber Fabry–Perot cavity.* New J. Phys. **15**, 045002 (2013).

[179] A. Faraon, A. Majumdar, H. Kim, P. Petroff and J. Vučković. *Fast electrical control of a quantum dot strongly coupled to a photonic-crystal cavity.* Phys. Rev. Lett. **104**, 047402 (2010).

[180] J. T. Shen and S. Fan. *Coherent photon transport from spontaneous emission in one-dimensional waveguides.* Opt. Lett. **30**, 2001 (2005).

[181] I. N. Söllner. *Quantum Dots in Photonic Crystal Waveguides: From Efficient Single Photon Sources to Deterministic Photon-Photon Interaction.* Ph.D. thesis, The Niels Bohr Institute, Faculty of Science, University of Denmark (2009).

[182] P. R. Rice and H. J. Carmichael. *Single-Atom Cavity-Enhanced Absorption. I: Photon Statistics in the Bad-Cavity Limit.* IEEE J. Quant. Electron. **24**, 1351 (1988).

[183] A. Javadi, I. Söllner, S. L. H. M. Arcari, L. Midolo, S. Mahmoodian, G. Kiršanskė, T. Pregnolato, E. H. Lee, J. D. Song, S. Stobbe and P. Lodahl. *Single photon nonlinear optics with a quantum dot in a waveguide.* Under perpration .

[184] D. E. Chang, V. Vuletić and M. D. Lukin. *Quantum nonlinear optics – photon by photon.* Nat. Photonics **8**, 685 (2014).

[185] M. K. Tey, Z. Chen, S. A. Aljunid, B. Chng, F. Huber, G. Maslennikov and C. Kurtsiefer. *Strong interaction between light and a single trapped atom without the need for a cavity.* Nat. Phys. **4**, 924 (2008).

[186] G. Wrigge, I. Gerhardt, J. Hwang, G. Zumofen and V. Sandoghdar. *Efficient coupling of photons to a single molecule and the observation of its resonance fluorescence.* Nat. Phys. **4**, 60 (2007).

[187] Q. A. Turchette, C. Hood, W. Lange, H. Mabuchi and H. J. Kimble. *Measurement of conditional phase shifts for quantum logic.* Phys. Rev. Lett. **75**, 4710 (1995).

[188] J. Volz, M. Scheucher, C. Junge and A. Rauschenbeutel. *Nonlinear π phase shift for single fibre-guided photons interacting with a single resonator-enhanced atom.* Nat. Photonics **8**, 965 (2014).

[189] H. Gorniaczyk, C. Tresp, J. Schmidt, H. Fedder and S. Hofferberth. *Single Photon Transistor Mediated by Inter-State Rydberg Interaction.* arXiv:1404.2876 (2014).

[190] I. Fushman, D. Englund, A. Faraon, N. Stoltz, P. Petroff and J. Vučković. *Controlled Phase Shifts with a Single Quantum Dot.* Science **320**, 769 (2008).

[191] T. Volz, A. Reinhard, M. Winger, A. Badolato, K. J. Hennessy, E. L. Hu and A. Imamoğlu. *Ultrafast all-optical switching by single photons.* Nat. Photonics **6**, 605 (2012).

[192] J. Kasprzak, S. Reitzenstein, E. Muljarov, C. Kistner, C. Schneider, M. Strauss, S. Höfling, A. Forchel and W. Langbein. *Up on the Jaynes-Cummings ladder of a quantum-dot/microcavity system.* Nat. Mat. **9**, 304 (2010).

[193] R. Bose, D. Sridharan, H. Kim, G. S. Solomon and E. Waks. *Low-photon-number optical switching with a single quantum dot coupled to a photonic crystal cavity.* Phys. Rev. Lett. **108**, 227402 (2012).

[194] D. Englund, A. Majumdar, M. Bajcsy, A. Faraon, P. Petroff and J. Vučković. *Ultrafast photon-photon interaction in a strongly coupled quantum dot-cavity system.* Phys. Rev. Lett. **108**, 093604 (2012).

[195] V. C. Ballenegger and T. Weber. *The Ewald–Oseen extinction theorem and extinction lengths.* Appl. Phys. Lett. **67**, 599 (1999).

[196] A. Auffèves-Garnier, C. Simon, J.-M. Gérard and J.-P. Poizat. *Giant optical nonlinearity induced by a single two-level system interacting with a cavity in the Purcell regime.* Phys. Rev. A **75**, 053823 (2007).

[197] S. Haroche and J.-M. Raimond. *Exploring the Quantum: Atoms, Cavities, and Photons* (Oxford Univ. Press, 2006).

[198] E. Waks and J. Vuckovic. *Dipole induced transparency in drop-filter cavity-waveguide systems.* Phys. Rev. Lett. **96**, 153601 (2006).

[199] K. Konthasinghe, J. Walker, M. Peiris, C. K. Shih, Y. Yu, M. F. Li, J. F. He, L. J. Wang, H. Q. Ni, Z. C. Niu and A. Muller. *Coherent versus incoherent light scattering from a quantum dot.* Phys. Rev. B **85**, 235315 (2012).

[200] D. A. Miller. *Are optical transistors the logical next step?* Nat. Photonics **4**, 3 (2010).

[201] J. L. O'Brien, A. Furusawa and J. Vučković. *Photonic quantum technologies.* Nat. Photonics **3**, 687 (2009).

[202] H. Carmichael. *Photon antibunching and squeezing for a single atom in a resonant cavity.* Phys. Rev. Lett. **55**, 2790 (1985).

[203] D. E. Chang, V. Gritsev, G. Morigi, V. Vuletić, M. D. Lukin and E. A. Demler. *Crystalization of strongly interacting photons in a nonlinear optical fibre.* Nat. Phys. **4**, 884 (2008).

[204] W.-B. Yan and H. Fan. *Control of single-photon transport in a one-dimensional waveguide by a single photon.* Phys. Rev. A **90**, 053807 (2014).

[205] I. Söllner, S. Mahmoodian, S. Lindskov Hansen, L. Midolo, A. Javadi, G. Kiršanskė, T. Pregnolato, H. El-Ella, E. H. Lee, J. D. Song, S. Stobbe and P. Lodahl. *Deterministic photon-emitter coupling in chiral photonic circuits.* arXiv:1406.4295 (2014).